

Rosetta LAP Operations at the Target Comet

Master's Thesis

for the degree of

Master of Science in Space Science and Technology

Kristoffer Hultgren

Luleå University of Technology

Université Paul Sabatier Toulouse III

Swedish Institute of Space Physics, Uppsala

Supervisor: Anders Eriksson

Swedish Institute of Space Physics, Uppsala

June 7, 2009

Abstract

ESA's Rosetta mission is currently en route to comet 67P/Churyumov-Gerasimenko, where it will arrive in 2014. Among the instruments onboard, the Langmuir probe instrument LAP of the Rosetta Plasma Consortium can be expected to be particularly sensitive to early activation of the comet, as it can detect small plasma density changes even at the very low densities typical of the solar wind plasma. By running various operational modes, LAP can also characterize the denser plasmas expected to appear as the coma develops, and monitor the plasma dynamics around the comet all through the mission. In order to exploit these possibilities from the start of operations at the comet, it is essential to define useful operational modes in advance. The objective of this project was to prepare for LAP operations at the comet by simulating LAP measurements in the plasma environment expected at the comet, and for what can be regarded as typical operational scenarios for the spacecraft itself. To do so, results of an ESA-sponsored modeling activity at the International Space Science Institute formed the background, combined with a simulation of the LAP measurements. The results show that for heliocentric distances less than 2 AU, the LAP probe currents are appropriate to follow the dynamics of the plasma, but to extract the electron density and temperature dependence so to give an absolute value of the former we need other instruments, e.g. MIP designed to measure the electron density and temperature, in particular inside the contact surface of the comet, if the electron temperature indeed is as low as predicted by the models. The results also show that Rosetta has a good chance of occasionally being located close to the contact surface which creates a very good possibility to investigate the physics of this hitherto almost unexplored boundary.

Sammanfattning

ESAs rymdfarkost 'Rosetta' är just nu på väg till kometen 67P/Churyumov-Gerasimenko och kommer att anlända år 2014. Bland instrumenten ombord finns ett Langmuirprobinstrument, LAP, som förväntas vara speciellt känsligt för den tidiga aktiveringen av kometen då instrumentet kan detektera små plasmaförändringar även vid mycket låga densiteter, typiska för solvindsplasma. Genom att köra olika operationsmoder kan LAP även karakterisera tätare plasman, vilket förväntas då kometens koma utvecklas, och övervaka plasmadynamiken runt kometen genom hela uppdraget. För att kunna undersöka dessa möjligheter redan från start av operationerna vid kometen är det viktigt att definiera användbara operationsmoder i förväg. Målet för detta projekt var därför att förbereda för LAP-operationer vid kometen genom att simulera LAP-mätningar i plasmaomgivningen som förväntas vid kometen. För att genomföra detta har resultat från ett ESA-sponsrat modelleringsprojekt vid 'International Space Science Institute' i Bern format en bakgrund, kombinerat med modelleringar av LAP-mätningarna. Resultaten visar att för heliocentriska avstånd mindre än 2 AU är strömmarna uppmätta av LAP lämpade för att följa plasmats dynamik, men för att extrahera beroendet av elektrontätheten och elektrontemperaturen för att få fram ett absolutvärde av den förstnämnda behövs andra instrument, t.ex. MIP som är designat för att mäta elektrontätheten och elektrontemperaturen, speciellt innanför kontaktytan hos kometen, åtminstone om den låga temperatur som kometmodellerna förutspår faktiskt visar sig vara den riktiga. Resultaten visar också att Rosetta har en stor möjlighet att befinna sig nära kontaktytan vilket skapar en god möjlighet för att studera fysiken hos denna ännu okända gränssyta i rymden.

Preface

This work was sponsored by the Directorate of Human Spaceflight and Exploration at the European Space Agency (ESA). The aim of the directorate is to implement Europe's participation in the development of space infrastructure, such as the International Space Station (ISS), which makes it possible to perform experiments in a space environment, but also to support the development of research and technologies in space.

This thesis treats the measurements made by Langmuir probes, which are used to determine the electron temperature, electron density, and electric potential of a plasma. The work done is focused on the plasma environment of comets, but can easily be extended to other environments in space, e.g. the orbit of ISS.

On the S1 (starboard) element of the Integrated Truss Structure component of ISS, the Floating Potential Measuring Unit (FPMU) is installed, consisting of four probes: a floating potential probe, a plasma impedance probe (PIP), a wide-sweep Langmuir probe (WLP), and a narrow-sweep Langmuir probe (NLP). Its objective is to provide the ISS program with a capability for monitoring variations in vehicle frame potential due to the ionospheric plasma environment (Coffey et al., 2008). This is an important step in the process of evaluating ISS spacecraft charging issues including vehicle arcing and hazards to crew during extravehicular activities.

It has been known for some time that ISS, with its high voltage (160 V) primary power generation system, will interact strongly with the ambient plasma in which it orbits. For example, the solar arrays have a negative grounding scheme that causes the entire ISS structure to act as an ambient ion collector to compensate for the electrons collected by its more positive solar arrays. In the absence of any mitigation, ISS would float at electrical potentials highly negative relative to its surrounding plasma and these potentials would make ISS arc due to dielectric breakdown. These arcs could, in turn, have life threatening consequences in the form of currents flowing through an astronaut's space suit.

The Langmuir probes included in the FPMU can thus be used to measure the properties of the surrounding plasma in order to help controlling the ISS 'floating potential'.

Contents

| | | |
|----------|---|-----------|
| 1 | Introduction | 1 |
| 1.1 | The Rosetta Mission | 1 |
| 1.2 | The Target Comet 67P/Churyumov-Gerasimenko | 4 |
| 2 | Plasma Physics | 5 |
| 2.1 | Debye Shielding | 5 |
| 2.2 | Kinetic Theory | 6 |
| 2.2.1 | Collisions | 7 |
| 2.3 | Cometary Ionospheres and Magnetospheres | 8 |
| 3 | Plasma Environment Models | 10 |
| 3.1 | The ICES Tool | 10 |
| 3.1.1 | The Hybrid Model | 12 |
| 3.1.2 | The MHD Model | 14 |
| 3.1.3 | Input and Output Files | 17 |
| 4 | Trajectories | 19 |
| 4.1 | Phases | 19 |
| 4.2 | Coordinate Systems | 19 |
| 4.3 | Coordinate Transformations | 20 |
| 4.4 | Orbital Elements | 21 |
| 4.5 | Limits for Keplerian Orbits | 23 |
| 4.6 | Trajectory Plots | 25 |
| 5 | Plasma Environment Model Results | 27 |
| 5.1 | Coordinate System | 27 |
| 5.2 | Hybrid Model Results | 27 |
| 5.2.1 | Heavy Ion Density and Velocity | 27 |
| 5.2.2 | Solar Wind Density and Velocity | 28 |
| 5.2.3 | Magnetic and Electric Fields | 28 |
| 5.3 | MHD Model Results | 35 |
| 5.3.1 | Fluid Density and Velocity | 35 |
| 5.3.2 | Fluid Temperature | 35 |
| 5.3.3 | Magnetic Field | 35 |
| 5.3.4 | The Near Nucleus Environment | 35 |
| 5.4 | Comparison of the Hybrid and MHD Models | 42 |
| 5.5 | DSMC Model Results and a Discussion on Temperatures | 42 |
| 6 | Instrumentation | 44 |
| 6.1 | Langmuir Probes | 44 |
| 6.2 | Measurement Modes | 45 |
| 6.3 | Probe Currents | 46 |
| 6.4 | The I-V Curve | 47 |
| 6.5 | Spacecraft Charging | 49 |
| 6.6 | Instrument Model | 49 |

| | | |
|----------|--|-----------|
| 7 | Results | 51 |
| 7.1 | Approach Phase and the 3.3 AU Case | 51 |
| 7.2 | The 2.7 AU Case | 54 |
| 7.3 | The 2.0 AU Case | 57 |
| 7.4 | The 1.3 AU Case | 62 |
| 8 | Concluding Remarks and Possible Future Work | 66 |
| | Acknowledgments | 68 |
| | References | 69 |
| A | Matlab Routines | 71 |
| A.1 | draworbit.m | 71 |
| A.2 | ecl2orb.m | 71 |
| A.3 | go.m | 71 |
| A.4 | inst.m | 72 |
| A.5 | LP_Constants.m | 72 |
| A.6 | LP_Curre.m | 73 |
| A.7 | LP_Currf.m | 73 |
| A.8 | LP_Curri.m | 73 |
| A.9 | LP_Debye.m | 73 |
| A.10 | LP_IProbe.m | 74 |
| A.11 | LP_SetupInstrument.m | 74 |
| A.12 | LP_SetupPlasma.m | 75 |
| A.13 | LP_Walker.m | 75 |
| A.14 | LP_Vsc.m | 75 |
| A.15 | meanFreePath.m | 76 |
| A.16 | plotCurrents.m | 76 |
| A.17 | plotDSMCOorbit.m | 76 |
| A.18 | plotDSMCPPlane.m | 76 |
| A.19 | plotDSMCPolarOrbit.m | 77 |
| A.20 | plotDSMCTime.m | 77 |
| A.21 | plotHybridOrbit.m | 77 |
| A.22 | plotHybridPlane.m | 77 |
| A.23 | plotHybridPolarOrbit.m | 78 |
| A.24 | plotHybridTime.m | 78 |
| A.25 | plotMHDOorbit.m | 78 |
| A.26 | plotMHDPlane.m | 78 |
| A.27 | plotMHDPolarOrbit.m | 78 |
| A.28 | plotMHDTIME.m | 79 |
| A.29 | plotSweep.m | 79 |
| A.30 | plotSweepMom.m | 79 |
| A.31 | scaleVec.m | 79 |
| A.32 | simulate.m | 80 |
| A.33 | simulateSweep.m | 80 |
| A.34 | simulateTraj.m | 80 |
| A.35 | splitVector.m | 80 |
| A.36 | wholeSpace.m | 80 |

List of Figures

| | | |
|----|--|----|
| 1 | Rosetta's journey to 67P/Churyumov-Gerasimenko (Glassmeier et al., 2007a). | 3 |
| 2 | Cometary activity and boundaries at heliocentric distances smaller than 2 AU. (Adapted from Coates (1997).) | 8 |
| 3 | Structure of the curvilinear simulation grid used in the Hybrid model. The point-like nucleus is at the origin. (Adapted from Hansen et al., 2007.) | 12 |
| 4 | Example of the adaptive grid used in the MHD model for simulation of the 2.0 AU case. The left figure shows the grid in the region of the bow shock and the right figure shows the grid in the region of the diamagnetic cavity and the nucleus. (Adapted from Hansen et al., 2007.) | 14 |
| 5 | The Keplerian elements (adapted from Chobotov (2002)). | 22 |
| 6 | Velocity and period of Rosetta orbiting comet 67P/Churyumov-Gerasimenko. | 24 |
| 7 | Gravitational force exerted on Rosetta by the target comet, compared with the radiation pressure force from the Sun. | 24 |
| 8 | Neutral dynamic force exerted on Rosetta by the target comet at 3 AU. | 25 |
| 9 | Heliocentric 2D view of the Rosetta and the comet trajectories in the ecliptic. | 26 |
| 10 | Comet centered 2D view of Rosetta's approach. | 26 |
| 11 | Hybrid model results for the cometary ion densities of 67P/CG at heliocentric distances of 3.3 AU (A), 2.7 AU (B), 2.0 AU (C), and 1.3 AU (D). (Mind the different box sizes.) | 29 |
| 12 | Hybrid model results for the cometary ion velocities of 67P/CG at heliocentric distances of 3.3 AU (A), 2.7 AU (B), 2.0 AU (C), and 1.3 AU (D). (Mind the different box sizes.) | 30 |
| 13 | Hybrid model results for the solar wind densities of 67P/CG at heliocentric distances of 3.3 AU (A), 2.7 AU (B), 2.0 AU (C), and 1.3 AU (D). (Mind the different box sizes.) | 31 |
| 14 | Hybrid model results for the solar wind velocities of 67P/CG at heliocentric distances of 3.3 AU (A), 2.7 AU (B), 2.0 AU (C), and 1.3 AU (D). (Mind the different box sizes.) | 32 |
| 15 | Hybrid model results for the magnetic field of 67P/CG at heliocentric distances of 3.3 AU (A), 2.7 AU (B), 2.0 AU (C), and 1.3 AU (D). (Mind the different box sizes.) | 33 |
| 16 | Hybrid model results for the electric field of 67P/CG at heliocentric distances of 3.3 AU (A), 2.7 AU (B), 2.0 AU (C), and 1.3 AU (D). (Mind the different box sizes.) | 34 |
| 17 | MHD model results for the fluid densities of 67P/CG at heliocentric distances of 3.3 AU (A), 2.7 AU (B), 2.0 AU (C), and 1.3 AU (D). (Mind the different box sizes.) | 37 |
| 18 | MHD model results for the fluid velocities of 67P/CG at heliocentric distances of 3.3 AU (A), 2.7 AU (B), 2.0 AU (C), and 1.3 AU (D). (Mind the different box sizes.) | 38 |
| 19 | MHD model results of the fluid temperatures of 67P/CG at heliocentric distances of 3.3 AU (A), 2.7 AU (B), 2.0 AU (C), and 1.3 AU (D). (Mind the different box sizes.) | 39 |
| 20 | MHD model results of the magnetic fields of 67P/CG at heliocentric distances of 3.3 AU (A), 2.7 AU (B), 2.0 AU (C), and 1.3 AU (D). (Mind the different box sizes.) | 40 |
| 21 | MHD model results at heliocentric distances of 2.0 AU (A), and 1.3 AU (B). (Mind the different box sizes.) | 41 |
| 22 | DSMC (Direct Simulation Monte Carlo) model results of the neutral temperature of 67P/CG at heliocentric distances of 3.3 AU (A), 2.7 AU (B), 2.0 AU (C), and 1.3 AU (D). The results look a little odd and this is discussed further in the text. (Mind the different box sizes.) | 43 |
| 23 | One of the two LAP probes, to scale (by courtesy of IRF Uppsala). | 45 |
| 24 | A typical I-V curve from a Langmuir probe (adapted from http://www.cluster.irfu.se). | 48 |

| | | |
|----|---|----|
| 25 | Example probe bias sweep from a sunlit probe near the Earth's plasmapause. | 49 |
| 26 | Flowchart of the LAP model. | 50 |
| 27 | Bias sweep current vs. distance during Rosetta's approach to comet 67P/CG. Also included is the solar wind and heavy ion density and the components of the magnetic field during the approach. | 52 |
| 28 | Bias sweep during the approach phase, 3.3 AU, at a distance 50 km from the comet. . . . | 52 |
| 29 | Bias sweep current vs. time of flight during one orbit at a cometocentric distance of 5 km and a heliocentric distance of 3.3 AU. | 53 |
| 30 | Bias sweep at the point $\theta = 0$, a cometocentric distance of 5 km, and a heliocentric distance of 3.3 AU. | 53 |
| 31 | Bias sweep current vs. time of flight during one orbit at a cometocentric distance of 10 km and a heliocentric distance of 2.7 AU. | 55 |
| 32 | Bias sweep at the point $\theta = 0$, a cometocentric distance of 10 km, and a heliocentric distance of 2.7 AU. | 55 |
| 33 | High resolution bias sweep at the point $\theta = 0$, a cometocentric distance of 10 km, and a heliocentric distance of 2.7 AU. Here the step size is 10 mV and the range chosen for simulation is -2.2 to +0.2 V. | 56 |
| 34 | Bias sweep current vs. distance on an imaginary path along the x -axis (towards the Sun) at a heliocentric distance of 2.7 AU. | 56 |
| 35 | Bias sweep current vs. time of flight during one orbit at a cometocentric distance of 10 km and a heliocentric distance of 2.0 AU. | 57 |
| 36 | Plasma parameters vs. time of flight during one orbit at a cometocentric distance of 10 km and a heliocentric distance of 2.0 AU. | 58 |
| 37 | Bias sweep current vs. distance on an imaginary path along the x -axis (towards the Sun) at a heliocentric distance of 2.0 AU. | 59 |
| 38 | Fluid temperature, density, and current vs. cometocentric distance at 2.0 AU. | 59 |
| 39 | Fluid density and current vs. cometocentric distance at 2.0 AU. | 60 |
| 40 | Bias sweep at the point $\theta = 0$, a cometocentric distance of 10 km, and a heliocentric distance of 2.0 AU. | 60 |
| 41 | High resolution bias sweep at the point $\theta = 0$, a cometocentric distance of 10 km, and a heliocentric distance of 2.0 AU. | 61 |
| 42 | Bias sweep current vs. time of flight during one orbit at a cometocentric distance of 5 km and a heliocentric distance of 1.3 AU. | 62 |
| 43 | Fluid temperature, density and current vs. cometocentric distance at 1.3 AU. | 63 |
| 44 | Current vs. cometocentric distance at 1.3 AU. | 63 |
| 45 | The density and magnetic field at 1.3 AU compared with the measured current using constant bias potential. | 64 |
| 46 | Bias sweep current vs. distance on an imaginary path along the x -axis (towards the Sun) at a heliocentric distance of 1.3 AU. | 64 |
| 47 | Bias sweep at the point $\theta = 0$, a cometocentric distance of 5 km, and a heliocentric distance of 1.3 AU. | 65 |
| 48 | High resolution bias sweep at the point $\theta = 0$, a cometocentric distance of 5 km, and a heliocentric distance of 1.3 AU. | 65 |

List of Tables

| | | |
|----|---|----|
| 1 | Milestones of the Rosetta mission (Glassmeier et al., 2007a). | 2 |
| 2 | Orbital elements of the Rosetta target comet 67P/Churyumov-Gerasimenko (from Glassmeier et al., 2007a). | 4 |
| 3 | Gas production rate for H ₂ O (from Tennishev et al. (2008)) | 4 |
| 4 | Available models from the ICES tool (Hansen and Rubin, 2008). | 10 |
| 5 | Available cases (from Hansen and Rubin (2008)). | 11 |
| 6 | Nominal solar wind values at 1 AU used in Hansen and Rubin (2008). | 11 |
| 7 | Upstream solar wind parameters for the different cases (from Hansen and Rubin, 2008). | 11 |
| 8 | Simulation box sizes for the Hybrid cases. | 12 |
| 9 | Simulation box sizes for the MHD cases. | 14 |
| 10 | Input and output quantities and their corresponding units (from Hansen and Rubin, 2008). | 17 |
| 11 | Available quantities in the Hybrid model (from Hansen and Rubin, 2008). | 18 |
| 12 | Available quantities in the MHD model (from Hansen and Rubin, 2008). | 18 |
| 13 | The different phases of Rosetta's cometary approach (from Glassmeier et al., 2007a). | 19 |
| 14 | Useful coordinate systems for describing the position of Rosetta. | 20 |
| 15 | Mean free path at a cometocentric distance of 5 km in the terminator plane. | 43 |
| 16 | Summary of parameters and their ranges accessible to LAP (from Eriksson et al., 2007). | 44 |

1 Introduction

The exploration of our solar system has stimulated one of the most important scientific revolutions of the last decades. Planetary exploration has been carried out by the astronauts who traveled to the Moon, by robotic spacecraft that extend our reach to other planets, and by thousands of scientists working in observatories and laboratories on Earth. This international effort has transformed dozens of planets and satellites from mysterious dots of light into real worlds, each with its own unique environment and history.

You might ask yourself: why do we explore? The urge to explore seems to be fundamental to the character of man. Exploration might be motivated by a desire to understand our environment and the way it works. For some, the satisfaction of exploration can be obtained from watching the news or maybe from reading a book or surfing the internet. For many others, there is an urge to, in addition to a purely intellectual knowledge, having a more personal involvement; we want to travel to new places, either in real world or, as some, in a virtual reality. We have a desire to cross that border, to climb that mountain, and to set foot on that new world.

It is now time for another historical mission to take place - a new world is about to be conquered. Scientists and engineers from all over Europe and the United States have been combining their talents to build an orbiter and a lander for this unique expedition to unravel the secrets of a mysterious 'mini' ice world - a comet. For the first time in history, a spacecraft is about to fly alongside with a comet as it heads towards the inner parts of the solar system. For the first time in history, a spacecraft is about to examine from close proximity how a frozen comet is transformed by the warmth of the Sun and for the first time in the history of mankind - a human made gadget is about to set ground on a mysterious object originating from the outskirts of the solar system.

The spacecraft mentioned above was named 'Rosetta', after the 'Rosetta Stone', as it is hoped to help unlock the secrets of how our Solar System looked before the planets had formed. The rest of this introductory section will present the Rosetta mission and its target comet. Section 2 discusses a few areas from the theory of plasma physics needed before continuing with Section 3 and the plasma environment models used. In Section 4, the trajectories of Rosetta are analyzed together with some limiting forces to help keeping the spacecraft in orbit. Section 5 presents the results from investigating the plasma models, Section 6 deals with instrumentation and modeling the Langmuir probes, and Section 7 presents and discusses the results obtained from performing this work. Finally, Section 8 makes some concluding remarks and discusses possible further work that could be done, maybe by a future thesis worker.

1.1 The Rosetta Mission

Rosetta is a spacecraft with a cuboid shape, $2.8 \times 2.1 \times 2.0$ m, and with two solar panels, 32 m^2 each, spanning 32 m. The launch mass is 2900 kg including the 100 kg lander, 165 kg of scientific instruments, and a lot of fuel. Rosetta is set out to rendez-vous with comet 67P/Churyumov-Gerasimenko (67P/CG) in 2014. It is a cooperative project between ESA, various European national space agencies, and NASA, and consists of two mission elements: the Rosetta orbiter and the Rosetta lander, Philae. The prime scientific objective of the Rosetta mission is to investigate the origin of our solar system by studying the origin of comets. This is interesting because comets are considered to contain the least processed material in our solar system since their condensation from the proto-solar nebula. The physical and compositional properties of comets may therefore be a key to their formation and evolution, hence to the formation of the solar system.

The measurement goals of the Rosetta mission include (Glassmeier et al., 2007a):

- a global characterization of the nucleus;

Table 1: Milestones of the Rosetta mission (Glassmeier et al., 2007a).

| Mission event | Nominal date |
|--|-------------------|
| Launch | March 2, 2004 |
| First Earth Gravity Assist | March 4, 2005 |
| Mars Gravity Assist | February 25, 2007 |
| Second Earth Gravity Assist | November 13, 2007 |
| 2867 Steins Flyby | September 5, 2008 |
| Third Earth Gravity Assist | November 13, 2009 |
| 21 Lutetia Flyby | July 10, 2010 |
| Rendez-Vous Maneuver 1 | January 23, 2011 |
| Start of Hibernation | July, 2011 |
| Hibernation Wake-Up | January, 2014 |
| Rendez-Vous Maneuver 2 (4.5 - 4.0 AU) | May 22, 2014 |
| Start of Near-Nucleus Operations (3.25 AU) | August 22, 2014 |
| Philae Delivery | November 10, 2014 |
| Start of Comet Escort | November 16, 2014 |
| Perihelion Passage | August, 2015 |
| End of Nominal Mission | December 31, 2015 |

- the determination of its dynamical properties;
- the surface morphology and composition;
- the determination of chemical, mineralogical and isotopic compositions of volatiles in the cometary nucleus;
- the determination of the physical properties of volatiles in the cometary nucleus;
- studies of the development of cometary activity and the processes in the surface layer of the nucleus and inner coma, i.e. dust/gas interaction;
- studies of the evolution of the interaction region of the solar wind and the outgassing comet during perihelion approach.

The original target of the Rosetta mission was comet 46P/Wirtanen. However, a failure of an Ariane rocket forced ESA to postpone the launch and to re-target Rosetta on comet 67P/CG. Rosetta was finally launched with an Ariane-5 rocket from the Guyana Space Center in Kourou, French Guyana, on March 2, 2004 (Glassmeier et al., 2007a).

Table 1 provides an overview of the different milestones of the Rosetta mission. During an approximately ten-year trek, Rosetta will travel the distance Sun-Earth several times, and will pass through the asteroid belt into deep space beyond 5 AU before it reaches its destination. As is illustrated in Figure 1, Rosetta will employ four planetary gravity assist maneuvers to acquire sufficient energy to reach the comet (Earth-Mars-Earth-Earth). At the time of writing, the first three of these have already been successful, as has the fly-by of the main belt asteroid 2867 Steins (Keller, 2008). After the third Earth fly-by, Rosetta will return to the main asteroid belt and encounter the asteroid 21 Lutetia at a distance of 3000 km (Glassmeier et al., 2007a).

The spacecraft will enter a hibernation phase in July, 2011, which will last until wake-up in January 2014, and then begin a series of rendez-vous maneuvers for the target comet in May 2014.

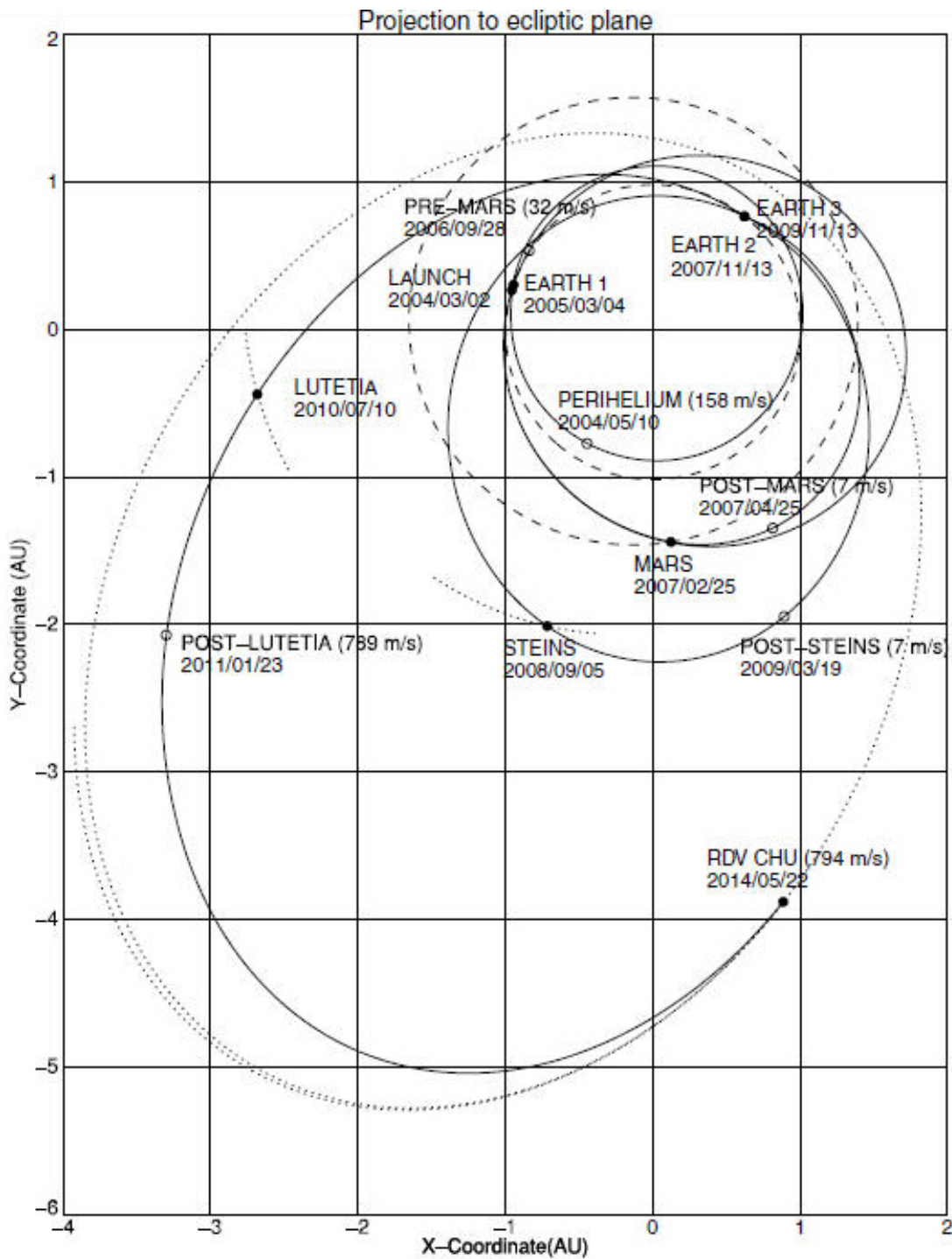


Figure 1: Rosetta's journey to 67P/Churyumov-Gerasimenko (Glassmeier et al., 2007a).

1.2 The Target Comet 67P/Churyumov-Gerasimenko

The comet 67P/CG is a Jupiter Family comet (JFC) discovered in 1969. JFCs are comets that are believed to be ejected from the Kuiper Belt region by Neptune and later captured by Jupiter into a short-periodic, near-ecliptic orbit around the Sun. This means that their formation region was the icy outskirts of the planetary system and that their interior preserves the least altered material from the formation period of the solar system (Glassmeier et al., 2007a).

67P/CG is a small sized body with an effective radius of about 2 km, low albedo, and asymmetric shape. Lamy et al. (2007) gives an estimate of a bulk density of $370 \text{ kg}\cdot\text{m}^{-3}$ which leads to a mass of about $8 \cdot 10^{12} \text{ kg}$. The current orbital elements of 67P/CG are listed in Table 2, together with the last perihelion date. These elements will remain unchanged well beyond the Rosetta mission duration.

A porous layer of ice and solid grains that covers the surface of a cometary nucleus is subjected to a periodic solar illumination that causes the sublimation of volatiles and serves as the source of gas in a coma. The main photoionization product is H_2O^+ and the production rate Q (adopted from Hansen et al., 2007) for four different heliocentric distances, to be used later, is presented in Table 3.

Table 2: Orbital elements of the Rosetta target comet 67P/Churyumov-Gerasimenko (from Glassmeier et al., 2007a).

| | |
|---------------------------|-------------------|
| Perihelion distance (AU) | 1.28931109 |
| Eccentricity | 0.631935597 |
| Ascending node (deg) | 50.923016 |
| Perihelion argument (deg) | 11.367883 |
| Inclination (deg) | 7.1272258 |
| Last perihelion date | 2002-Aug-18.23754 |

Table 3: Gas production rate for H_2O (from Tennishev et al. (2008))

| r_h (AU) | Q (s^{-1}) |
|------------|-------------------------|
| 1.3 | $5 \cdot 10^{27}$ |
| 2.0 | $8 \cdot 10^{26}$ |
| 2.7 | $8 \cdot 10^{25}$ |
| 3.3 | $1 \cdot 10^{24}$ |

2 Plasma Physics

In our daily experience, matter can be divided into solids, liquids, and gases, but moving upwards from the surface of the Earth our environment changes and no longer fits into this picture. The ionosphere begins at a height of just 80 km - hence the atmosphere already contains an ionized particle component at this level. With increasing height the relative importance of the neutral component decreases and ionized matter becomes dominant. Even farther out in the magnetosphere and in interplanetary space almost all gas is ionized by the heavy electromagnetic radiation from the Sun and space is therefore dominated by a plasma - *the fourth state of matter*.

It is however not enough for a gas to be ionized in order to be a plasma. The general definition of a plasma is that it must be *a quasi-neutral gas of charged and neutral particles which exhibits collective behavior* (Chen, 1984). Quasi-neutrality is discussed further below and the term ‘collective behavior’ simply means that charged particles must be close enough together that each particle influences many nearby charged particles, rather than just interacting with the closest particle (Dendy, 1995).

To be able to correctly describe the plasma environment of comets, we first need to define some basic properties of plasmas.

2.1 Debye Shielding

One of the most fundamental properties of a plasma is its *Debye length*. The Debye length is the scale over which mobile charge carriers screen out electric fields in plasmas and other conductors. In other words, the Debye length is the longest distance over which significant charge separation can occur.

If an object placed in a plasma has a different potential than that of the surrounding plasma, it will either attract electrons and repel ions or attract ions and repel electrons, depending on its potential. This will create a *sheath* around the object with an excess of particles with opposite charge to that of the object. This sheath will reduce the potential of the object as ‘seen’ by particles outside of the sheath, much like electrons reduce the charge of the nucleus as seen by other charges far away from the atom. This phenomenon is known as *Debye shielding* and the characteristic thickness of the sheath, or the radius of the *Debye sphere*, is thus the *Debye length*.

The vacuum electrostatic potential at a distance r from a particle with charge q is

$$V(r) = \frac{q}{4\pi\epsilon_0 r}. \quad (1)$$

In the presence of a plasma this relation is slightly modified in such a way that the electric field becomes confined to a short range (Parks, 2004), and the potential can be written as

$$V(r) = \frac{q}{4\pi\epsilon_0 r} e^{-r/\lambda_D}, \quad (2)$$

where λ_D is the Debye length, defined by

$$\lambda_D^2 = \frac{k_B T_e \epsilon_0}{n_0 q_e^2}. \quad (3)$$

Here k_B is Boltzmann’s constant, T_e is the electron temperature in units of kelvin, ϵ_0 is the permittivity of free space, n_0 is the equilibrium density of the plasma, and q_e is the charge of the electrons.

If $r \ll \lambda_D$, equation 2 tells us that the potential reduces to the simple Coulomb potential. Conversely, if $r > \lambda_D$, $V(r)$ decreases exponentially and the potential around a point charge is effectively screened

out. This leaves the bulk of the plasma free of large electric potentials and, in regions outside λ_D , the plasma is unaffected and is said to be *quasi-neutral* (Parks, 2004), i.e.

$$n_i \approx n_e. \quad (4)$$

2.2 Kinetic Theory

The dynamics of a plasma is mainly described by two different theories; magnetohydrodynamic (MHD) theory and kinetic theory. The former will be discussed together with the MHD model used in this work, in Section 3.1.2, while the latter follows below.

Kinetic theory starts from the microscopic approach, i.e. the physics of individual particles. The macroscopic phenomena can then be described by averaging over a sufficiently large number of particles. The mechanical properties of each particle are described completely by its position and momentum, and the average speed of these particles is also the plasma flow speed \bar{u} . The speeds of individual particles, however, can be substantially different; in particular, speeds of individual particles can exceed the flow speed by several orders of magnitude (Kallenrode, 2004). If the system is in thermal equilibrium, which is not necessarily the case for hot plasmas, the velocity distribution is given by the Maxwellian distribution:

$$f(\vec{r}, \vec{v}, t) = n \sqrt{\left(\frac{m}{2\pi k_B T}\right)^3} \exp\left\{-\frac{m(\vec{v} - \bar{u})^2}{2k_B T}\right\}, \quad (5)$$

where T is the plasma temperature and m is the mass of the particle species under study. The most probable speed is obtained from the maximum of the distribution, i.e.

$$v_{th} = \sqrt{\frac{2k_B T}{m}}. \quad (6)$$

If the plasma is not in thermal equilibrium, energy exchanges will occur between the charged particles and normally no analytical distribution function exists (Kim and Jung, 2007). Occasionally, the particle distribution can be described by a Maxwellian up to a certain energy; at higher energies the particle distribution is fitted much better by a power law than by an exponential decay. Here the kappa distribution, also called the Lorentzian distribution,

$$f(\vec{r}, \vec{v}, t) = \frac{n}{\kappa} \sqrt{\left(\frac{m}{2\pi k_B T}\right)^3} \left[1 + \frac{m(\vec{v} - \bar{u})^2}{2\kappa E_T}\right]^{-\kappa-1}, \quad (7)$$

can be used as an approximation (Kallenrode, 2004). The parameters κ and E_T are characteristics of the distribution, with E_T being closely associated with temperature and κ describing the deviation of the distribution from a Maxwellian. As $\kappa \rightarrow \infty$, we recover the Maxwellian distribution with temperature $k_B T = E_T$.

If the plasma is subject to a pure electromagnetic field, the particles will, in addition to the thermal motion, follow the equation of motion as described by the *Lorentz force*:

$$m \frac{d\vec{v}}{dt} = q \left(\vec{E} + \vec{v} \times \vec{B} \right). \quad (8)$$

Solving this, it is found that the electric field introduces a drift motion

$$\vec{v}_{\vec{E} \times \vec{B}} = \frac{\vec{E} \times \vec{B}}{B^2}, \quad (9)$$

usually denoted as the $\vec{E} \times \vec{B}$ -drift.

If the field is a pure magnetic field, equation 8 reduces to

$$m \frac{d\vec{v}}{dt} = q\vec{v} \times \vec{B}, \quad (10)$$

and by solving this, the solution can be seen (Kallenrode, 2004) to describe a harmonic oscillator with a *cyclotron frequency*

$$\omega_c = \frac{|q|B}{m}. \quad (11)$$

The solution of the equation of motion is a circular orbit around the magnetic field lines with a trajectory described by

$$x(t) = r_L \sin \omega_c t, \quad (12)$$

$$y(t) = r_L \cos \omega_c t, \quad (13)$$

where the radius of the particle orbit, the *Larmor radius*, or the *gyro-radius*, is given by

$$r_L = \frac{v_{\perp}}{\omega_c} = \frac{mv_{\perp}}{|q|B}. \quad (14)$$

When the density grows, and the particles involved starts to notice that the environment is crowded, a lot of collisions occur - this is to be discussed next.

2.2.1 Collisions

Collisions are important in the energy transfer between, and hence the temperature of, different components in a plasma. For example, close to a comet the plasma also contains neutral particles ejected from the nucleus. In time, collisions with charged particles in the solar wind will equalize the two distributions, leading to an acceleration of the neutrals.

The number of collisions depends on the number density of particles and on their ‘size’ as described by the scattering cross section. Consider a fast particle with radius r_1 moving in a gas of slow particles with radii r_2 . A collision happens if the distance between the two particles has decreased below $r_1 + r_2$. Alternatively, we can assume the fast particle to be a mass point. Then we have to attribute a radius of $r_1 + r_2$ to the gas molecules. Thus for the fast particle, a gas molecule is equivalent to a disc with the scattering cross section $\sigma = \pi (r_1 + r_2)^2$ (Kallenrode, 2004).

The average distance traveled by a particle between collisions is called the mean free path and is defined as

$$\lambda_m = \frac{1}{n_s \sigma}, \quad (15)$$

where n_s is the number density of the target particles per unit volume.

The above discussion applies for interactions with neutrals. Collisions between charged particles are different, as they interact at a distance. The formalism for this use is more advanced but not needed in this work.

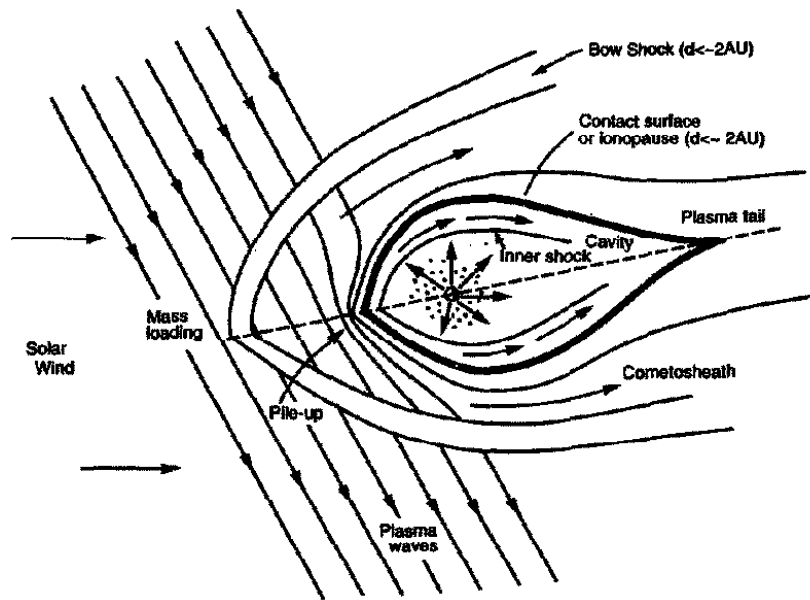


Figure 2: Cometary activity and boundaries at heliocentric distances smaller than 2 AU. (Adapted from Coates (1997).)

2.3 Cometary Ionospheres and Magnetospheres

Let us now turn to the dynamics of plasmas surrounding a comet.

As a comet's orbit takes it near to the Sun, neutral gas and dust are driven away from the nucleus. The gas ionizes due to photoionization and charge exchange and a dense ionosphere forms near to the comet, bounded by a contact surface (Figure 2). Once the particles have been ionized, they attain a net positive electrical charge which in turn gives rise to an induced magnetosphere around the comet. The comet and its induced magnetic field form an obstacle to outward flowing solar wind particles and as the relative orbital speed of the comet and the solar wind is supersonic, a bow shock is formed upstream of the comet in the flow direction of the solar wind. In this bow shock, large concentrations of cometary ions (called pick-up ions) congregate and act to load the solar magnetic field with plasma, such that the field lines *drape* around the comet forming the ion tail (Coates, 1997).

As the solar magnetic field is loaded, conservation of momentum and energy require that the solar wind slows down. Continuous deceleration of the solar wind flow by mass loading is possible only up to a certain point at which the mean molecular weight of the plasma particles reaches a critical value. At this point a weak shock forms and impulsively decelerates the flow to subsonic velocities. A cometosheath forms between the cometary shock and the magnetic field free region in the innermost coma. The plasma population in the cometosheath is a changing mixture of ambient solar wind constituents and particles picked up upstream and downstream of the shock. Near the nucleus, ion-neutral chemistry and recombination starts to become more and more important. In the inner coma, an ionopause separates the solar wind controlled magnetized plasma from the magnetic field free cometary ionosphere, the *diamagnetic cavity*. Deep inside the diamagnetic cavity, the cometary plasma and the neutral gas are very strongly coupled by ion-neutral collisions, and they move radially outward with the same expansion velocity (Hansen et al., 2007).

For weaker production rate comets, where the sizes of comatosheath and/or the bow shock standoff distance would be comparable to or even smaller than the ion gyro-radius, the above basic picture does not hold (Bagdonat and Motschmann, 2002a). This will be especially important at the time of the Rosetta - 67P/CG rendez-vous when the production rate is very low. At this time, the classical ideas of bow shocks and diamagnetic cavities are meaningless. The complex nature of the interaction between the solar wind and the comet can also be further complicated by the large difference in the gyro-radii of protons and heavy ions (1:18 in mass).

3 Plasma Environment Models

As is discussed above, the cometary plasma environment is driven by the ionization of the neutral coma. Therefore, any plasma model must either include a prescribed or a self-consistent model of the neutral distribution and its interaction with the plasma. The neutral distribution is often taken to be a simple spherically symmetric source which expands at a constant velocity:

$$n_n = \frac{Q}{4\pi u_n r^2} \exp\left(-\frac{r}{\lambda}\right), \quad (16)$$

where Q is the gas production rate, $u_n = 1$ km/s is the radial neutral velocity, r is the distance from the nucleus, and λ is the ionization scale length. Both the gas production rate, Q , and the ionization scale length, λ , depend on heliocentric distance (Hansen et al., 2007).

As is also discussed above: near the beginning of the Rosetta mission, the gyro-radius of ions is large compared to the extent of 67P/CG's plasma structures and the classical ideas of bow shocks and diamagnetic cavities does not hold. While the comet is in this state, a model which includes finite gyro-radius effects is required to accurately describe the plasma. For this reason, a semi-kinetic hybrid (HYB) particle model of the plasma exists together with a magnetohydrodynamic (MHD) model, the latter holding for a plasma where the gas production rate is larger, the finite gyro-radius effects are smaller, and a fluid description of the plasma becomes valid.

In both of the models, the neutral distribution described above is used to compute the effects of mass loading and collisions. Mass loading in the two models is handled via an effective ionization rate chosen to include contributions from both photoionization and charge exchange. In each model, the effects of ion-neutral collisions as well as the momentum exchange effects of charge exchange are handled through a friction term where the effective friction coefficient is chosen to include all relevant collisional processes (Hansen et al., 2007).

Table 4: Available models from the ICES tool (Hansen and Rubin, 2008).

| Abbrev. | Description | Physics |
|---------|----------------------------------|---------------------------------------|
| ICES | Inner Coma Environment Simulator | User interface & tool |
| DSMC | Direct Simulation Monte Carlo | Dust and neutral gas |
| ELEC | Electron | Field aligned electrons |
| HYB | Hybrid | Plasma: kinetic ions, fluid electrons |
| MHD | Magnetohydrodynamics | Plasma: single fluid |

3.1 The ICES Tool

The Inner Coma Environment Simulation tool (ICES) has been developed as part of the efforts of the International Space Science Institute (ISSI) comet modeling team. The intent of the tool is to provide access to results from a comprehensive set of models of the cometary coma ranging from the surface out to the interaction with the solar wind and covering dust, gas, and plasma phases (Hansen and Rubin, 2008). The models available are listed in Table 4 and further explained below.

The ICES model can either be downloaded from http://csem.engin.umich.edu/ISSI_Comet/ICES/ and compiled in a Linux environment, or simply be used through the GUI at http://csem.engin.umich.edu/ISSI_Comet/ICES/GUI/. In this work, both ways were used due to some compatibility problems when compiling the MHD codes.

Table 5: Available cases (from Hansen and Rubin (2008)).

| Heliocentric Distance | Description |
|-----------------------|-----------------------|
| 1.3 AU | Closest approach |
| 2.0 AU | Intermediate distance |
| 2.7 AU | Lander operation |
| 3.3 AU | Rendez-vous |

Table 6: Nominal solar wind values at 1 AU used in Hansen and Rubin (2008).

| Quantity | Value |
|-------------------------|--------------------------|
| Solar wind speed | 400 km/s |
| Number density | 10 cm^{-3} |
| Electron temperature | $1 \cdot 10^5 \text{ K}$ |
| Ion temperature | $5 \cdot 10^4 \text{ K}$ |
| Magnetic field strength | 7 nT |

The ISSI comet modeling team chose to model the comet at four representative heliocentric radial distances that represent either significant times of the mission or serve to span the range of plasma environments that can be expected during the mission (Table 5).

The solar wind conditions used in these models are based on nominal values at 1 AU (Table 6) and then extrapolated to obtain the conditions for each of the cases. Table 7 gives values in the upstream solar wind for density (n), velocity (v), magnetic field strength (B), Parker spiral angle (α), Alfvén speed (v_a), and electric field (E). Note that these values are only representative of the conditions that comet 67P/CG may encounter during the Rosetta mission. However, as average values they will give a good idea of the type and scale of the expected interaction between the comet and the solar wind.

In this work, mainly the Hybrid and the MHD models have been used and a brief review of these will now follow. For a more comprehensive description the reader is referred to the respective articles cited in the text.

Table 7: Upstream solar wind parameters for the different cases (from Hansen and Rubin, 2008).

| R (AU) | $n \text{ (cm}^{-3}\text{)}$ | $v \text{ (km/s)}$ | $v_a \text{ (km/s)}$ | B (nT) | $\alpha(^{\circ})$ | E (mV/m) |
|--------|------------------------------|--------------------|----------------------|--------|--------------------|----------|
| 3.3 | 0.9 | 400 | 36.8 | 1.6 | 73 | 1.54 |
| 2.7 | 1.4 | 400 | 36.9 | 2.0 | 70 | 1.00 |
| 2.0 | 2.5 | 400 | 38.7 | 2.8 | 63 | 0.75 |
| 1.3 | 6.0 | 400 | 43.7 | 4.9 | 52 | 0.61 |

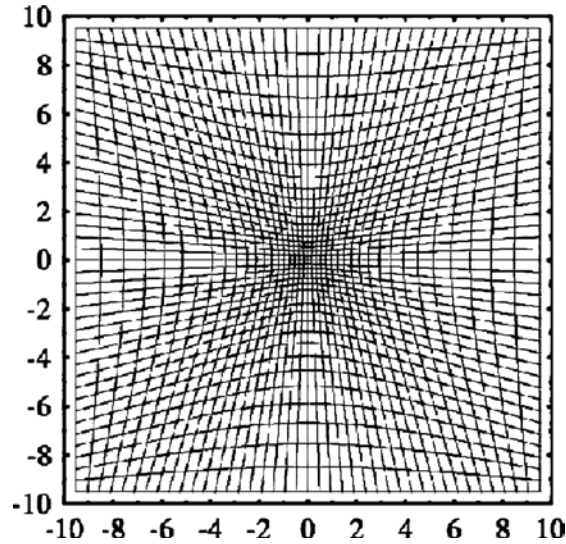


Figure 3: Structure of the curvilinear simulation grid used in the Hybrid model. The point-like nucleus is at the origin. (Adapted from Hansen et al., 2007.)

Table 8: Simulation box sizes for the Hybrid cases.

| Case | Boundary (+x) |
|--------|---------------------|
| 3.3 AU | $0.36 \cdot 10^6$ m |
| 2.7 AU | $1 \cdot 10^6$ m |
| 2.0 AU | $6 \cdot 10^6$ m |
| 1.3 AU | $10 \cdot 10^6$ m |

3.1.1 The Hybrid Model

The Hybrid model describes the plasma environment as a massless charge-neutralizing fluid of electrons using typical conservation equations, together with ions treated as particles with equations of motion solved individually. The electrons in the model interact with the ions mainly by virtue of their pressure. Two ion species are considered: the solar wind protons and the ions of cometary origin. The cometary ions are much heavier than the solar wind protons so in order to correctly model the ions, the dynamic equations include collisions with neutral gas in addition to the Lorentz force.

The Hybrid model operates on a three dimensional static but curvilinear grid (Figure 3). The domain is chosen in such a way that important potential plasma signatures near the nucleus are covered, especially the bow shock, cometopause, and diamagnetic cavity. Simulations are performed on a $90 \times 90 \times 90$ grid where, in each case, the smallest cell at the nucleus is about one third the size of the largest at the box boundaries. Table 8 lists the box sizes for the different cases, found by trial and error while using the model.

The solar wind flow is supersonic, and therefore information from the interaction between the solar wind and the comet does not travel upstream. This means that simple boundary conditions can be chosen; upstream uses a constant inflow boundary where newly inserted particles have a thermal distribution and all field quantities are kept constant; downstream uses an outflow boundary where all particles which

cross the boundary are deleted. At an inflow boundary, new particles have to be inserted at each time step and at an outflow boundary, the crossing particles are simply deleted and all field quantities are linearly extrapolated (Hansen et al., 2007; Bagdonat and Motschmann, 2002a).

Basic Equations As mentioned above, the electrons are assumed to be a massless charge-neutralizing fluid ($m_e = 0$) and the ions are treated as particles. The code solves the equation of motion for the ions and a momentum conservation equation,

$$\nabla p_e = -n_e e \left(\vec{E} + \vec{v}_e \times \vec{B} \right), \quad (17)$$

for the electron fluid (Bagdonat and Motschmann, 2002ab). This gives an equation for the electric field in the form

$$\vec{E} = -\frac{\vec{J}_{ion} \times \vec{B}}{\rho_c} + \frac{(\nabla \times \vec{B}) \times \vec{B}}{\mu_0 \rho_c} + \frac{\nabla p_e}{\rho_c} + \eta \frac{\nabla \times \vec{B}}{\rho_c}, \quad (18)$$

where ρ_c is the ion charge density, \vec{J}_{ion} is the ion current density, p_e is the electron pressure, and η a constant representing resistivity effects.

From Faraday's law,

$$\frac{\partial \vec{B}}{\partial t} = -\nabla \times \vec{E}, \quad (19)$$

a partial differential equation for the time development of the magnetic field is obtained and, by assuming an adiabatic behavior of the kinetic pressure, an equation of state

$$p_e = p_{e0} \left(\frac{\rho_e}{\rho_{e0}} \right)^\kappa \quad (20)$$

is valid. Here ρ_{e0} and p_{e0} are the initial background quantities, the latter one given by means of the electronic plasma beta

$$\beta = \frac{p}{p_B}; \quad (21)$$

the ratio of the plasma pressure to the magnetic pressure (Bagdonat and Motschmann, 2002ab). As thermodynamic coupling of the motion only is effective perpendicular to the magnetic field in a collisionless plasma, the thermodynamics of the system is quasi two-dimensional implying $\kappa = 2$ instead of the usual value of $5/3$ (Bagdonat and Motschmann, 2002b).

The cometary ions are very cold compared to the solar wind ions. However, the cometary electrons have a thermal energy of about 1 eV, corresponding to $\beta_e = 0.2$ (Bagdonat and Motschmann, 2002b), since they are produced by an ionization process. This temperature is still different from the solar wind electron temperature and, unfortunately, the Hybrid description does not allow for different electron species with different temperatures because β_e is a global parameter (Bagdonat and Motschmann, 2002b). This parameter may play an important role for the physics near the nucleus and was therefore chosen according to the temperature of the cometary electrons. However, the value of $\beta_e = 0.2$ is not very different from the typical solar wind value of $\beta_e = 0.4$ for larger distances from the Sun.

Further discussions on temperature can be found in Section 5.5.

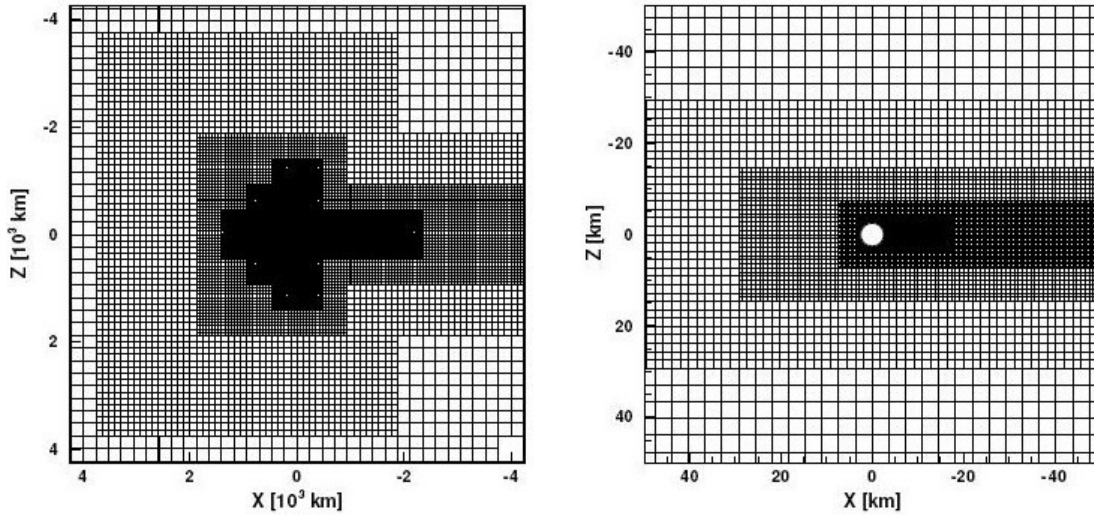


Figure 4: Example of the adaptive grid used in the MHD model for simulation of the 2.0 AU case. The left figure shows the grid in the region of the bow shock and the right figure shows the grid in the region of the diamagnetic cavity and the nucleus. (Adapted from Hansen et al., 2007.)

Table 9: Simulation box sizes for the MHD cases.

| Case | Boundary (+x) | Min Δx | Max Δx |
|--------|------------------|----------------|--------------------|
| 3.3 AU | $2 \cdot 10^6$ m | 60 m | 250 km |
| 2.7 AU | $2 \cdot 10^6$ m | 60 m | 250 km |
| 2.0 AU | $1 \cdot 10^7$ m | 60 m | $7.5 \cdot 10^5$ m |
| 1.3 AU | $4 \cdot 10^9$ m | 500 m | $2.5 \cdot 10^8$ m |

3.1.2 The MHD Model

When the plasma can be described accurately as a single fluid, the MHD model can be used. This code solves the governing equations of ideal magnetohydrodynamics and here the plasma is treated as a single species plasma; effects related to finite gyro-radius, resistivity, and other kinetic effects are neglected.

One of the most important features of the MHD model is that it utilizes the approach of adaptive blocks. Adaptive blocks partition space into regions, each of which is a regular Cartesian grid of cells, called a block. If the region needs to be refined, the block is replaced by 8 sub-blocks, each of which contains the same number of cells as the parent block. The basic data structure used is thus a hierarchical cell-based octree structure (Gombosi et al., 1999); each cell has a pointer to its parent cell (if one exists) and to its eight children cells (if they exist). The ‘leaves of the tree’, i.e. the cells with no children, are the cells on which the calculation takes place. Figure 4 shows examples of this and Table 9 lists the smallest and largest cell sizes as well as the size of the simulation domain for the MHD simulations.

The mesh is generated in such a way that important geometry and flow features are resolved. The geometry is resolved by recursively dividing cells near the comet until a specified cell-size is obtained. Flow features are resolved by acquiring a solution on the original mesh, dividing cells in which the flow gradients are considerable, and unrefining cells in which the flow gradients are negligible. This is done

by first looking at $|\nabla \cdot \vec{u}|$, $|\nabla \times \vec{u}|$, and $|\nabla \vec{B}|$ in each cell, then refine cells in which any of these three is large or unrefine cells in which all of these three are small (Gombosi et al., 1996 1999).

Basic Equations The global scale 3D MHD model of the cometary plasma environment is a single-fluid model. This means that some of the underlying physics must be simplified. The main simplifying assumptions are the following (Gombosi et al., 1999):

- The pitch-angles of freshly ionized particles are assumed to be instantaneously scattered to an isotropic shell distribution (isotropic in the plasma frame).
- The flow velocities of implanted ions and the mass-loaded solar wind are assumed to be identical.
- Collisions, including charge exchange, between plasma particles and cometary neutrals do not change the plasma mass density. Even though this is not strictly true, it leads to a reasonable approximation with great mathematical simplification.

The basic equations for ideal MHD, a perfectly conducting fluid moving at non-relativistic speeds in three dimensions, are expressions from

- conservation of mass (1 eq.),
- conservation of momentum (3 eq.),
- Faraday's law (3 eq.), and
- conservation of energy (1 eq.).

These eight equations incorporates eight dependent variables:

- mass density (ρ),
- momentum ($\rho u_x, \rho u_y, \rho u_z$),
- magnetic field (B_x, B_y, B_z), and
- total plasma energy (E),

where \vec{u} is the solar wind velocity and where

$$E = \rho e + \rho \frac{\vec{u} \cdot \vec{u}}{2} + \frac{\vec{B} \cdot \vec{B}}{2\mu_0}. \quad (22)$$

Here the second and third terms on the right hand side represents the kinetic energy of the fluid and the total energy density of the magnetic field. The first term on the right is the thermal energy, where

$$e = \frac{p}{(\gamma - 1)\rho}, \quad (23)$$

the ideal-gas equation of state, is used to relate pressure and energy (Powell et al., 1999 Parks, 2004). In the above equations the total mass density and pressure, $\rho = \rho_{sw} + \rho_c$ and $p = p_{sw} + p_c$, are used. γ is the adiabatic index, or the heat capacity ratio, given by $\gamma = C_p/C_v$.

The production rate of cometary ions due to photoionization of neutrals is given by

$$\dot{n}_n = \frac{Q}{4\pi\lambda r^2} \exp\left(-\frac{r}{\lambda}\right). \quad (24)$$

The derivation and details of the set of equations used in the model will not be presented here. Instead, we will just present the result and refer the interested reader to Gombosi et al. (1996 1999) and Powell et al. (1999). The problem ends up as a Riemann problem¹, and hence needs a Riemann solver (for details on Riemann solvers see Eleuterio (1999)). Following Gombosi et al. (1999), the set of equations obtained by adding the conservation equations for the solar wind and implanted ions can be written as

$$\frac{\partial \mathbf{W}}{\partial t} + (\nabla \cdot \mathbf{F})^T = \mathbf{S} + \mathbf{P} - \mathbf{L}, \quad (25)$$

where T symbolizes a transposed matrix. \mathbf{W} is a state vector given by

$$\mathbf{W} = \begin{pmatrix} \rho \\ \rho \vec{u} \\ \vec{B} \\ \frac{1}{2}\rho \vec{u} \cdot \vec{u} + \frac{3}{2}p + \frac{1}{2\mu_0} \vec{B} \cdot \vec{B} \end{pmatrix}, \quad (26)$$

and \mathbf{F} is a flux tensor given by

$$\mathbf{F} = \begin{pmatrix} \rho \vec{u} \\ \rho \vec{u} \vec{u} + \left(p + \frac{1}{2\mu_0} \vec{B} \cdot \vec{B}\right) \mathbf{I} - \frac{1}{\mu_0} \vec{B} \vec{B} \\ \vec{u} \vec{B} - \vec{B} \vec{u} \\ \vec{u} \left(\frac{1}{2}\rho \vec{u} \cdot \vec{u} + \frac{5}{2}p + \frac{1}{\mu_0} \vec{B} \cdot \vec{B}\right) - (\vec{B} \cdot \vec{u}) \vec{B} \end{pmatrix}^T, \quad (27)$$

where μ_0 is the permeability of vacuum and \mathbf{I} is an identity matrix. \mathbf{S} is a source vector,

$$\mathbf{S} = -\nabla \cdot \vec{B} \begin{pmatrix} 0 \\ \frac{1}{\mu_0} \vec{B} \\ \vec{u} \\ \frac{1}{\mu_0} \vec{B} \cdot \vec{u} \end{pmatrix}, \quad (28)$$

containing the terms that cannot be expressed in divergence form, \mathbf{P} is given by

$$\mathbf{P} = \dot{\rho} \begin{pmatrix} 1 \\ \vec{u}_n + \eta_c \rho (\vec{u}_n - \vec{u}) \\ 0 \\ \frac{1}{2} [u_n^2 + \eta_c \rho (u_n^2 - u^2) - 3\eta_c p] \end{pmatrix}, \quad (29)$$

where \vec{u}_n is the cometary neutral gas bulk velocity, η_c is a ion-neutral friction coefficient, and the mass addition rate is given by

$$\dot{\rho} = \frac{m_c Q}{4\pi\lambda r^2} \exp\left(-\frac{r}{\lambda}\right), \quad (30)$$

¹A Riemann problem consists of a conservation law together with a piecewise constant data having a single discontinuity. One of the important issues is to numerically maintain the $\nabla \cdot \vec{B} = 0$ condition to avoid any unphysical effects (Eleuterio, 1999).

Table 10: Input and output quantities and their corresponding units (from Hansen and Rubin, 2008).

| Quantity | Unit |
|----------------|-------------------|
| Position | m |
| Density | m^{-3} |
| Velocity | $km \cdot s^{-1}$ |
| Magnetic field | T (Tesla) |
| Pressure | Pa (Pascal) |
| Temperature | K (Kelvin) |
| Energy | eV |

with m_c being the mass of the implanted ions. \mathbf{L} is a loss term given by

$$\mathbf{L} = \alpha_e n_e \begin{pmatrix} \rho \\ \rho \vec{u} \\ 0 \\ \frac{1}{2} \rho u^2 + \frac{3}{2} p \end{pmatrix}, \quad (31)$$

where $\alpha_e n_e$ is a recombination coefficient discussed in detail in Gombosi et al. (1996).

Note that in the above equations, terms proportional to $\nabla \cdot \vec{B}$ are retained. These terms arise from rewriting the magnetic field terms in the basic equations in a divergence form. Although, for physical fields there are no magnetic monopoles and the source term is therefore zero. Dropping the source term from the analysis changes the character of the equations in such a way to make them unsymmetrizable. The above system has substantially better numerical properties than one based on the form in which the source term \mathbf{S} is dropped. The resulting numerical scheme treats $\nabla \cdot \vec{B}$ as a passive scalar and any $\nabla \cdot \vec{B}$ that is created numerically is passively convected. In this treatment $\nabla \cdot \vec{B} = 0$ is satisfied to within truncation error once it is imposed as an initial condition to the problem. A comprehensive study of this problem can be found in Brackbill and Barnes (1980).

3.1.3 Input and Output Files

Almost all input and output quantities in the ICES tool should be in SI units, with a few exceptions. The quantities and their corresponding units are listed in Table 10.

An input trajectory file should contain a list of points at which the user wishes to extract data from the models. In general this file may be thought of as a list of points along a spacecraft trajectory. The trajectory file should have three columns in it corresponding to the three dimensional location of the desired points x, y, z (more described in Section 5.1). Columns should be separated by spaces only.

After the model has been run, a unique output file is created for the output from each model selected. Output files are named with the name of the model followed by the name of the input data file case used. For the Hybrid model, the available quantities to be output are given in Table 11, and for the MHD model the output quantities are listed in Table 12.

The MHD simulations are single species, so there is no way of knowing the ion composition. Far upstream of the comet the plasma would have an average mass of 1 amu (H), and closer to the comet the average mass would be 18 amu (H_2O). In regions where ions are mixed it is not possible to determine the average mass and for this reason the mass density is given in amu/m³.

Table 11: Available quantities in the Hybrid model (from Hansen and Rubin, 2008).

| Variable | Physical Quantity |
|-------------------------|---|
| x, y, z | Position |
| <i>Status</i> | Indicates the validity of this data point: 0 - value is fine; 1 - Position of point outside the simulation box |
| B_x, B_y, B_z | Magnetic field components |
| E_x, E_y, E_z | Electric field components |
| <i>rhosw</i> | Solar wind ion number density |
| $uswx, uswy, uswz$ | Velocity components of the solar wind ions |
| <i>rho_{hi}</i> | Oxygen ion number density |
| $uhix, uhiy, uhiz$ | Velocity components of Oxygen ions |

Table 12: Available quantities in the MHD model (from Hansen and Rubin, 2008).

| Variable | Physical Quantity |
|-----------------|---|
| x, y, z | Position |
| Status | Indicates the validity of this data point: 0 - value is fine; 1 - Position of point outside the simulation box |
| n | Ion (and electron) mass density |
| V_x, V_y, V_z | Velocity components |
| B_x, B_y, B_z | Magnetic field components |
| p | Thermal pressure in Pascals ($p = nkT$) |

4 Trajectories

During the last part of the journey shown in Figure 1 at about 4.5 AU, Rosetta will begin a series of rendez-vous maneuvers to lower the spacecraft velocity relative to that of the comet at about 25 m/s and put it into the near comet drift phase, starting May 22, 2014, until the distance is about 10 000 km from the comet. One important part of planning the target comet approach is to plot the trajectory in a way that is useful for performing and evaluating measurements. Matlab routines for reading the trajectory data files and make trajectory plots have been developed by former master thesis workers for the Earth (Billvik, 2005) and Mars (Edberg, 2006) fly-bys, and modified to fit this thesis work.

The raw trajectory data files for all the celestial bodies and satellites are provided by the NASA Jet Propulsion Laboratory's (JPL) HORIZONS System. The data for the Rosetta mission ranges only until May 22, the start of the drift phase at about 4 AU, after which the trajectory of the target comet has to be used. For the phases interesting to this project new trajectories in the form of circular orbits and excursions was invented.

4.1 Phases

After May 22, 2014, Rosetta will approach 67P/CG at a relative velocity of about 25 m/s until the distance is about 10 000 km from the comet. The final point of this near-comet drift phase, the comet acquisition point (CAP), is reached at a Sun distance of less than 4 AU. When this is reached, the far approach trajectory phase will start and last for about 30 days. At the end of this phase the relative velocity will have been reduced to about 1.5 m/s at a distance of about 300 comet nucleus radii (the radius of comet 67P/CG is about 2 km with low asymmetric body shape). Here precise determinations of the spacecraft and the comet relative positions, relative velocity, and rotation and gravity of the comet nucleus will be made to fine-tune the approach. At a distance of about 60 comet radii and a speed of a few cm/s, orbit insertion and close approach operations will be performed, and at about 25 comet radii a capture maneuver will close the orbit. At August 22, 2014, the global mapping will commence, this by using polar orbits at 5 to 25 comet radii. After the global studies of the nucleus are completed, close observation will be made at a distance down to 1 nucleus radii. For convenience, these different phases are summarized in Table 13.

Table 13: The different phases of Rosetta's cometary approach (from Glassmeier et al., 2007a).

| Phase | Distance | Velocity | Time |
|-------------------------|-------------------|-----------------|--------------------|
| Near-comet drift | Down to 10 000 km | Down to 25 m/s | After May 22, 2014 |
| Far approach trajectory | Down to 600 km | Down to 1.5 m/s | 30 days |
| Orbit insertion | 120 km | cm's/s | |
| Orbit closure | 50 km | | |
| Mapping | 10-50 km | | August 22, 2014 |
| Close observations | Down to 2 km | | |

4.2 Coordinate Systems

The data files provided by the HORIZONS system are given in a Geocentric Ecliptic Aries (GEA) system, i.e. the xy -plane is the ecliptic plane; the positive x -axis points towards the vernal equinox of the Earth, the positive z -axis points towards the ecliptic north, and the y -axis completes the right-handed

Table 14: Useful coordinate systems for describing the position of Rosetta.

| Coordinate system | Direction of x -axis | Direction of z -axis | Center |
|--|------------------------|-------------------------------|--------|
| GEA <small>(Geocentric Ecliptic Aries)</small> | Earth vernal equinox | Ecliptic north | Earth |
| HEA <small>(Heliocentric Ecliptic Aries)</small> | Earth vernal equinox | Ecliptic north | Sun |
| CEA <small>(Comet Ecliptic Aries)</small> | Earth vernal equinox | Ecliptic north | Comet |
| CEC <small>(Comet Ecliptic asCending node)</small> | Comet ascending node | Ecliptic north | Comet |
| COC <small>(Comet Orbital asCending node)</small> | Comet ascending node | Normal to comet orbital plane | Comet |
| CSO <small>(Comet Solar Orbital)</small> | Comet-Sun line | Normal to comet orbital plane | Comet |

system which is centered on the Earth. These coordinates have to be transformed into other coordinate systems in order to get useful plots of the events at the target comet. The coordinate systems used are listed in Table 14, and the transformation between these are described in detail below.

4.3 Coordinate Transformations

GEA to CEA

To move the center of the frame from the Earth to the comet, a subtraction of the position of the target comet in GEA-coordinates from the position of Rosetta in GEA-coordinates is performed:

$$[r_R]_{CEA} = [r_R]_{GEA} - [r_C]_{GEA}, \quad (32)$$

where r_R is the position of Rosetta and r_C is the position of the target comet. The notation $[]$ simply applies that this is a matrix.

GEA to HEA

To move the center of the frame from the Earth to the Sun, a subtraction of the position of the Sun in GEA-coordinates from the position of Rosetta in GEA-coordinates is performed:

$$[r_R]_{HEA} = [r_R]_{GEA} - [r_S]_{GEA}, \quad (33)$$

where r_S is the position of the Sun. This transformation can also be performed for the target comet by using the cometary coordinates instead of Rosetta's.

CEA to CEC

To fix the x -axis on the comet ascending node, a rotation around the z -axis is performed:

$$[r_R]_{CEC} = [R(\Omega)] [r_R]_{CEA} = \begin{bmatrix} \cos \Omega & \sin \Omega & 0 \\ -\sin \Omega & \cos \Omega & 0 \\ 0 & 0 & 1 \end{bmatrix} [r_R]_{CEA}, \quad (34)$$

where Ω is the longitude of the comet ascending node with respect to the ecliptic and the Earth vernal equinox.

CEC to COC

To make the z -axis normal to the comet orbital plane, a rotation around the x -axis is performed:

$$[r_R]_{COC} = [P(i)] [r_R]_{CEC} = \begin{bmatrix} 1 & 0 & 0 \\ 0 & \cos i & \sin i \\ 0 & -\sin i & \cos i \end{bmatrix} [r_R]_{CEC}, \quad (35)$$

where i is the inclination of the comet orbital plane with respect to the ecliptic.

COC to CSO

To fix the x -axis along the comet-Sun line, another rotation around the z -axis is performed:

$$[r_R]_{CSO} = [R(l)] [r_R]_{COC} = \begin{bmatrix} \cos l & \sin l & 0 \\ -\sin l & \cos l & 0 \\ 0 & 0 & 1 \end{bmatrix} [r_R]_{COC}, \quad (36)$$

where l is the longitude of the Sun, i.e. the angle between the comet ascending node and the Sun:

$$l = \arctan \left\{ \frac{y_{COC}(\text{Sun})}{x_{COC}(\text{Sun})} \right\}. \quad (37)$$

Hence, the complete transformation is given by

$$[r_R]_{CSO} = [R(l)] [P(i)] [R(\Omega)] ([r_R]_{GEA} - [r_C]_{GEA}). \quad (38)$$

4.4 Orbital Elements

To invent different orbits around the comet we would like to define this by giving three of the Keplerian parameters of the orbit suggested. The available elements are listed below and some of them are illustrated in Figure 5.

- Eccentricity, ϵ
- Semi-major axis, a
- Inclination, i
- Longitude of ascending node, Ω
- Argument of periapsis, ω

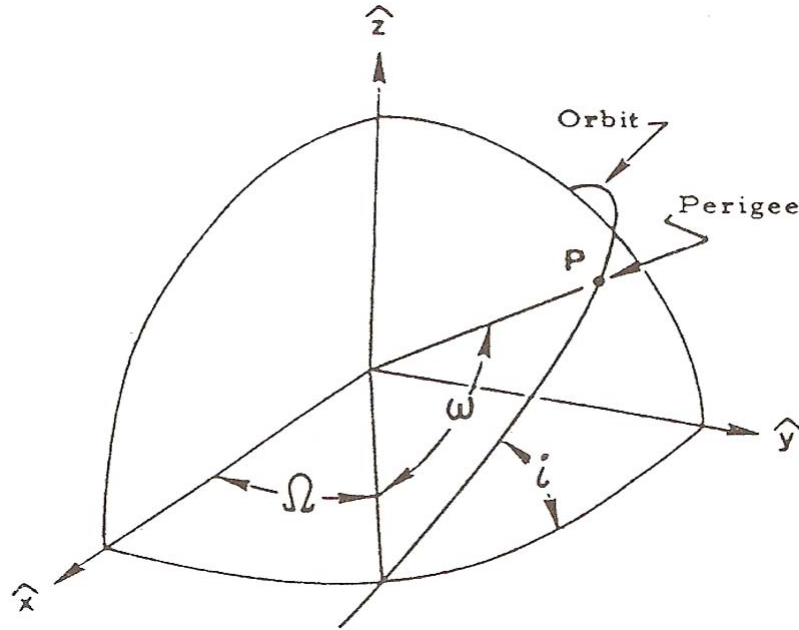


Figure 5: The Keplerian elements (adapted from Chobotov (2002)).

- True anomaly, ν

We will work with circular orbits and therefore the semi-major axis, a , will be specified by the altitude of the orbit and the eccentricity is zero.

To transform the coordinate system of the ecliptic plane into the orbital system defined above we use the Euler angle transformations. The angles i , Ω , ω are then the Euler angles characterizing the orientation of the coordinate system $\hat{x}, \hat{y}, \hat{z}$ with \hat{x}, \hat{y} in the orbital plane and \hat{x} in the direction of the pericenter. For circular orbits we can choose $\omega = 0$, so that the pericenter always coincides with the ascending node. In this case the transformation from the Euler angles to the $\hat{x}, \hat{y}, \hat{z}$ -system is

$$\begin{aligned}
 x_1 &= \cos \Omega \\
 x_2 &= \sin \Omega \\
 x_3 &= 0 \\
 y_1 &= -\sin \Omega \cos i \\
 y_2 &= \cos \Omega \cos i \\
 y_3 &= \sin i \\
 z_1 &= \sin i \sin \Omega \\
 z_2 &= -\sin i \cos \Omega \\
 z_3 &= \cos i
 \end{aligned} \tag{39}$$

Now, for a chosen altitude a , the points on the orbit is given by

$$\hat{r} = a \cos \nu \hat{x} + a \sin \nu \hat{y} \quad (40)$$

where the only variable is ν . In other words, we can perform a transformation of the polar coordinates in the orbital plane, given by $\hat{r} = (a \cos \nu \ a \sin \nu \ 0)$, to the system in the ecliptic plane, r , by

$$\begin{aligned} r &= \hat{r} \cdot (\hat{x} \ \hat{y} \ \hat{z}) \\ &= \begin{pmatrix} \cos \Omega & \sin \Omega & 0 \\ -\sin \Omega \cos i & \cos \Omega \cos i & \sin i \\ \sin i \sin \Omega & -\sin i \cos \Omega & \cos i \end{pmatrix} (a \cos \nu \ a \sin \nu \ 0)^T \\ &= a \begin{pmatrix} \cos \nu \cos \Omega + \sin \nu \sin \Omega \\ -\cos \nu \sin \Omega \cos i + \sin \nu \cos \Omega \cos i \\ \cos \nu \sin i \sin \Omega - \sin \nu \sin i \cos \Omega \end{pmatrix}. \end{aligned} \quad (41)$$

The above procedure was collected in a Matlab function (Appendix A, draworbit.m) which draws the specified orbit and exports the x,y,z -coordinates as a space separated text file, later to be used in the ICES model discussed above.

4.5 Limits for Keplerian Orbits

Using the comet's mass estimated in Lamy et al. (2007), the equation for velocity in a circular orbit with radius r ,

$$v = \sqrt{\frac{\mu}{r}} = \sqrt{\frac{GM}{r}}, \quad (42)$$

and Kepler's third law,

$$P = 2\pi \sqrt{\frac{r^3}{G(M+m)}}, \quad (43)$$

where G is the gravitational constant, M is the mass of the comet, and m is the mass of Rosetta (which can be completely neglected compared to M), gives the orbital velocity and period as functions of r , shown in Figure 6. Here it can be seen that for an altitude of, for example, 25 km the velocity is approximately 15 cm/s with a period of about 12 days.

From the approximate size of Rosetta, $A = 32 \cdot 2 + 3 \cdot 2 = 70 \text{ m}^2$, and the solar constant, $I_{\odot} = 1370 \text{ W} \cdot \text{m}^{-2}$, the radiation pressure force from the Sun can be calculated by

$$F_{\odot} = \frac{I \cdot A}{d^2} \quad (44)$$

to be $320 \mu\text{N}$ at $d = 1 \text{ AU}$ and $35 \mu\text{N}$ at $d = 3 \text{ AU}$. For the 1 AU case, this is less compared to the gravitational force exerted on Rosetta out to a distance of about 70 km, as can be seen in Figure 7, and for the 3 AU case, the radiation pressure can be totally neglected when planning orbits.

Figure 8 shows the neutral dynamic force, $F_q = \frac{1}{2} A n m v^2$, from the DSMC model at 3 AU. Here Rosetta's maximum area has been used, i.e. if Rosetta would have its solar panels pointed towards the comet. For the 1 AU case, the force increases by a factor of 10 so not even in this case is the neutral pressure near the gravitational force keeping Rosetta in its orbit.

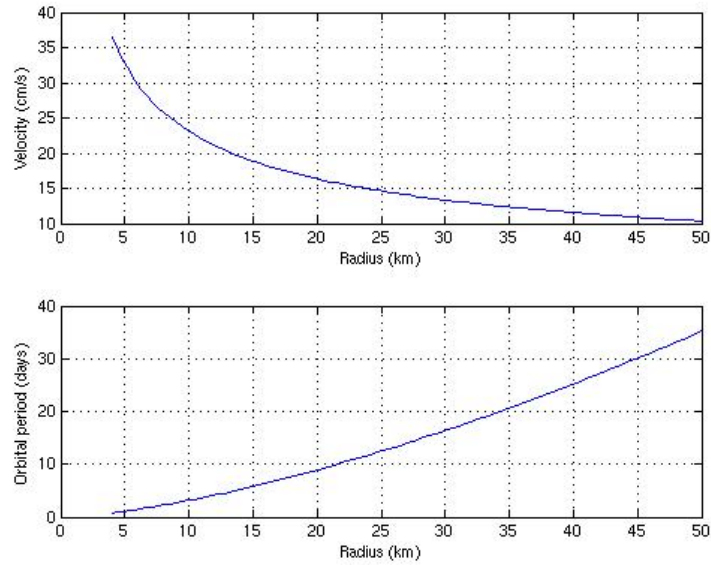


Figure 6: Velocity and period of Rosetta orbiting comet 67P/Churyumov-Gerasimenko.

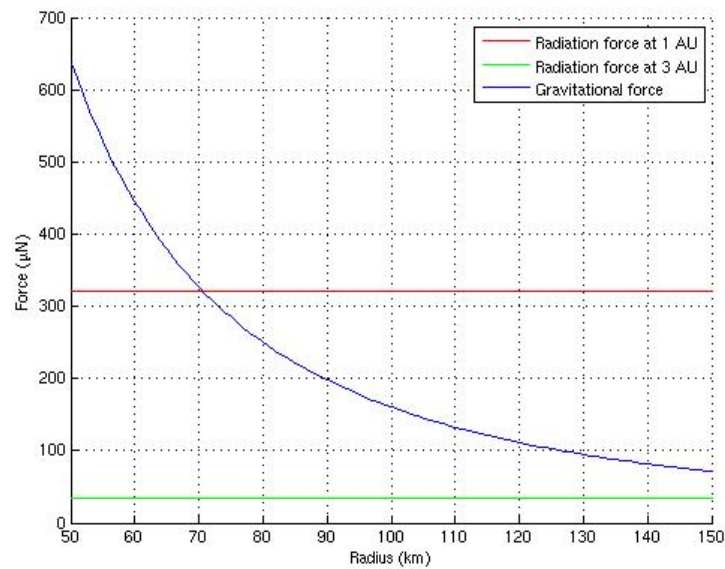


Figure 7: Gravitational force exerted on Rosetta by the target comet, compared with the radiation pressure force from the Sun.

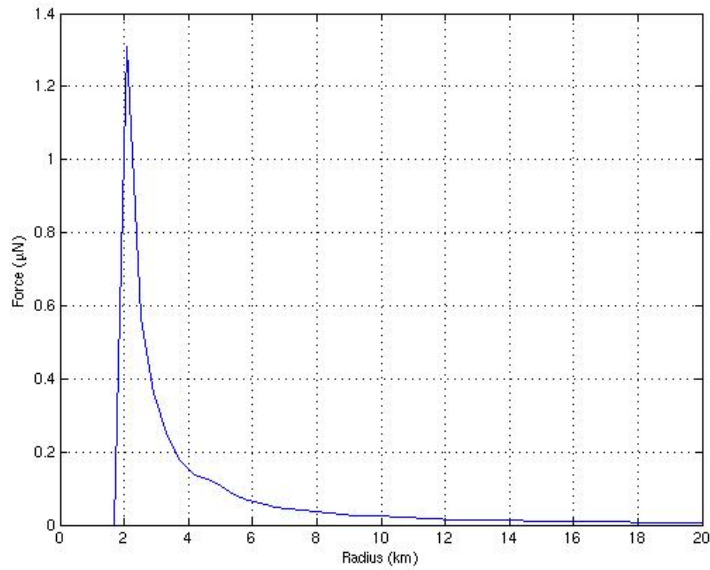


Figure 8: Neutral dynamic force exerted on Rosetta by the target comet at 3 AU.

4.6 Trajectory Plots

In Figure 9, the Rosetta and the comet trajectories obtained from the HORIZONS system are both plotted in the HEA system in a 2D view of the ecliptic plane. The marks (x's and +'s) are indicating simultaneous events and here it can be seen that the comet is actually approaching Rosetta, not the other way around, or as seen in a comet centered frame - Rosetta is approaching the comet from the sunward side. This can also be seen in the CSO system, Figure 10, where the positive x -axis is pointing towards the Sun.

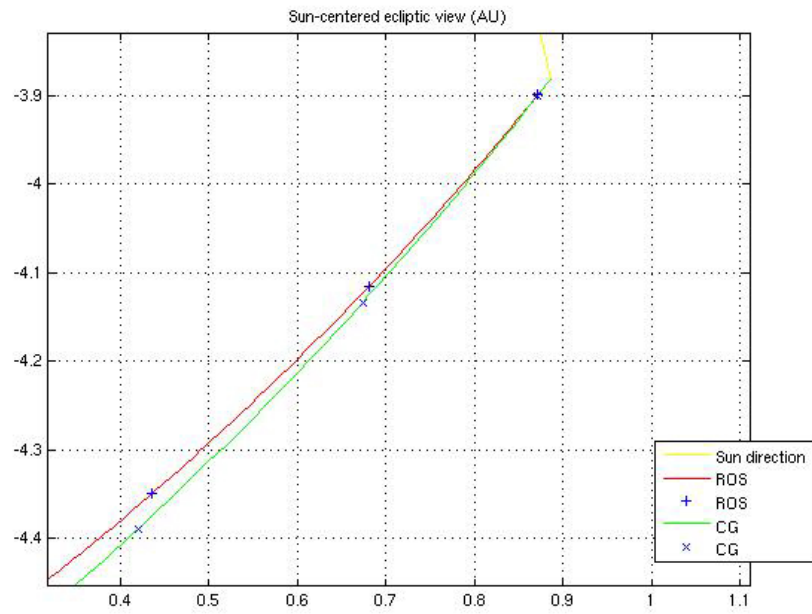


Figure 9: Heliocentric 2D view of the Rosetta and the comet trajectories in the ecliptic.

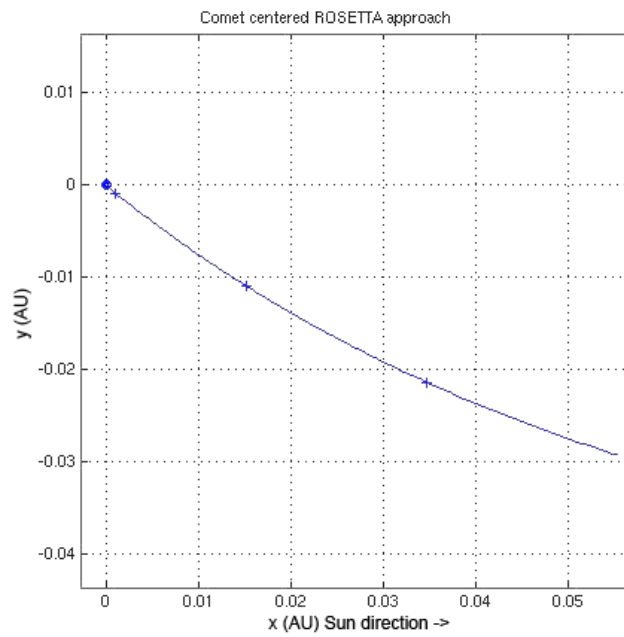


Figure 10: Comet centered 2D view of Rosetta's approach.

5 Plasma Environment Model Results

This section will present the results from the ICES Hybrid, MHD, and DSMC models and discuss the outcome of these in the four different cases. To get a satisfied visual appearance of the comet environment, the cometocentric distances 150 km, 1000 km, 4000 km, and 8000 km have been used for the four cases 3.3 AU, 2.7 AU, 2.0 AU, and 1.3 AU respectively. For convenience, the figures are placed at the end of each subsection.

As is discussed in Section 3, the comet's low gas production rate near the beginning of the mission leads to that the cometary boundaries move close to the comet. The result is that the gyro-radius of the ions is quite large compared to the extent of the plasma structures. While the comet is in this state, the Hybrid model, which includes finite gyro-radius effects, is required to accurately describe the plasma. However, when 67P/CG is closer to perihelion and the gas production rate is larger, the fluid description of the plasma becomes valid and the MHD model can be used. Each of these two models has different strengths and weaknesses which are described below.

5.1 Coordinate System

The coordinate system used in the models is defined as:

- x : Points from the comet to the Sun;
- y : Perpendicular to the x -axis together with which it spans the ecliptic plane. It then points in a sense that is retrograde to planetary motion. This plane is the one containing the solar wind magnetic field when a simple Parker Spiral is used;
- z : Perpendicular to the x and y axes and positive towards ecliptic north.

In terms of the coordinate systems discussed in Section 4.2 this system is given in CSO-coordinates with the modification that the direction of the z -axis is towards the ecliptic north (which also is the same as the CEC-system but with the x -axis directed towards the Sun). We will from now on call the positive x -direction for Sunward, the negative x -direction for anti-Sunward, the positive y -direction for East, the negative y -direction for West, the positive z -direction for North, and finally, the negative z -direction for South.

5.2 Hybrid Model Results

5.2.1 Heavy Ion Density and Velocity

The Hybrid model regards solar wind protons and cometary ions (mainly H₂O) as separate species. As the cometary ions are much heavier than the solar wind protons (1 amu compared to 18 amu), we hereafter use the notations 'heavy ions' and 'cometary ions' synonymously.

The heavy ion densities are shown in Figure 11 and the heavy ion velocities in Figure 12. Far away from the Sun at 3.3 AU (A in the figures), the cometary activity is extremely weak and the cometary plasma is faint. The cometary ions behave mainly like test particles and, as can be seen in the figures, the pick-up process of freshly ionized cometary particles directs them almost perpendicular to the solar wind flow. For those familiar with the ion tails of comets this perpendicular ion tail may seem odd. However, its generation mechanism is simple. As is described in Hansen et al. (2007), all cometary ions feel mainly the Lorentz force

$$\vec{F}_{hi} = q \left(\vec{E} + \vec{v}_{hi} \times \vec{B} \right), \quad (45)$$

so as the velocity of the newborn ions near the nucleus is very small ($v_{hi} \approx 0$), they feel mainly the electric force qE where E is the interplanetary electric field

$$\vec{E} = -\vec{v}_{sw} \times \vec{B}. \quad (46)$$

Thus the force to the cometary ions is

$$\vec{F}_{hi} = -q\vec{v}_{sw} \times \vec{B}, \quad (47)$$

which is perpendicular to the solar wind flow.

At 2.7 AU the activity of the comet has increased and Figure 11B shows that the maximum ion density has grown by a factor of 10 compared to 3.3 AU. The feedback of the cometary ions to the solar wind is no longer negligible but the ion tail still has a pronounced perpendicular component.

At 2.0 AU the model tells us that the ion tail of the comet has perpendicular and parallel flow components of comparable strength. At 1.3 AU the ion tail is mainly anti-sunward.

5.2.2 Solar Wind Density and Velocity

As can be seen in Figures 13 and 14, the feedback of the faint comet to the solar wind is insignificant at 3.3 AU; no disturbance to the solar wind density or velocity can be seen at all. At 2.7 AU a cone-like downstream structure can be resolved. This structure is just the indication of a Mach cone², caused by the high cometary ion density in the superfast solar wind flow. Further approach of the comet to the Sun evolves the Mach cone, as can be seen in Figures 13C and 14C.

A bow shock is not yet seen at the heliocentric distance of 2.7 AU. However, the structure can be seen to start to form at 2.0 AU and it has clearly arisen at 1.3 AU. At this latter distance, the bow shock is positioned at about 4000 km from the nucleus.

Another boundary that can be resolved is a cometopause. This pause evolves as a function of heliocentric distance and can be identified already at 3.3 AU (Figure 11A). However, at this distance the solar wind completely penetrates the ion tail. Increasing cometary activity at 2.7 AU and 2.0 AU prevents the ion tail penetration more and more and deflects the solar wind protons. This process separates the solar wind protons and the cometary ions and a nearly complete separation is reached at 1.3 AU.

5.2.3 Magnetic and Electric Fields

Figures 15 and 16 shows the evolution of the magnetic field B and the electric field E . Looking at the 3.3 AU cases confirm the expectation that the faint coma only has a weak feedback on the solar wind parameters. At 2.7 AU the magnetic field perturbation lies along the perpendicular ion tail and is a good indicator of the Mach cone. At 2.0 AU the cone shaped structure can still be extracted whereas at 1.3 AU the bow shock is fully developed. The jump of the magnetic field strength at the bow shock is a factor of about 2.5.

The undisturbed electric field is always directed south and maps the plasma structures in a way analogous to the magnetic field. When the solar wind approaches the cometary obstacle it is deflected around the obstacle, as shown in Figure 14. The dominant solar wind deflection is northward and the reaction of the electric field is an anti-sunward rotation due to equation 18 as can be seen in Figures 16B and 16C.

²A Mach cone is a V-shaped disturbance formed by an object moving with a supersonic speed in a dispersive medium (Mamun et al., 2004).

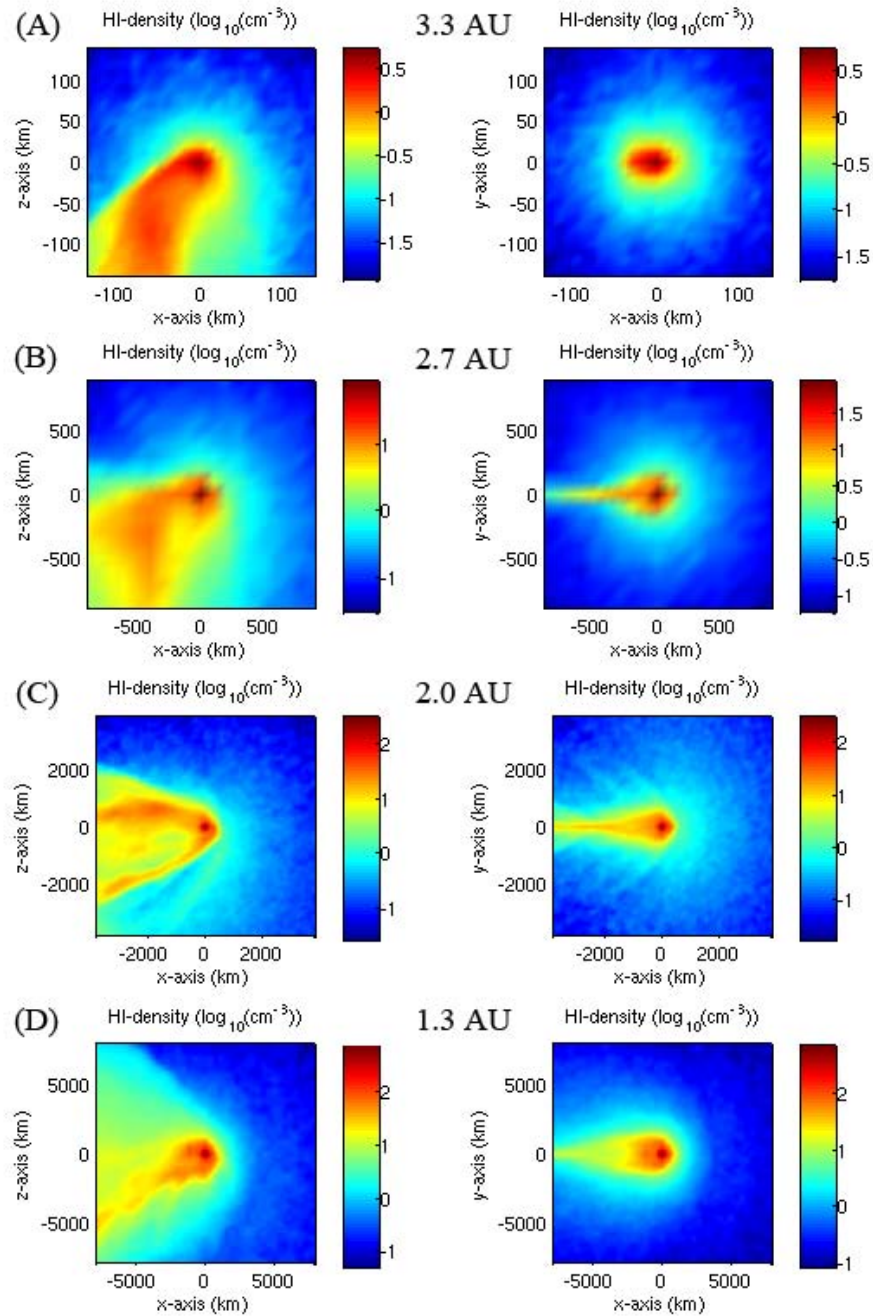


Figure 11: Hybrid model results for the cometary ion densities of 67P/CG at heliocentric distances of 3.3 AU (A), 2.7 AU (B), 2.0 AU (C), and 1.3 AU (D). (Mind the different box sizes.)

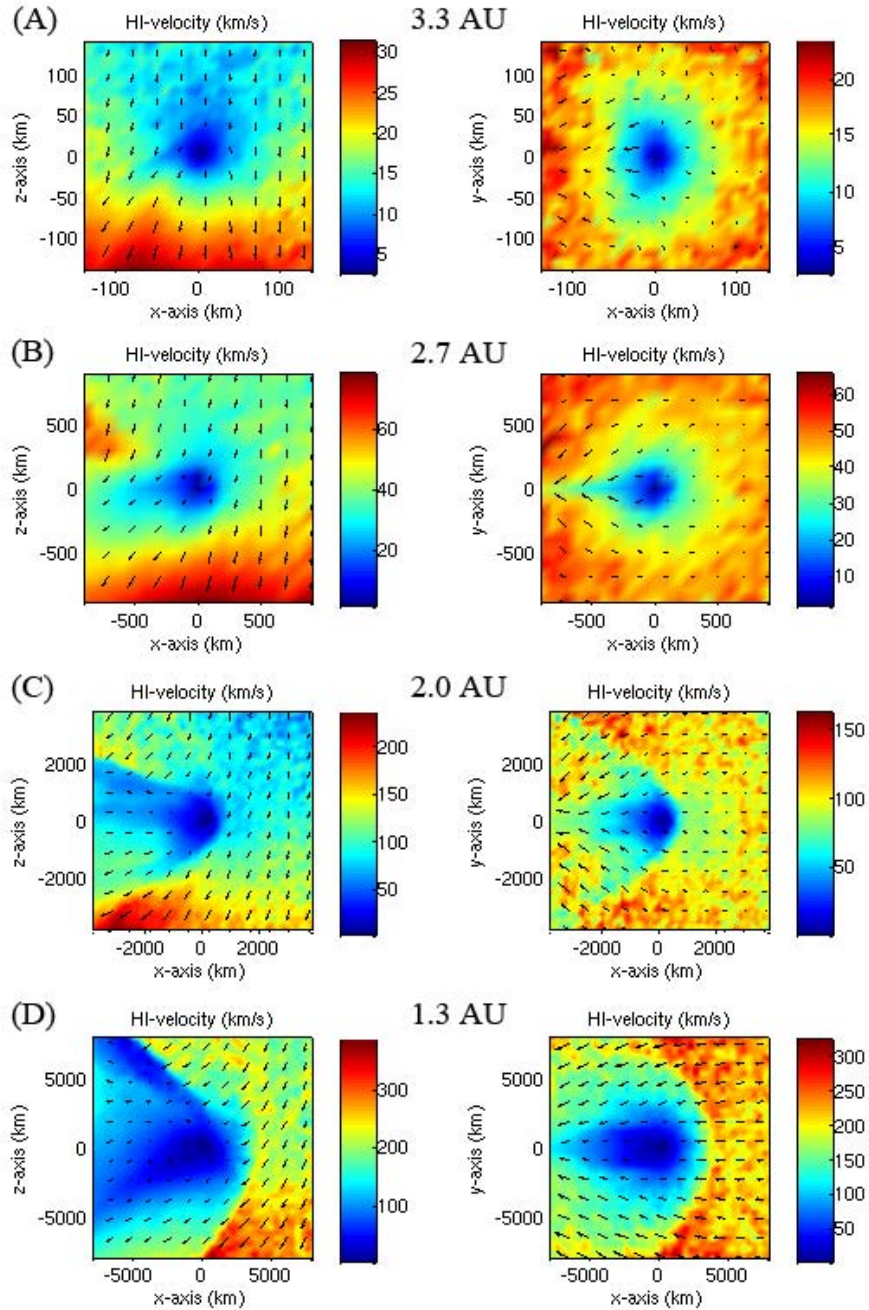


Figure 12: Hybrid model results for the cometary ion velocities of 67P/CG at heliocentric distances of 3.3 AU (A), 2.7 AU (B), 2.0 AU (C), and 1.3 AU (D). (Mind the different box sizes.)

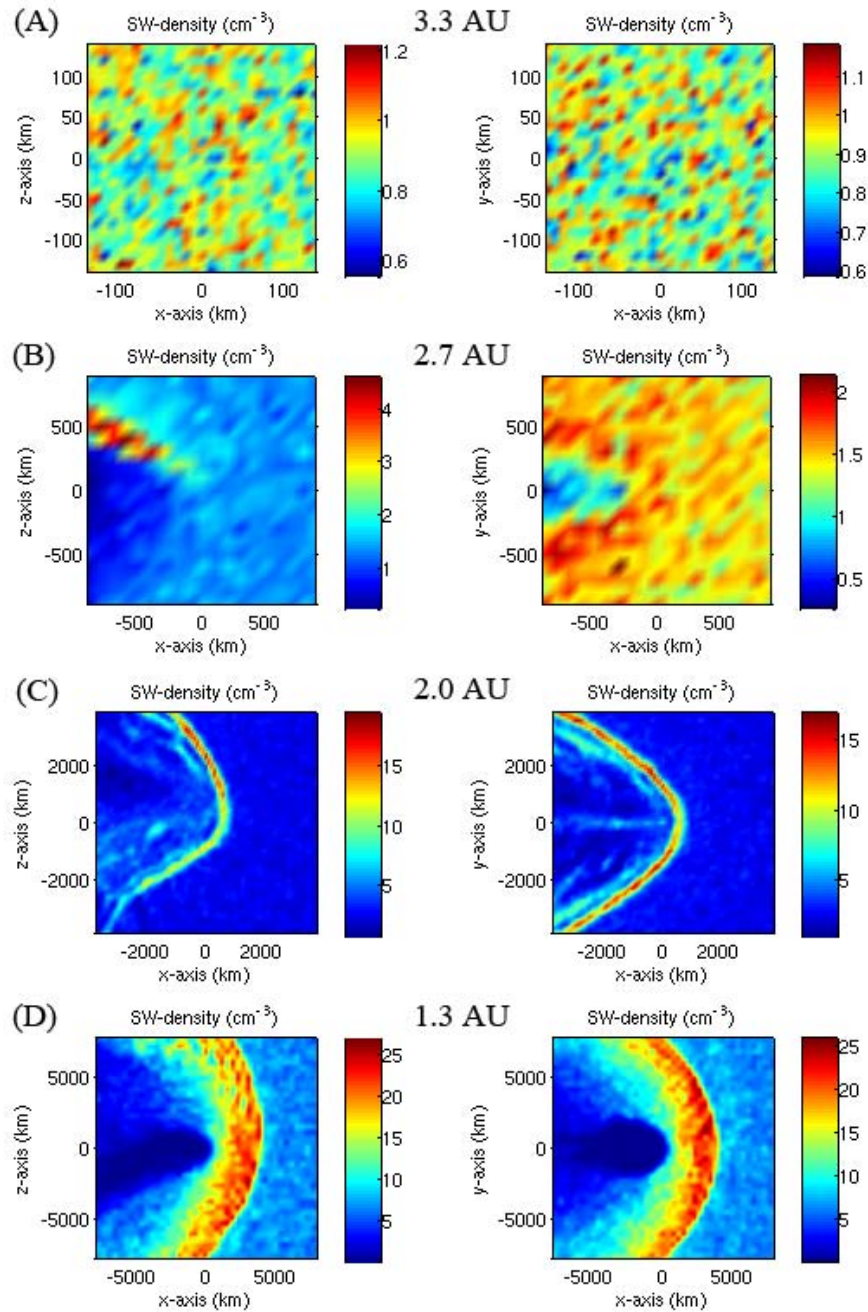


Figure 13: Hybrid model results for the solar wind densities of 67P/CG at heliocentric distances of 3.3 AU (A), 2.7 AU (B), 2.0 AU (C), and 1.3 AU (D). (Mind the different box sizes.)

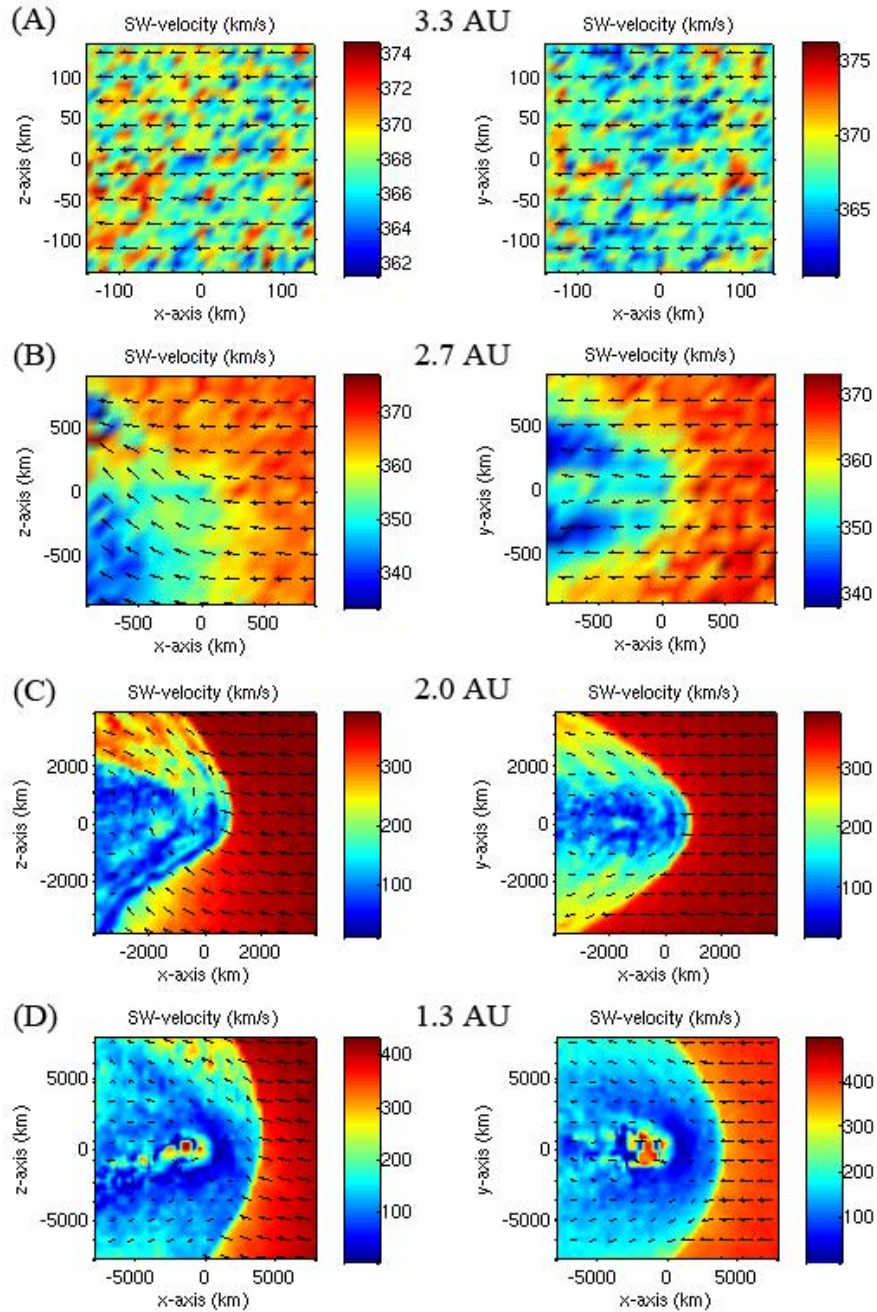


Figure 14: Hybrid model results for the solar wind velocities of 67P/CG at heliocentric distances of 3.3 AU (A), 2.7 AU (B), 2.0 AU (C), and 1.3 AU (D). (Mind the different box sizes.)

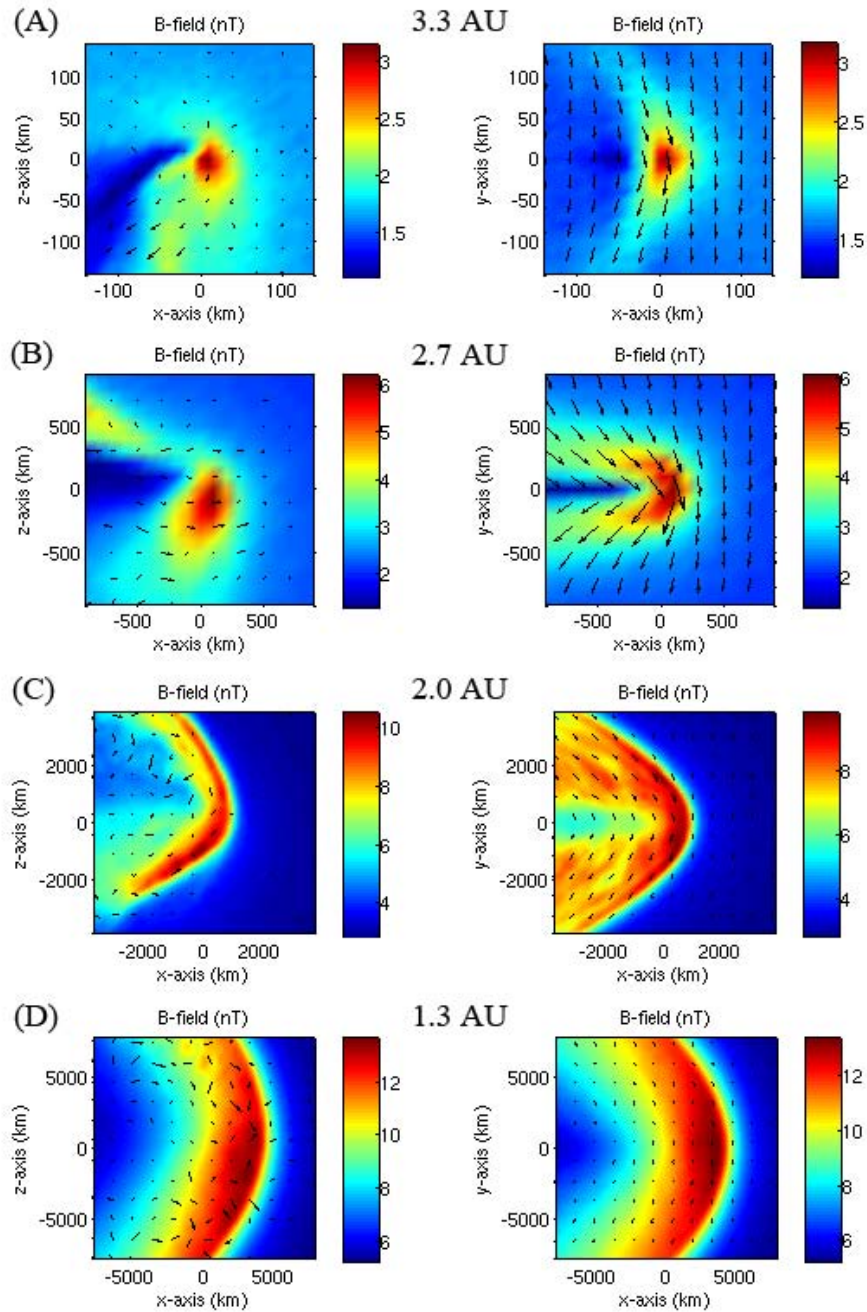


Figure 15: Hybrid model results for the magnetic field of 67P/CG at heliocentric distances of 3.3 AU (A), 2.7 AU (B), 2.0 AU (C), and 1.3 AU (D). (Mind the different box sizes.)

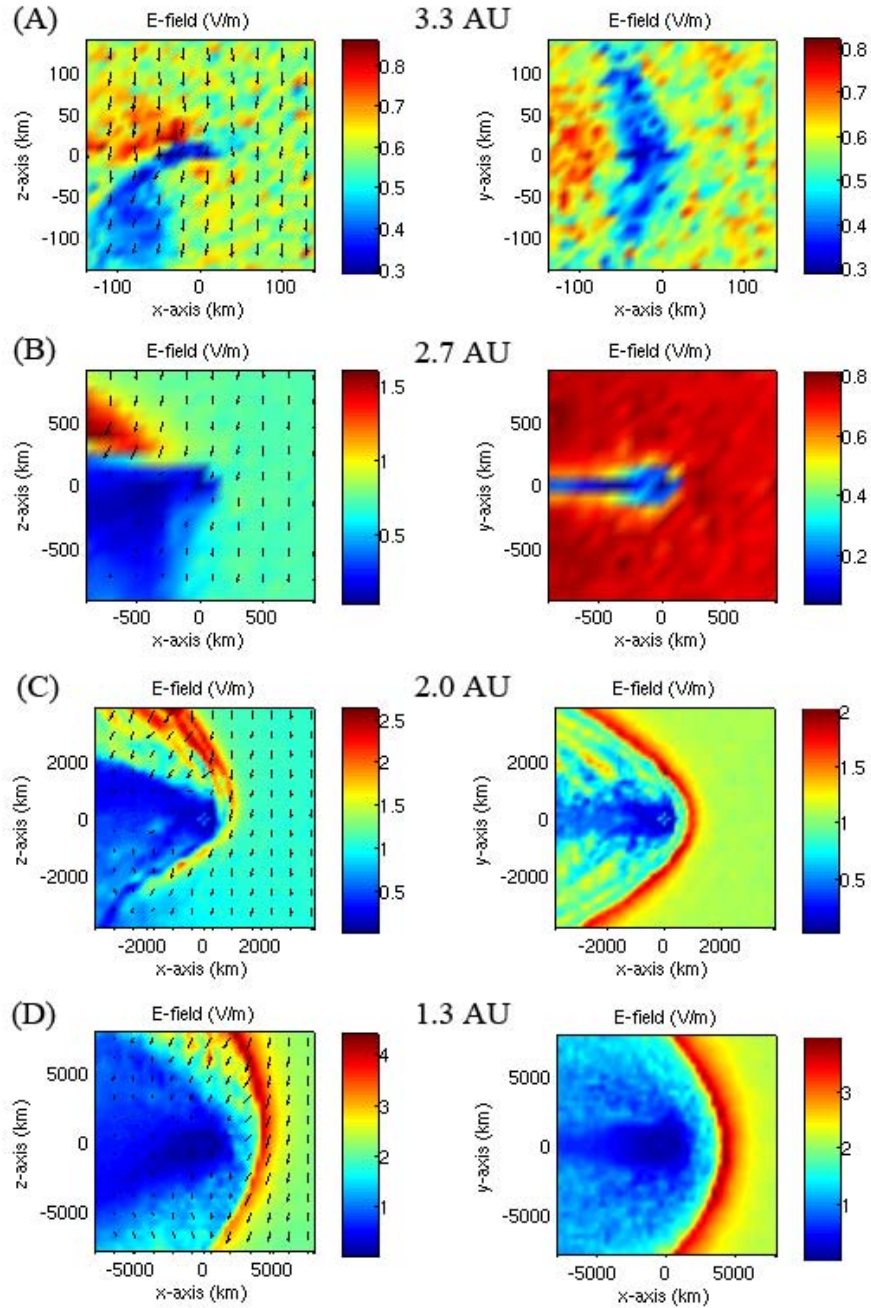


Figure 16: Hybrid model results for the electric field of 67P/CG at heliocentric distances of 3.3 AU (A), 2.7 AU (B), 2.0 AU (C), and 1.3 AU (D). (Mind the different box sizes.)

5.3 MHD Model Results

In this section we look at the results from the MHD model at the same cometocentric distances as for the Hybrid model. As is outlined in Section 3, the comet-solar wind interaction is not well described by MHD when the pick-up ion gyro-radius is much larger than the scale lengths of the cometary coma. Therefore the MHD results are only valid for the 1.3 and 2.0 AU cases (C and D). However, the MHD model runs for the 2.7 and 3.3 AU cases have been included for completeness.

5.3.1 Fluid Density and Velocity

Figure 17 shows the results for the ion (and electron) mass density of the model. Because the model is single species, it is not possible to distinguish the solar wind protons from the cometary ions as in the Hybrid model. The results clearly depict several main features of the interaction that is possible to model with MHD. The cometary ions can be seen to be picked-up well upstream of the bow shock. This results in a gradual slowing of the plasma upstream of the bow shock which can be seen in both the ramping up of the mass density (Figure 17) and the decrease of the plasma velocity (Figure 18). For the 1.3 AU case this is a very important feature; the pick-up well upstream of the bow shock slows and modifies the plasma. It can be seen that the plasma density is about 2.5 times greater just upstream of the bow shock than in the unperturbed solar wind. At the same time, the plasma has slowed dramatically - almost by a factor of 2.

5.3.2 Fluid Temperature

Figure 19 shows the results for the fluid temperature. In the model, the pressure is provided rather than the temperature, so the output then gives the sum of the temperatures, i.e.

$$T = T_e + T_s = \frac{P}{nk_B}, \quad (48)$$

where s indicates the average over all ion species and P and n is given by the model. Hence the sum of the ion and electron temperatures can be determined, but not either individually since we do not know the ratio T_i/T_e . However, from the upcoming discussion on temperatures, the neutral temperature can be used in the instrument model.

5.3.3 Magnetic Field

Figure 20 shows the results for the magnetic field and it can be noted that the field strength is increased by about 50% over the upstream value.

Figures 17-20 clearly show the cometary bow shock which forms at a critical point where the plasma has slowed sufficiently.

5.3.4 The Near Nucleus Environment

Figure 21 shows the innermost part of the comet for the two cases where the MHD model is valid, i.e. 2.0 and 1.3 AU. At this point it can be seen that both cases look relatively similar and differ mainly by the scale over which the interaction occurs. We also see that, although the fraction cannot be determined from MHD, the plasma is mostly comprised of cometary ions, and that the flow of neutrals radially outward from the nucleus results in outward plasma flow which resists the incident solar wind/pick-up ion flow.

The magnetic field pile up in front of the diamagnetic cavity can also clearly be seen and resembles the magnetic field draping described briefly in Section 2.3.

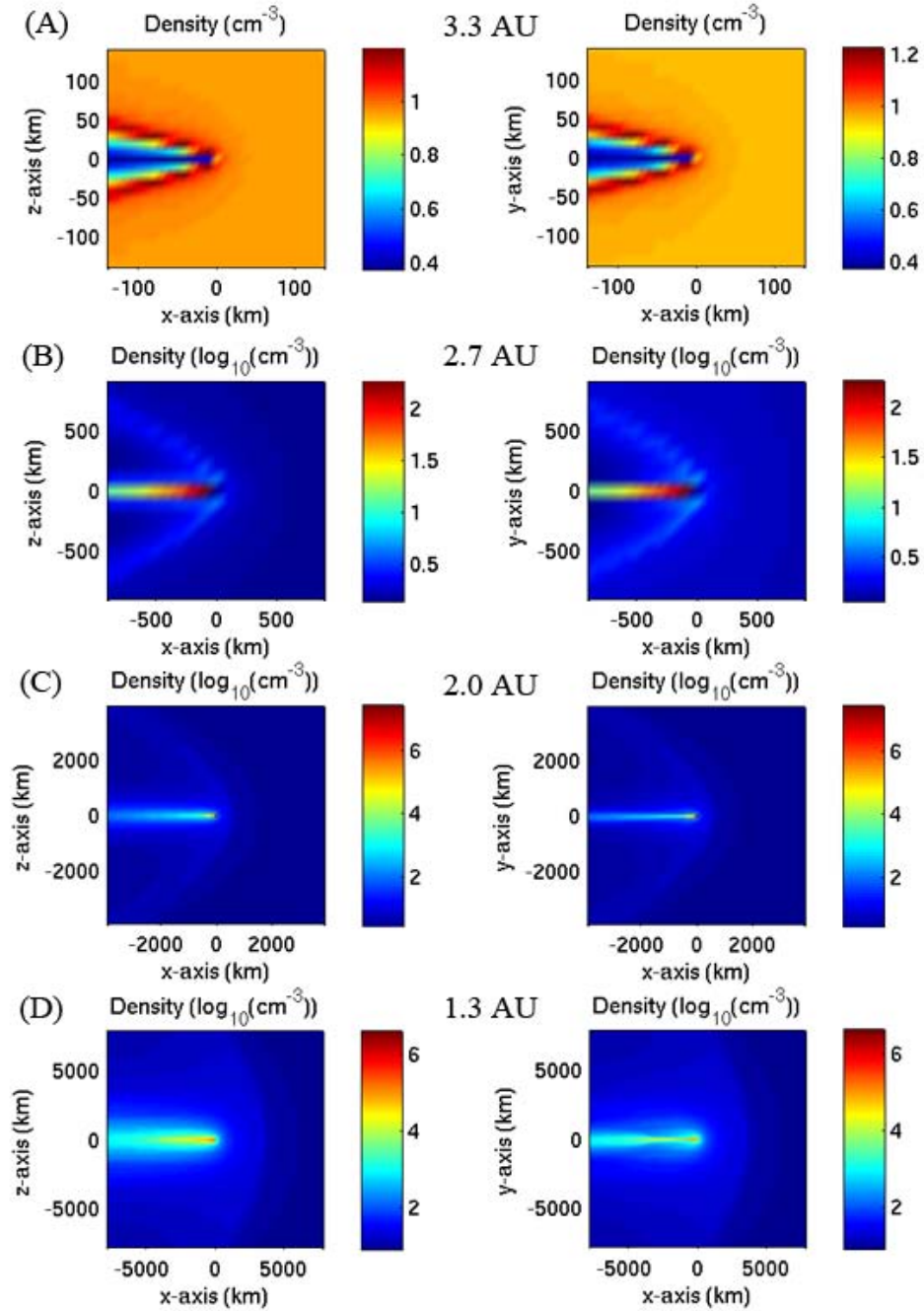


Figure 17: MHD model results for the fluid densities of 67P/CG at heliocentric distances of 3.3 AU (A), 2.7 AU (B), 2.0 AU (C), and 1.3 AU (D). (Mind the different box sizes.)

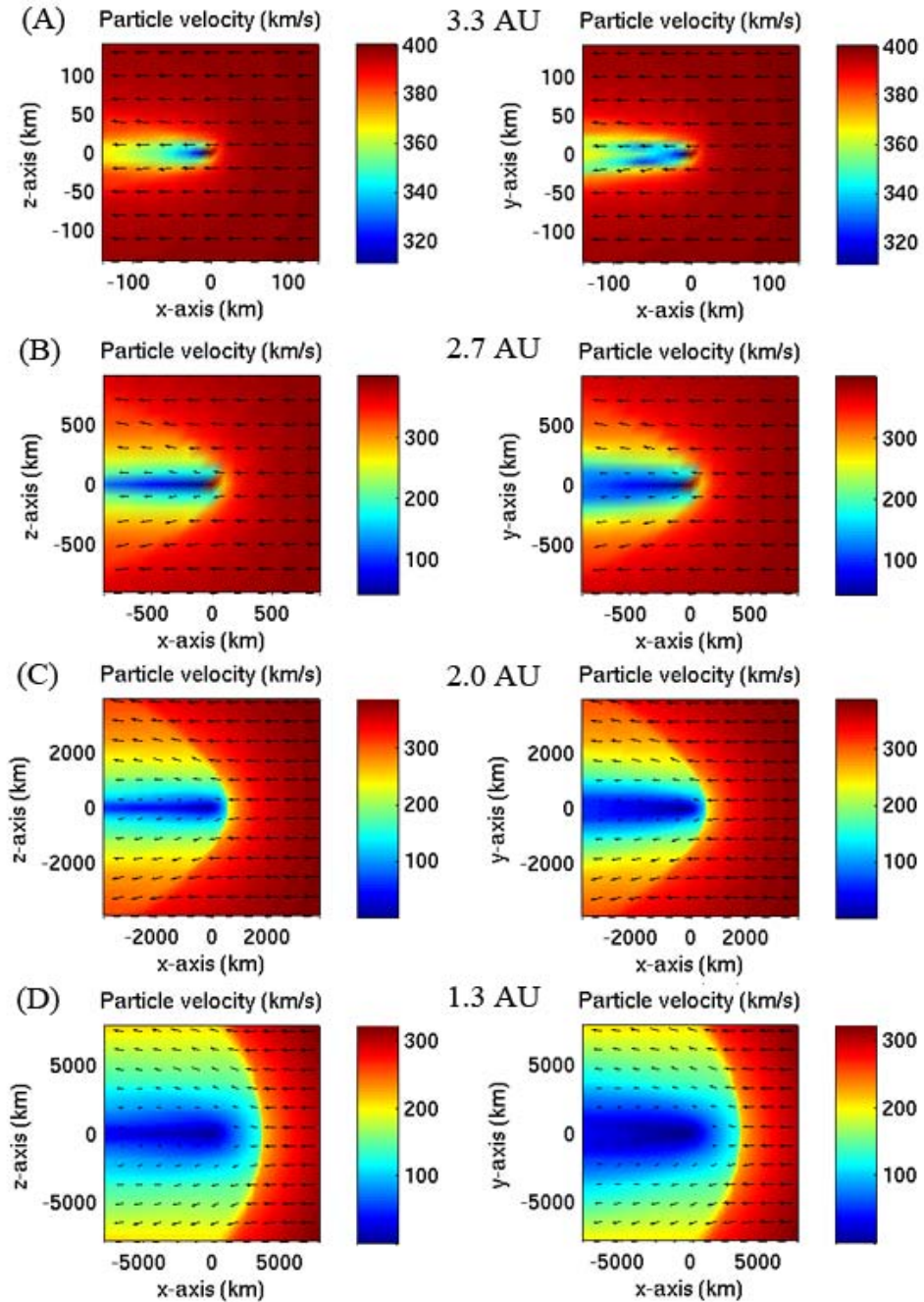


Figure 18: MHD model results for the fluid velocities of 67P/CG at heliocentric distances of 3.3 AU (A), 2.7 AU (B), 2.0 AU (C), and 1.3 AU (D). (Mind the different box sizes.)

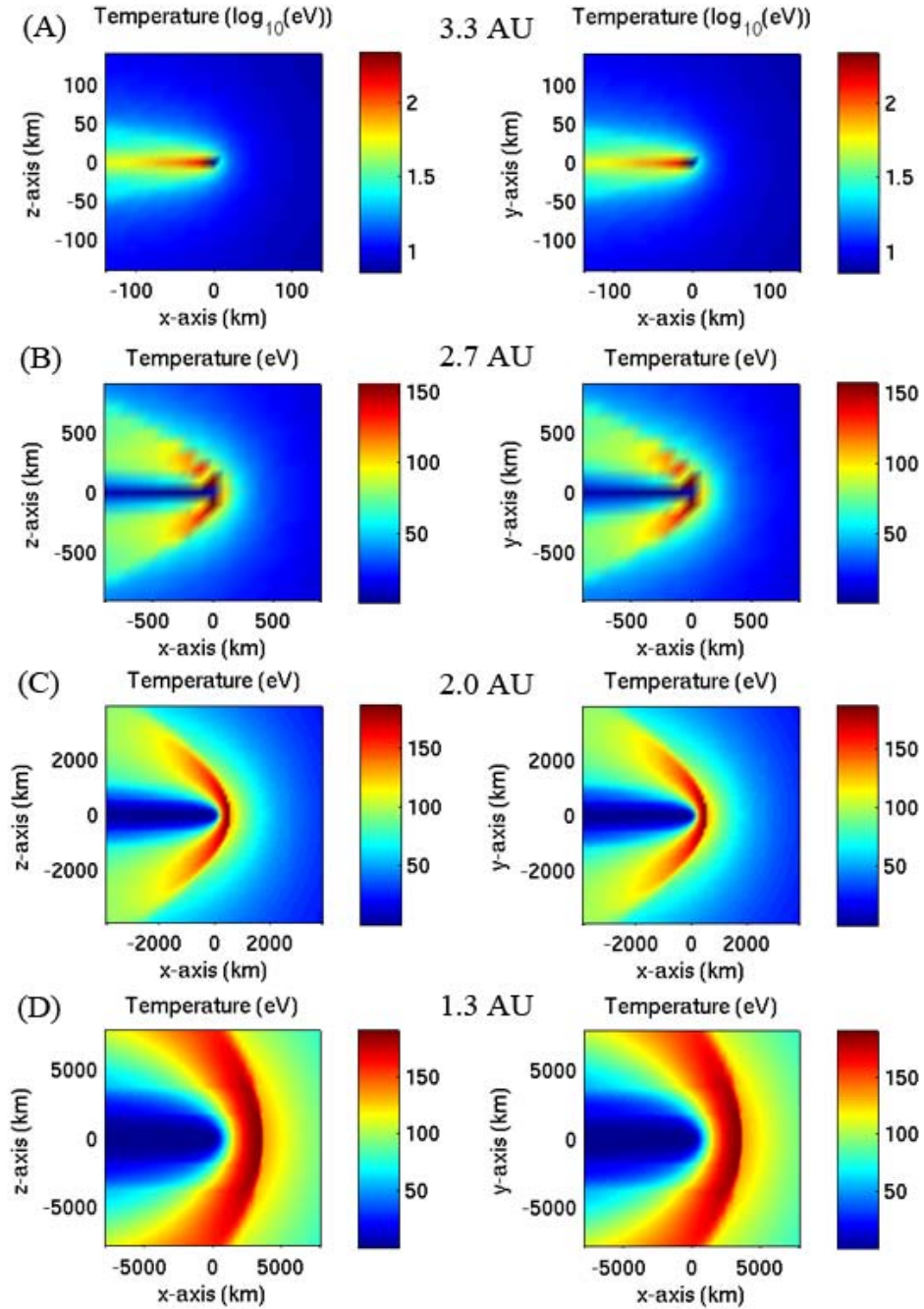


Figure 19: MHD model results of the fluid temperatures of 67P/CG at heliocentric distances of 3.3 AU (A), 2.7 AU (B), 2.0 AU (C), and 1.3 AU (D). (Mind the different box sizes.)

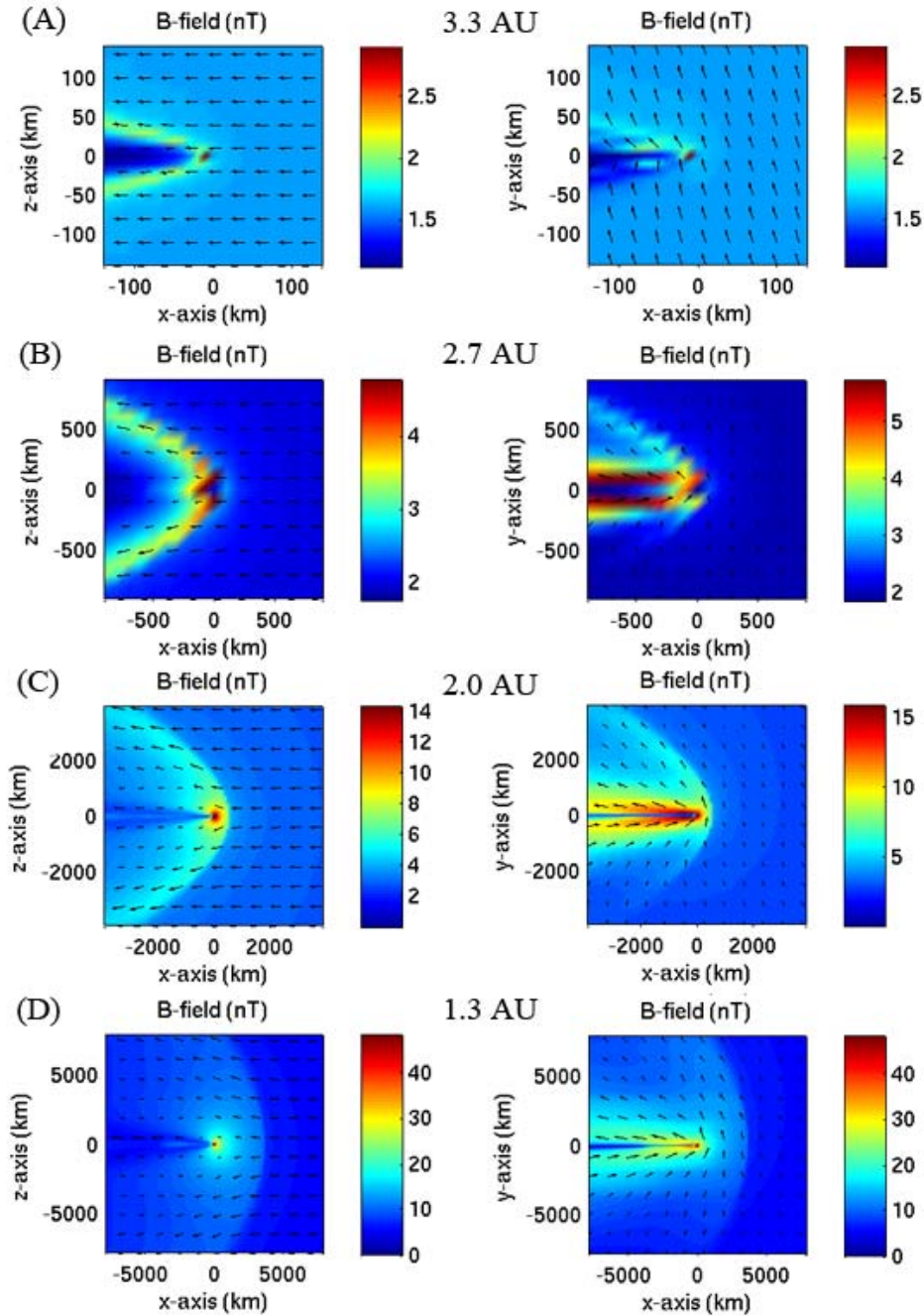


Figure 20: MHD model results of the magnetic fields of 67P/CG at heliocentric distances of 3.3 AU (A), 2.7 AU (B), 2.0 AU (C), and 1.3 AU (D). (Mind the different box sizes.)

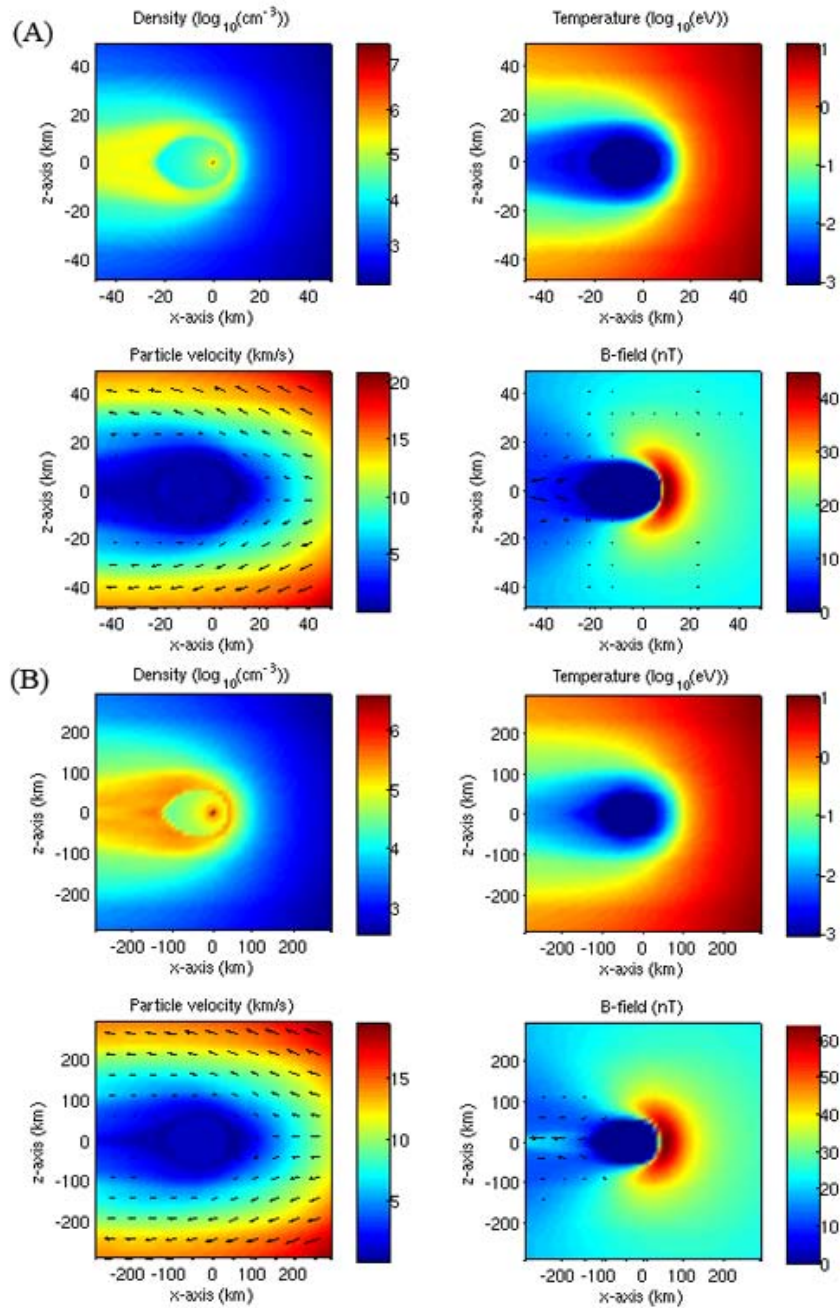


Figure 21: MHD model results at heliocentric distances of 2.0 AU (A), and 1.3 AU (B). (Mind the different box sizes.)

5.4 Comparison of the Hybrid and MHD Models

In the above sections the results from the Hybrid and MHD models of the plasma environment of 67P/CG have been presented. A direct comparison is best near perihelion, where the MHD model is most valid. For this case, the larger production rate produces significant upstream mass loading which leads to a slowing of the plasma. Because the Hybrid model domain is small, the upstream pickup is not captured accurately and the MHD model therefore predicts a better picture of the compression of the shock than the Hybrid model. However, the two models do predict that the bow shock will be positioned at similar distances from the comet.

For cases where the comet is farther away from the Sun the production rate is much lower and the Hybrid model clearly is more accurate; it predicts significant deviations from symmetry and that at 3.3 AU the heavy ion tail will not be anti-sunward but almost perpendicular to the Sun-comet direction, something the MHD model fails to describe. The Hybrid model is clearly a better physical model than the MHD model at these heliocentric distances.

5.5 DSMC Model Results and a Discussion on Temperatures

Models of the electron, ion, and neutral gas temperatures for comet Halley have been reviewed by Ip (1985), Häberli et al. (1996), and Rubin et al. (2009). Because of the close coupling of the electrons to the neutral gas, the electron temperature follows that of the neutrals out to a few thousand kilometers, beyond which it rapidly increases to $10^3 - 10^4$ K. The target comet of Rosetta, 67P/CG, is considered to be a similar comet and the neutral temperature from the DSMC model could then be used as a reference for electron temperatures out to a cometocentric distance of 10^3 km.

As the primary species, water dominates in the thermodynamic balance of cometary comae through its photodissociation and radiational cooling. In Tennishev et al. (2008) a conclusion is that, at small heliocentric distances, the extensive momentum exchange in the innermost coma causes a collisional coupling between its components, which results in a decrease of temperature of daughter species that would otherwise be determined only by the energy excess of photolytic processes and have a higher value. Because of this coupling their macroscopic parameters follow the variation of water density from the day to the night side of the nucleus. The same article, Tennishev et al. (2008), presents a result that shows that the neutral temperature lies in the range 1 – 10 K for the cometocentric distances 100 – 10000 km at 1.3 AU and 2.0 AU and in the range 15 – 25 K for the same cometocentric distances at 2.7 AU and 3.3 AU. This compares well with the result obtained from the DSMC model presented in Figure 22. The same figure however shows some very confusing patterns in the temperature distribution. This appearance could not be resolved and probably shows a fault in the model. Therefore the creators have been contacted so that possible errors can be corrected.

These results show clearly that the increased water production when getting closer to the comet results in a decrease of temperature at the dayside of the nucleus (+x direction). Therefore the conclusion was made to use the neutral temperature from the DSMC model when treating the two cases closest to the Sun, i.e. 2.0 AU and 1.3 AU.

However, when considering the collisions between neutrals and ions/electrons, i.e. using equation 15, it is obvious that this can not be the case for all heliocentric distances. When the order of magnitude of the mean free path gets considerably larger than the cometocentric distance, the molecules do not exchange information and hence the temperatures differ. The collisions of the heavy ions and electrons with the neutrals was calculated using equation 15 and is tabulated in Table 15. Here we can see that the collision length is smaller than, or comparable with, the cometocentric distance only for the two cases 1.3 AU and 2.0 AU and hence we need to make another approach to find the ion and electron temperatures at greater heliocentric distances.

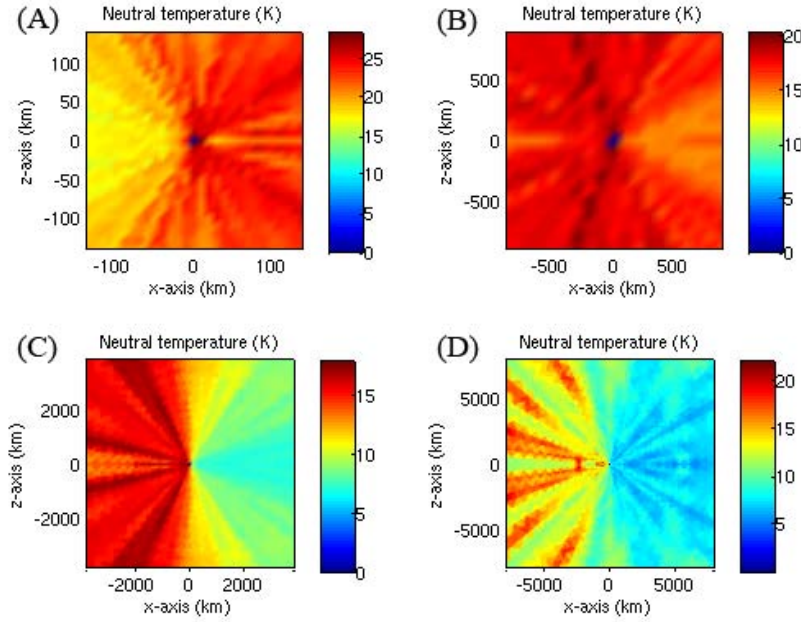


Figure 22: DSMC (Direct Simulation Monte Carlo) model results of the neutral temperature of 67P/CG at heliocentric distances of 3.3 AU (A), 2.7 AU (B), 2.0 AU (C), and 1.3 AU (D). The results look a little odd and this is discussed further in the text. (Mind the different box sizes.)

Following the discussion in Section 3.1.1, the electron temperature for the cases 3.3 AU and 2.7 AU was chosen to be kept constant at 1 eV which is slightly lower than the solar wind temperature. The ion temperature, which should be a mixture of the slightly colder cometary ions and the solar wind protons, was chosen to be 0.1 eV.

Table 15: Mean free path at a cometocentric distance of 5 km in the terminator plane.

| R_{\odot} (AU) | λ_{HI} (m) | λ_e (m) |
|------------------|--------------------|-------------------|
| 3.3 | $2.8 \cdot 10^6$ | $11.2 \cdot 10^6$ |
| 2.7 | $3.3 \cdot 10^4$ | $13.2 \cdot 10^4$ |
| 2.0 | $4.4 \cdot 10^3$ | $17.6 \cdot 10^3$ |
| 1.3 | 780 | 3120 |

6 Instrumentation

Rosetta's payload comprises 12 scientific instruments and instrument groups on board the orbiter and 10 on the Rosetta lander Philae (Glassmeier et al., 2007a). The instrument interesting for this work is the Langmuir Probe (LAP) operated by IRF Uppsala, one of five instruments of the Rosetta Plasma Consortium (RPC). In Section 7, we will also present some results on magnetic fields, to be measured by the flux gate magnetometer MAG, also included in the RPC (Glassmeier et al., 2007b).

The LAP uses a pair of spherical Langmuir Probes to measure basic plasma parameters. The fundamental plasma properties to be studied are the plasma density, electron temperature, and plasma flow velocity (Eriksson et al., 2007). Table 16 contains a summary of parameters and their ranges accessible to LAP.

Table 16: Summary of parameters and their ranges accessible to LAP (from Eriksson et al., 2007).

| Quantity | Range |
|-----------------------------|--|
| Plasma density | $1 \text{ cm}^{-3} - 10^6 \text{ cm}^{-3}$ |
| Electron temperature | $\sim 10 \text{ meV} - 10 \text{ eV}$ ($100 \text{ K} - 10^5 \text{ K}$) |
| Plasma drift velocity | Up to 10 km/s |
| Electric field fluctuations | Up to 8 kHz |
| Plasma density fluctuations | 0.05 - 50% |
| Spacecraft potential | $\pm 30 \text{ V}$ |
| Effective ion mass | 1 - 100 amu |

6.1 Langmuir Probes

Langmuir probes are commonly used for measuring plasma properties. One applies a controlled potential to the probe and then measures the current collected by the probe. Varying the potential will cause the current to vary and the resulting current-voltage relationship (further explained in Section 6.4) is useful for determining the plasma density and temperature. The applied potential is the known driving force while the current is the response which is to be measured.

The LAP sensors consist of spheres with a radius of 2.5 cm mounted on 15 cm long 'stubs' which, in turn, are mounted to the ends of long booms (see Figure 23). The spheres are made of titanium with a coating of titanium nitride and are electrically insulated from the stubs, which nevertheless are held at the same potential as the spheres.

Probe 1 (LAP1) is mounted on the 'upper' spacecraft boom which is 2.24 m long. By pointing to the comet, LAP1 will measure the plasma flow from the comet as undisturbed as possible by any spacecraft sheath or wakes. LAP2 is mounted on the 'lower' spacecraft boom, being 1.62 m long and giving a distance of 5.00 m between the probes (Eriksson et al., 2007).

If a probe is exposed of sunlight, photoelectrons may be emitted from the probe and the spacecraft and dominate over the plasma particles surrounding the spacecraft. This makes the probe currents collected misleading for inferring the plasma parameters. In order to minimize this effect, the position of the LAP probes on Rosetta has been chosen to increase the probability of one of them being shadowed by the spacecraft.

The LAP electronics are connected to two circuit boards; one holding the digital processing unit (DPU) and the other (working as an interface between the DPU and the LAP sensors) containing the analog electronics doing the actual measurement. The electronics are designed in such a way that the



Figure 23: One of the two LAP probes, to scale (by courtesy of IRF Uppsala).

two probes can be operated independently of each other and hence operated in the same or different bias mode (voltage or current bias), further explained below.

The basic principles of the Langmuir probe, as briefly described above, may be very simple, but the theoretical description of its response is very complicated and in order to do any kind of work we need to use approximations to the theory. Hence the problem of modeling the current to a probe in a plasma is difficult but, however, there exist some simplified expressions in the limits with regard to the density characteristics of the plasma. We have two limits; sheath limited (SL) or orbital motion limited (OML). In the SL case there is a very dense plasma and the Debye length will be much smaller than the probe radius, while in the OML case the plasma is very tenuous and the Debye length will be much larger than the probe radius.

6.2 Measurement Modes

The bias voltage sweep is the standard measurement technique for measuring electron number density and electron temperature by Langmuir probes. These parameters (among others) are inferred by recording the current collected by the probe while varying the probe potential with respect to the spacecraft and comparing this with the theoretically predicted current-voltage relations (Eriksson et al., 2007).

If the potential of the probe with respect to the plasma is set positive, electrons will dominate the current collected and the electron number density together with the electron temperature can be determined, the latter if it stays above a certain limit depending on the spacecraft electrostatic cleanliness and stability as well as on the homogeneity of the probe surface. If the temperature goes below this limit, only combinations of the density and temperature can be obtained (Eriksson et al., 2007).

If the potential of the probe with respect to the plasma is set negative, positive ions will be collected and if the ion flow is supersonic, an average ion drift kinetic energy can be derived.

If one, instead of varying the probe potential, keeps the probe bias voltage constant, it is possible to study the changes in the probe current caused by variations in plasma density and temperature. By assuming isothermal or adiabatic conditions, the relative electron density variations can be estimated up to a certain frequency, where the capacitive coupling to the plasma starts dominating and the probe current variations reflect fluctuations in the electric field rather than in the plasma density.

Another mode possible is to operate the probes with a controlled bias current, giving a measured quantity V_{PS} that is the potential between the probe and the spacecraft. By dividing the difference in V_{PS} for the two probes with the probe separation one gets an estimate of the electric field. It is also possible to leave the probe potentials floating freely, without any bias current applied. This is usually advantageous for electric field measurements in dense plasmas (Eriksson et al., 2007).

The two probes can be individually biased within the range ± 31 V and bias sweeps can be performed over the full measurement range at resolutions down to 0.25 V. In the inner coma, low electron temperatures are predicted and to properly resolve these low values, high-resolution sweeps can be performed at step sizes down to 10 mV over ± 1.2 V around an offset bias which can be set to values in the range -8

V to +9 V. Two analog-to-digital converters (ADCs) are connected to each probe; one 16 bit, operating at 18 750 samples/s, and one 20 bit, acquiring 57.8 samples/s.

To provide flexibility over the mission lifetime, the instrument operational modes are defined as ‘macros’, i.e. repeatable command sequences. These macros can control any aspect of the instrument, including bias modes, bias values, measurement range, sweeps, etc. Some of the presently available macros are described in detail in Eriksson et al. (2009). The macro simulated in this work is Macro ID 604 which uses 16-bit ADC bias voltage sweeps with a resolution of 0.25 V over the range -30 V to +20 V.

6.3 Probe Currents

The basic reference for orbital motion limited current collection in a plasma is the study by Mott-Smith and Langmuir (1926). We will build the presentation in this section on the summary by Engwall (2006).

If we consider a charged particle with orthonormal velocity components u , v , and w at a distance r from an *uncharged* spherical probe with radius a in a region so far from the probe that absorption by the probe does not affect the plasma, the Maxwellian distribution function is given by

$$f(u, v, w) = n \left(\frac{m}{2\pi kT} \right)^{3/2} \exp \left(-\frac{m}{2kT} (u^2 + v^2 + w^2) \right). \quad (49)$$

In this treatment, the velocity component u gives the radial velocity, positive when directed towards the probe, and v and w are the tangential components.

The current from the probe to the plasma is created by plasma particles hitting the probe, so only particles with positive radial velocities will contribute to the current. The particle flux to a probe at zero potential with respect to the plasma is given by

$$\Phi = n \sqrt{\frac{kT}{2\pi m}}, \quad (50)$$

and that the number of particles per second hitting a spherical surface of area S centered at the probe is

$$\eta = S\Phi. \quad (51)$$

The current to the probe is then obtained by multiplying the expression above by the particle charge, so

$$I_0 = 4\pi a^2 n |q| \sqrt{\frac{kT}{2\pi m}} = 4\pi a^2 n |q| v_{th}, \quad (52)$$

where $v_{th} = \sqrt{\frac{kT}{2\pi m}}$ is the thermal velocity. The expression in equation 52 above is the *random current* to a probe in a Maxwellian plasma.

If we now charge the spherical probe with a potential V_p with respect to the plasma, the probe will be shielded by charges of opposite sign; a negatively charged object will be shielded by a cloud of positive ions and vice versa. Together the shielding particles form a *sheath*, beyond which the potential from the object will not reach. Inside the sheath, the plasma is disturbed by the potential from the probe and the distribution function deviates from the Maxwellian distribution in such a way that it is constant along a particle trajectory. Since the plasma is undisturbed outside the sheath, the distribution function at the sheath edge s is taken again to be a Maxwellian. By letting the sheath expand to infinity, the current to the probe is given by

$$I = \begin{cases} -I_0 \left(1 - \frac{qV_p}{kT} \right), & \text{for } qV_p < 0 \text{ (attractive potentials)} \\ I_0 \exp \left(-\frac{qV_p}{kT} \right), & \text{for } qV_p > 0 \text{ (repulsive potentials)} \end{cases}. \quad (53)$$

When $V_p = 0$, $I = I_0$ as expected.

Furthermore, it can be shown (Engwall, 2006) that a probe inserted in a flowing plasma receives a current according to

$$I = \begin{cases} \pi a^2 q n v_d \left(1 - 2 \frac{q V_p}{m v_d^2}\right), & \text{for } V_p < \frac{m v_d^2}{2q} \\ 0, & \text{for } V_p \geq \frac{m v_d^2}{2q} \end{cases}, \quad (54)$$

where the constraint is due to that, for repulsive potentials, the velocity of the particle has to be sufficiently high to enable it to overcome the potential barrier and reach the probe. This lower limit is given by $v = \sqrt{2qV_p/m}$.

The above discussion can be used to separate the different currents received by ions and electrons for positive or negative potentials. The result is

$$V_p < 0: \quad \begin{aligned} I_e &= I_e^0 \exp\left(\frac{eV_p}{kT_e}\right), \\ I_i &= -I_i^0 \left(1 - 2 \frac{q_i V_p}{m u^2}\right), \end{aligned} \quad (55)$$

$$V_p > 0: \quad \begin{aligned} I_e &= -I_e^0 \left(1 + \frac{eV_p}{kT_e}\right), \\ I_i &= \begin{cases} I_i^0 \left(1 - 2 \frac{q_i V_p}{m u^2}\right), & \text{for } V_p \leq \frac{m u^2}{2q_i}, \\ 0, & \text{else.} \end{cases} \end{aligned} \quad (56)$$

In addition to plasma ion and electron currents, we have to regard the current due to photoelectrons emitted by the probe. For negative potentials all photoelectrons can escape from the probe and the photoelectron current will be saturated at a constant value. However, probes at positive potentials will recollect some of the photoelectrons and the current due to this can be approximated by

$$I_{ph} = \begin{cases} I_{ph}^0, & \text{for } V_p < 0, \\ -I_{ph}^0 \exp\left(-\frac{eV_p}{kT_{ph}}\right), & \text{for } V_p > 0, \end{cases} \quad (57)$$

where

$$I_{ph}^0 = \pi a^2 j_{ph}^0, \quad (58)$$

with the photo saturation current j_{ph}^0 and the photoelectron temperature T_{ph} which is of the order of 1.5 eV.

In practice, another contribution to the current from the LAP probes is due to collections of photoelectrons emitted by the spacecraft body and the solar panels. We make no attempt to model these here, but discuss their impact in relevant parts of Section 7. As a rule of thumb, this current can be estimated to follow the relation $j_{ph}^0 \cdot \frac{V_b}{10[\text{V}]}$ (A. Eriksson, personal conversation, 2009).

6.4 The I-V Curve

As is mentioned in Section 6.1, a Langmuir sweep will result in a current-voltage relationship most conveniently plotted as an I-V curve. A typical I-V curve from a Langmuir probe is shown in Figure 24 and the qualitative behavior of the I-V curve can be explained as follows³.

The first current to be considered is the photocurrent: if the probe potential is negative compared to the plasma around it, all of the liberated photoelectrons will flow out into space. If, on the other hand, the probe potential is positive, some of these photoelectrons are attracted back to the sphere, reducing

³Following <http://www.cluster.irfu.se>.

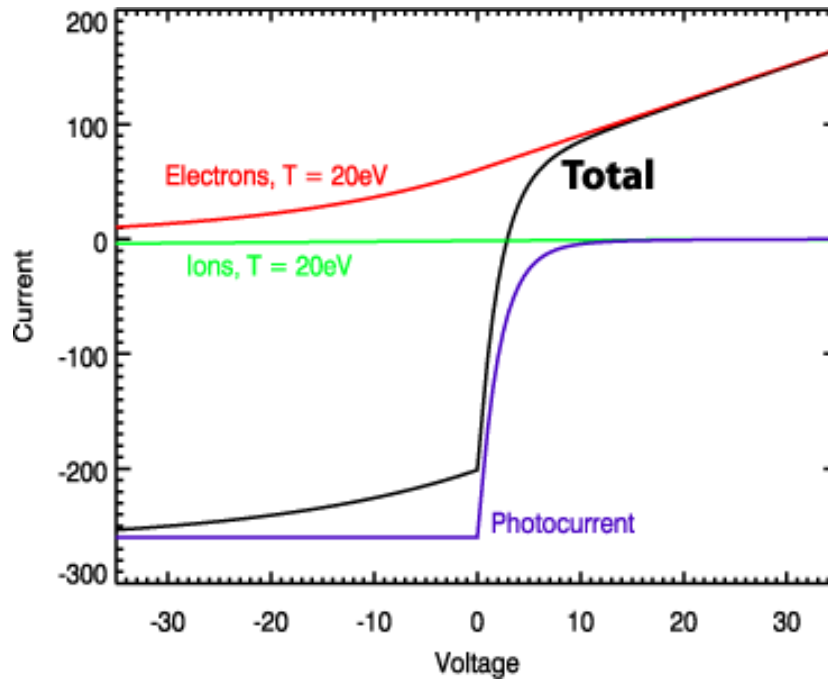


Figure 24: A typical I-V curve from a Langmuir probe (adapted from <http://www.cluster.irfu.se>).

the current. The energy of the emitted photoelectrons is small, so the net photocurrent falls very rapidly for potentials above 0 V.

Turning now to the electron current: if the probe potential is far negative with respect to the plasma, no electrons will reach the probe. If the probe potential is just a little bit negative, some of the most energetic electrons will reach the probe and as the potential rises the current increases. If the probe potential is positive with respect to the plasma, the probe begins attracting electrons from the surroundings and at sufficiently high potential, the only current is the electron current.

The third and last current considered is the ion current: this current behaves opposite to the electron current. At large positive probe potentials it is zero. At 0 V, the full probes are available. Since the ions move so slowly, the current is much smaller than the electron current and at large negative potentials, the probe attracts ions from the surroundings, resulting in a larger and larger current.

As is implied from the above discussion, for positive probe potentials, electrons will dominate the collected current. The electron number density n_e and the electron temperature T_e can be determined from this part of the curve, if T_e stays above a certain limit. Figure 25 shows an example of a bias sweep for a sunlit probe near the Earth's plasmopause. The red dots are the measured values and the vertical blue line marks the location of the maximum of $\frac{d^2 I_p}{dV_b^2}$ which is a way of approximating the negative of the spacecraft potential, in this case about 3 V.

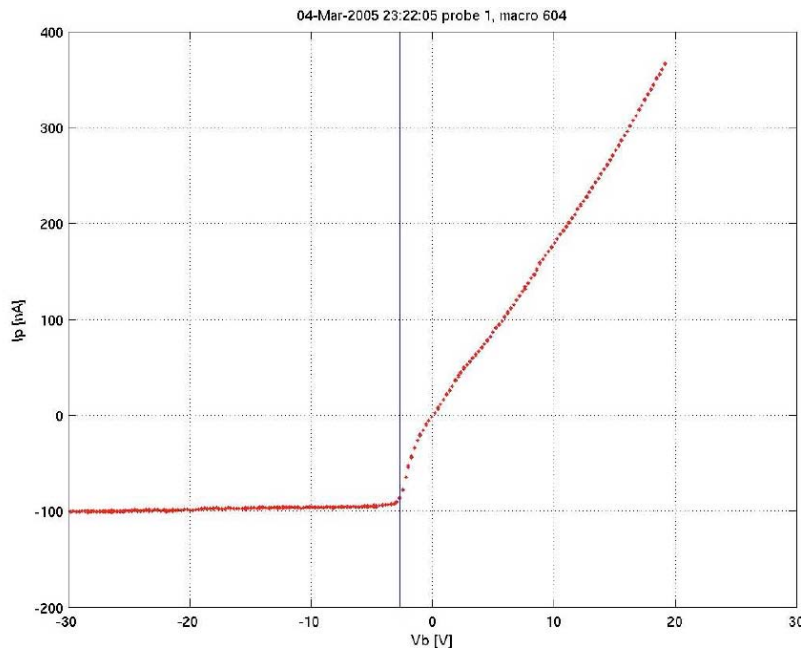


Figure 25: Example probe bias sweep from a sunlit probe near the Earth's plasmopause.

6.5 Spacecraft Charging

In space plasmas, a spacecraft behaves as a Langmuir probe but, unlike in the laboratory, one does not apply a potential to a spacecraft. Instead, the spacecraft potential responds to the currents collected from its environment - if one knows how all the currents depend on potential, one can calculate the potential from the requirement that the sum of all currents flowing to the spacecraft must be zero. In contrast to the laboratory case, the currents are the driving forces while the spacecraft potential is the response.

The current-voltage equation of a spacecraft is similar to that of a Langmuir probe; we just exchange the probe for the much larger spacecraft and the overall picture of currents collected remains the same. However, since a spacecraft seldom resembles a probe in that it is perfectly spherical, we have no exact analytical expression for the currents, but to get a qualitative description we can still use the relations given above.

6.6 Instrument Model

The code used to simulate LAP measurements was originally created by IRF-Uppsala for the Swarm mission and further developed to fit this project. As is described earlier, a Langmuir probe measures the current collected by an application of a controlled potential to the probe, so this model uses the plasma parameters from the ISSI model as input which results in a current. This current is then plotted against the controlled potential which, in turn, can be varied between various intervals to create a sweep.

A flowchart of the model is shown in Figure 26 and, as can be seen, the program first determines if the heliocentric distance modeled is one of the cases closest to perihelion or one of the outer two; this is to make a decision on which plasma model to receive data from, i.e. the MHD or the Hybrid model. The data is loaded into memory and the plasma parameters are set up. When this is completed the program

calculates the spacecraft potential; this is done by first calculating the theoretical currents, determining if the potential is positive or negative, and finally calculating the corresponding potential. The spacecraft potential is then added to the bias potential to create the probe potential, V_p .

When all this is done it is time to calculate the probe currents and for this the model uses the same unmodified codes as for the Swarm instrument (Eriksson et al., 2008). The resolution is lowered to that of the measurement ranges (i.e. a simulation of the ADCs is performed) and, finally, the current-voltage relationship is plotted, first during time of flight and then as a regular I-V plot at a specified point in orbit.

A complication that arose when running this model was that when the environment gets very cold, the Debye length gets considerably much smaller than the probe radius and the sheath formation strongly influences also the ion current. When this happens, the Swarm model breaks down and because of this the codes had to be modified further. As a simple yet reasonable model for the ion current, we used the result by Kiel (1971) to obtain:

$$I_i = I_i^0 \left[1 + \left(\frac{\lambda_D}{a} \right)^{2/3} \sqrt{\frac{e|V_p|}{k_B T_i}} \right]^2, \quad (59)$$

where a is the probe radius. We do not expect that this expression will give a very good model for the ion current in our case of a cold flowing plasma, but it at least gives a realistic order of magnitude also to the ion current, which is all we need here.

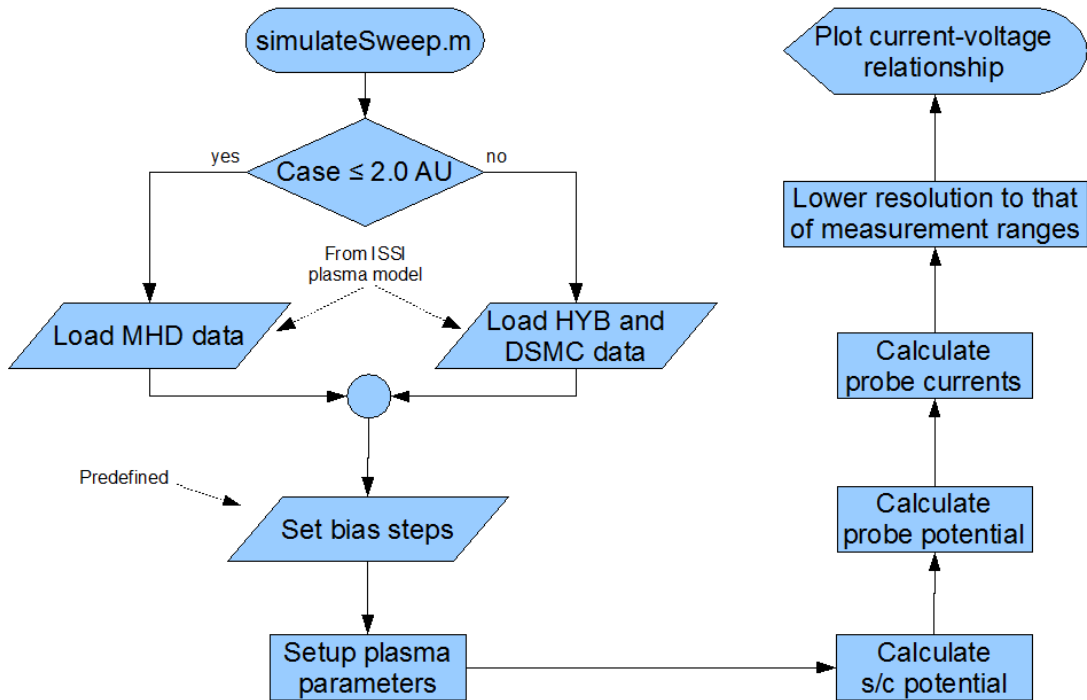


Figure 26: Flowchart of the LAP model.

7 Results

In this section we will discuss the results from combining the instrument model with the ICES model for the coma with reasonable sample orbits around the comet. A few interesting trajectories will be discussed while the complete set of plots can be found at the web page http://www.space.irfu.se/exjobb/2009_kristoffer_hultgren.

7.1 Approach Phase and the 3.3 AU Case

Looking at Figure 10 in Section 4.6, we see that the approach to the comet at rendez-vous is at an angle of about 45 degrees from both the negative y -axis and the positive x -axis, and occurs close to the ecliptic plane. Starting to model the measurements at 500 km (the corner of the hybrid model box) and all the way to just 14 km from the nucleus gives an output as illustrated in Figure 27. Here we see that the probe current is fairly constant during the approach and that no legible signature in density should be expected (further discussed in the conclusion). However, the increased density when getting closer to the comet in turn increases the current slightly and also the magnetic field starts to be affected in the vicinity of the object.

To get a better view, Figure 28 shows a sweep at 50 km from the comet. Here the photocurrent can easily be resolved, being the saturated current for high negative voltages, i.e. about -7.4 nA (this can also be seen as the constant colored area for negative potentials in Figure 27). The current then rises exponentially, marking the point where the electron current kicks in and hence also the spacecraft potential; since the electron current rises for positive potentials, and the probe potential is $V_p = V_b + V_{s/c}$, the spacecraft potential from our model can be retrieved from $V_{s/c} = -V_b$ in the point where $\frac{d^2 I_p}{dV_b^2} = \max$, i.e. where the curve goes from being exponential to linear, and is in the range +3.5 to +4 V. The output from our code tells us that $V_{s/c} = +3.85$ V, so the plot of the sweep in question is showing a satisfying result.

Practically, Figure 27 shows that, during the approach phase, $I_e < 10$ nA and hence a bias voltage mode is not preferred; the electron current would probably drown in photoelectrons from the spacecraft itself and it is probably more rewarding to use the probes in bias current mode.

If we now turn to an orbit at an altitude of 5 km in the terminator plane⁴, Figure 29 shows the bias sweep current vs. time of flight; also indicated on the x -axis is the position in orbit, where zero degrees is defined as the point where $z = 0$ on the positive y -axis (see Section 5.1 for a description of the coordinate system used). We see that the current has increased slightly ($I_p < 25$ nA) due to the increased density, but this may still not be enough to exceed the photocurrent from the spacecraft. It seems that, as discussed in Section 6.3, the contribution to the probe current from the spacecraft photoelectrons is likely to increase by the value of the probe photocurrent for every 10 V bias potential. The corresponding I-V plot for this point, $\theta = 0$, is shown in Figure 30 where we can see an expected spacecraft potential of about +1.5 to +2.0 V and a photocurrent of about -7.5 nA, very similar to the situation at 50 km but with a slightly decreased spacecraft potential due to the increased density⁵. This practically means that, in this case, the cloud of photoelectrons surrounding the spacecraft would contribute to the probe current with about 7.5 nA per 10 V, which, as predicted, exceeds the probe current by far. It should however be added that the current from the photoelectron cloud strongly depends on the attitude of the spacecraft; it decreases significantly when the probe is located behind the plane of the solar arrays.

⁴The terminator plane is the plane where $x = 0$ in our system, i.e. making a ground track at the day-/nightside border.

⁵The spacecraft potential is determined from the balance between the collected plasma electrons I_e and the emitted photoelectrons I_{ph} . The former depends on the plasma density but not the latter, so the equation $I_e = I_{ph}$ becomes a relation between the density and the spacecraft potential (Eriksson and Winkler, 2007).

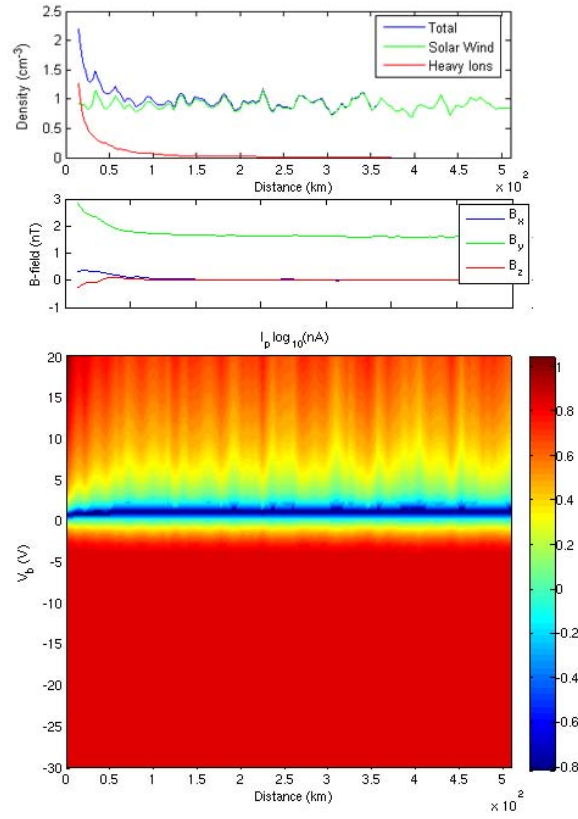


Figure 27: Bias sweep current vs. distance during Rosetta's approach to comet 67P/CG. Also included is the solar wind and heavy ion density and the components of the magnetic field during the approach.

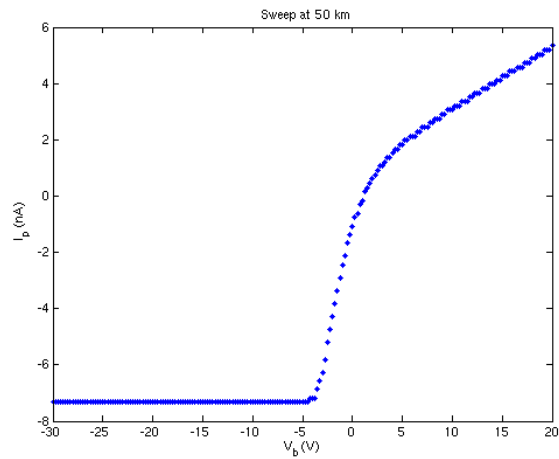


Figure 28: Bias sweep during the approach phase, 3.3 AU, at a distance 50 km from the comet.

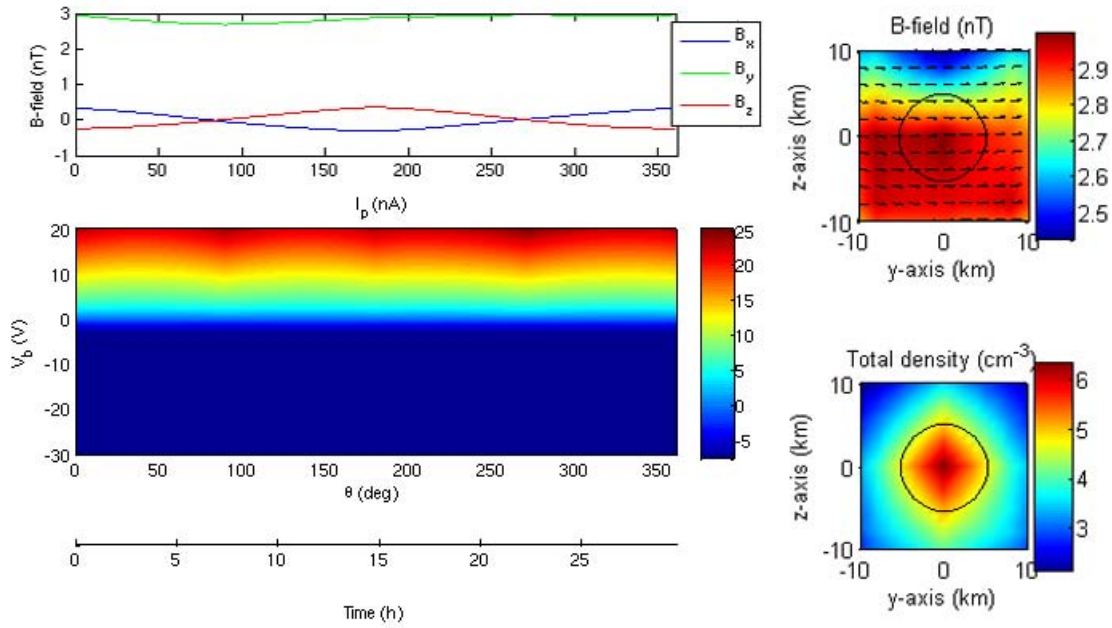


Figure 29: Bias sweep current vs. time of flight during one orbit at a cometocentric distance of 5 km and a heliocentric distance of 3.3 AU.

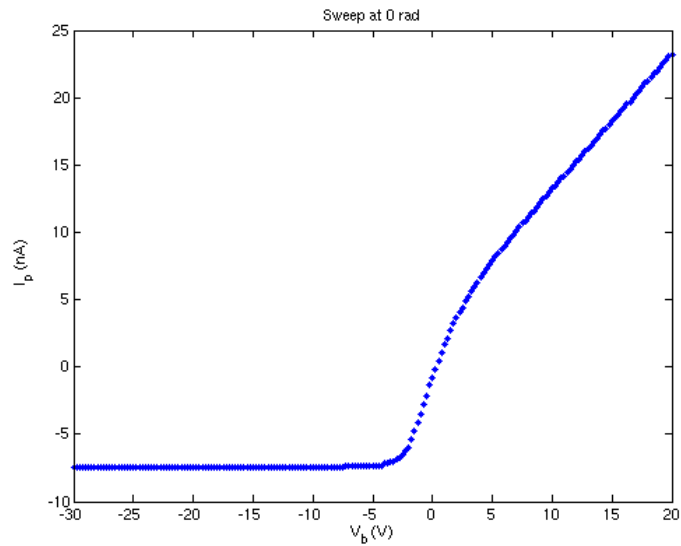


Figure 30: Bias sweep at the point $\theta = 0$, a cometocentric distance of 5 km, and a heliocentric distance of 3.3 AU.

7.2 The 2.7 AU Case

Turning now to the 2.7 AU case where we still are using the Hybrid model, Figure 31 shows the sweep current vs. time of flight for an orbit at 10 km altitude and we see that there are no big variations in the currents, which have, however, increased to reach 300 nA for high bias voltages. By looking at the orbit inserted in the environment plot (to the right) we see that the spacecraft is located in an area of fairly constant density, and hence the practically non-existing current variations.

If we have a closer look at the sweep at $\theta = 0$, Figure 32, the spacecraft potential and the photocurrent can be expected to be close to zero and about -15 nA respectively. Since the exact spacecraft potential is hard to extract, a high resolution sweep with step size 10 mV can be performed over the range ± 1.2 Volts (see Section 6.2); the result is depicted in Figure 33 and using the method described above, we can see that the spacecraft potential seems to be about -0.05 V. In fact, from the output of our code, $V_{s/c} = -0.017$ V, which shows that extracting the exact spacecraft potential from the I-V curve can be a difficult task, at least by eyesight alone.

Since studies of the cometary environment would benefit from Rosetta investigating not only the few kilometers closest to the comet, but also spending some time further out, occasional excursions from the nucleus is an attractive possibility. There is, however, a conflict between these excursions and asteroid flybys due to the ΔV cost and some of the spare ΔV has already been used for the asteroid flybys. It would still be very interesting to see what the models say about the coma plasma structure, especially the boundaries, so an excursion has been included for each of the cases. Figure 34 shows the bias sweeps along a path directed towards the Sun. As can be seen, the cometary activity is not very large, but there is a difference in current, and hence density, at a cometocentric distance of about 150 km as can be expected from the plasma environment modeled in Section 5.

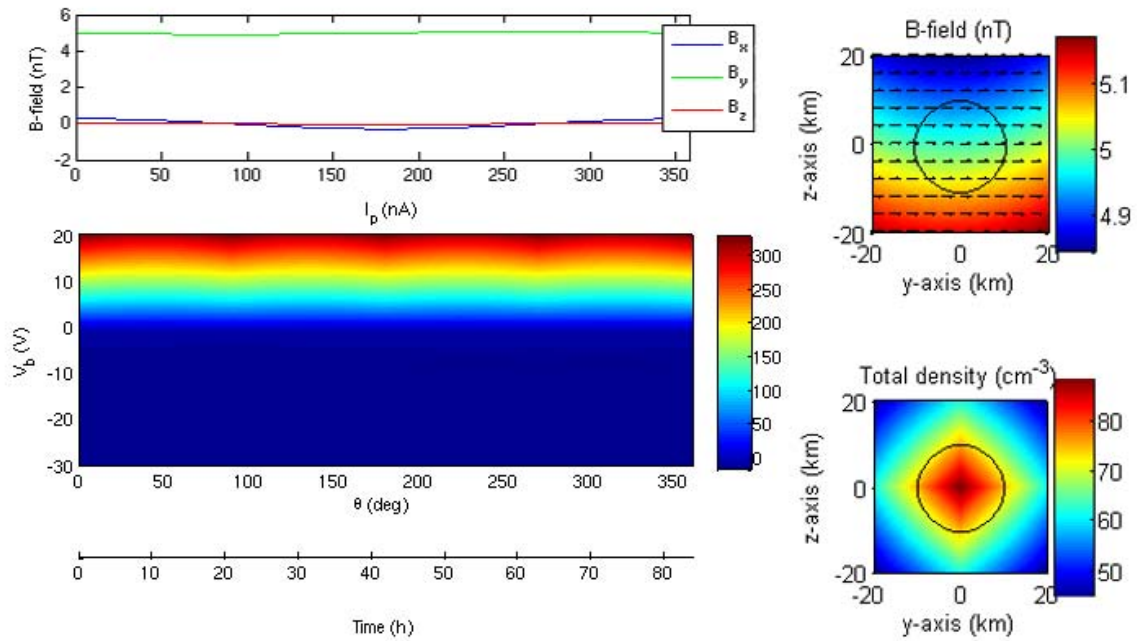


Figure 31: Bias sweep current vs. time of flight during one orbit at a cometocentric distance of 10 km and a heliocentric distance of 2.7 AU.

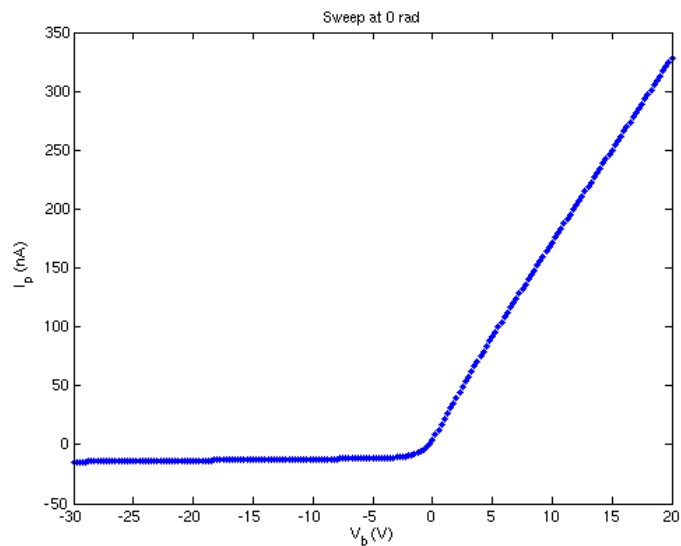


Figure 32: Bias sweep at the point $\theta = 0$, a cometocentric distance of 10 km, and a heliocentric distance of 2.7 AU.

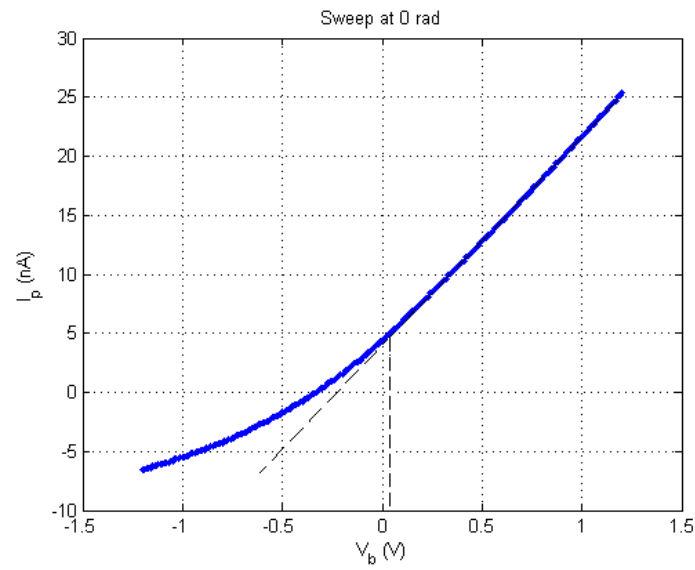


Figure 33: High resolution bias sweep at the point $\theta = 0$, a cometocentric distance of 10 km, and a heliocentric distance of 2.7 AU. Here the step size is 10 mV and the range chosen for simulation is -2.2 to +0.2 V.

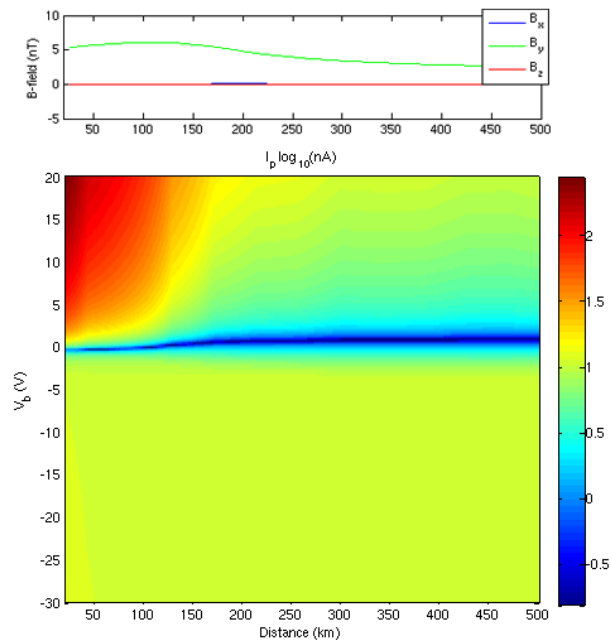


Figure 34: Bias sweep current vs. distance on an imaginary path along the x -axis (towards the Sun) at a heliocentric distance of 2.7 AU.

7.3 The 2.0 AU Case

At the 2.0 AU case the cometary activity is considerably larger and we have to use the MHD model. Bias sweeps at a 10 km orbit here shows a little bit more features (Figure 35); these strange patterns at each 45 degrees can also be seen from a collection of parameter plots (Figure 36) and is due to that the chosen orbit happens to coincide with the border of the diamagnetic cavity, as can be seen in the environment plots to the right in Figure 35, including the modeled orbit. At this border, the magnetic field goes from zero up to 25 nT in a very short distance and the plasma is transported away from the nucleus. It can be noted that the cavity is not forming a perfect circle in the orbital plane, and hence the border is crossed every 45 degree, resulting in decreased currents due to the decreased density. This can be seen clearly in the plot of the components of the magnetic field (top left of Figure 35) and leads to a very interesting conclusion: if the assumption that the orbits are placed this close to the comet, which is the case according to Glassmeier et al. (2007a), the most interesting part of the mission for the LAP measurements is at heliocentric distances of between 2.0 and 1.3 AU. i.e. in this range, Rosetta has a big chance of being located close to the contact surface.

Also note that the x -component of the magnetic field changes direction from one side of the comet to the other, which is a good indication of the magnetic field draping discussed in Section 2.3.

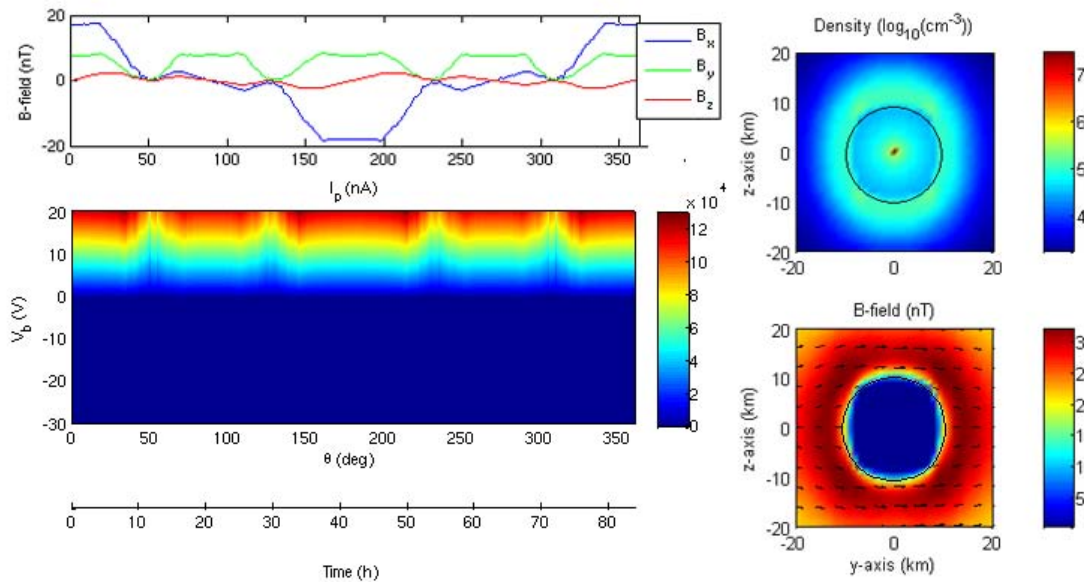


Figure 35: Bias sweep current vs. time of flight during one orbit at a cometocentric distance of 10 km and a heliocentric distance of 2.0 AU.

Figure 37 shows the sweeps during an excursion along the comet-Sun line and a small decrease in current at about 500 km can be observed. This fits well with the environment plots in Section 5 and is probably the signature of a partially developed bow shock.

Closer to the comet, at a distance below 400 km, the current reaches up to $10 \mu\text{A}$, which also can be seen in Figure 38 where the current is plotted together with the fluid density for a constant bias potential of 1 V. As discussed in Section 6.2, the current at constant bias is a means for tracking density variations,

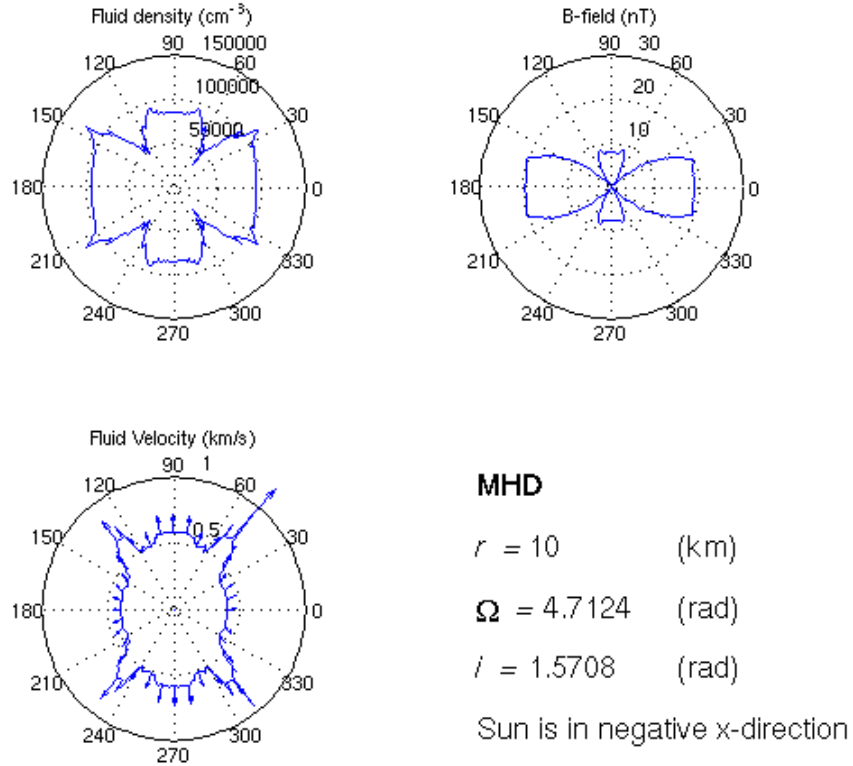


Figure 36: Plasma parameters vs. time of flight during one orbit at a cometocentric distance of 10 km and a heliocentric distance of 2.0 AU.

and the similarity between the density and current curves in this case indicates that the constant voltage bias is a useful operational mode here. Occasional sweeps should be inserted to give temperature estimates at lower time resolution.. The fact that the current reaches up to $10 \mu\text{A}$ can be a problem for the instrument measurement ranges which only covers up to $10 \mu\text{A}$ and thus is on the edge of being insufficient. Therefore a new sweep with a constant bias potential of 0.25 V is plotted in Figure 39. Here we see that the current follows the density neatly and only reaches $0.4 \mu\text{A}$ when getting close to the comet, and this is thus a much better bias potential to use.

Figure 40 shows the sweep at a point on a 10 km orbit. We can here see that there is no sign of an exponential function and hence no chance of determining either the density nor the temperature. Not even a high resolution sweep at bias potentials in the range $\pm 1.2 \text{ V}$ (Figure 41) is sufficient to extract T_e . This is because the temperature is too low so LAP can at best give an estimate of $n_e \sqrt{T_e}$ by determination of I_e^0 . However, in this situation of low temperature, the MIP instrument (Trotignon et al., 2007) is expected to work well and provide accurate determinations of n_e and T_e . Combining the MIP n_e and T_e values with the high time resolution probe current measurements obtained by LAP at constant bias voltage is likely to be a fruitful way of obtaining details on plasma processes in this environment.

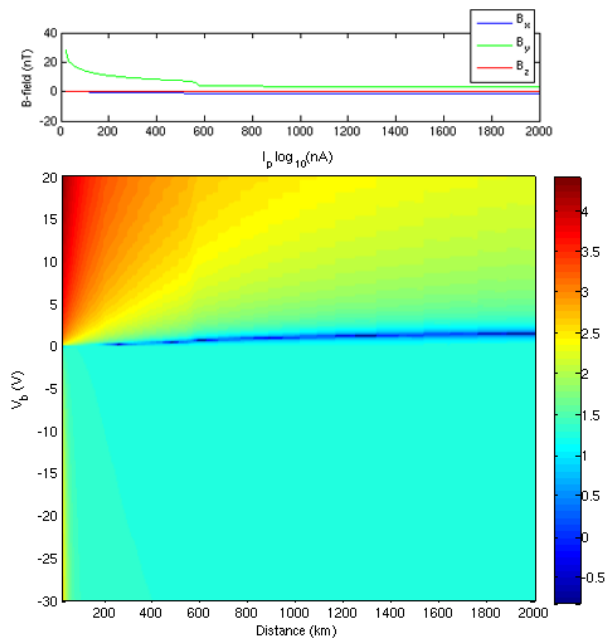


Figure 37: Bias sweep current vs. distance on an imaginary path along the x -axis (towards the Sun) at a heliocentric distance of 2.0 AU.

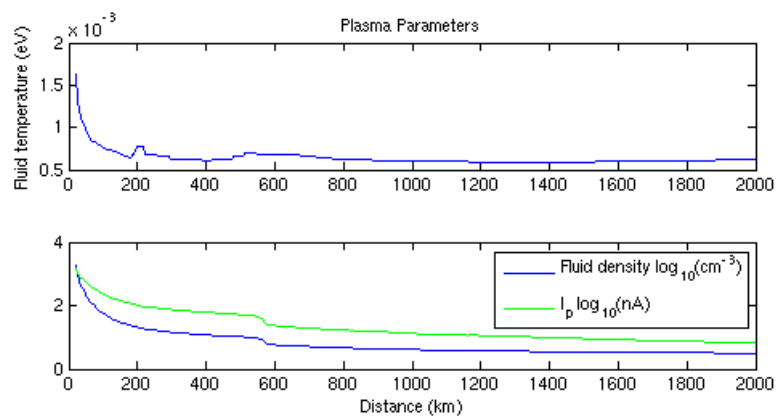


Figure 38: Fluid temperature, density, and current vs. cometocentric distance at 2.0 AU.

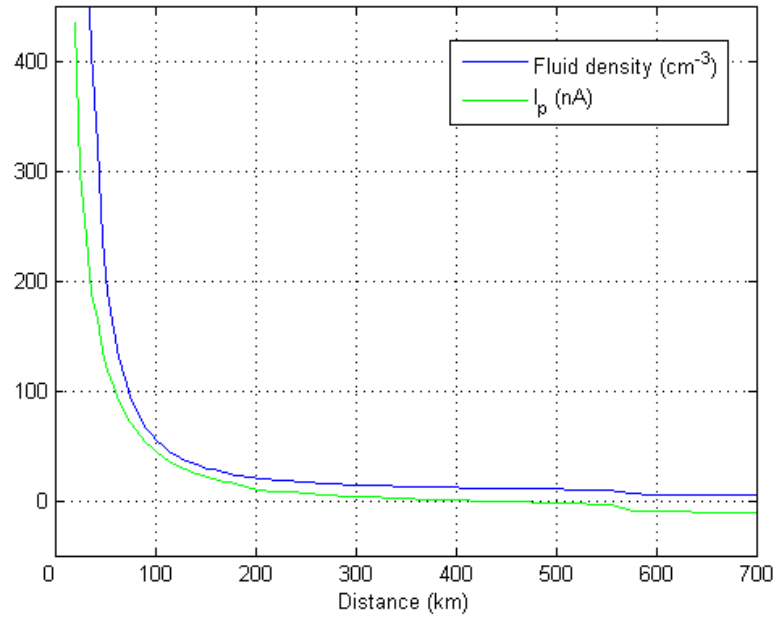


Figure 39: Fluid density and current vs. cometocentric distance at 2.0 AU.

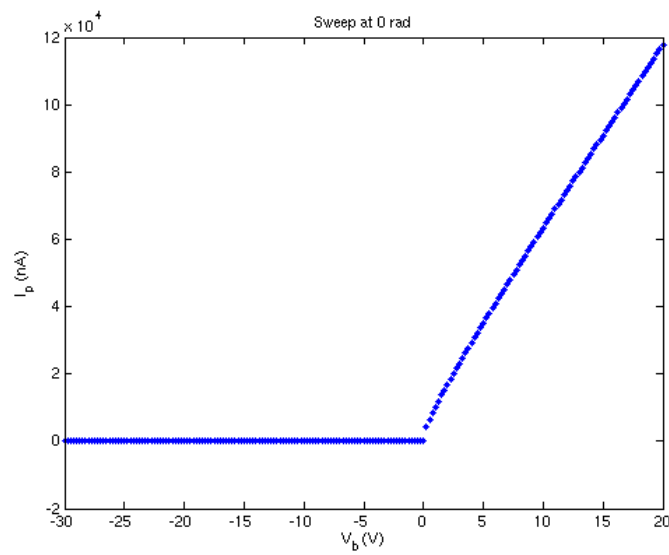


Figure 40: Bias sweep at the point $\theta = 0$, a cometocentric distance of 10 km, and a heliocentric distance of 2.0 AU.

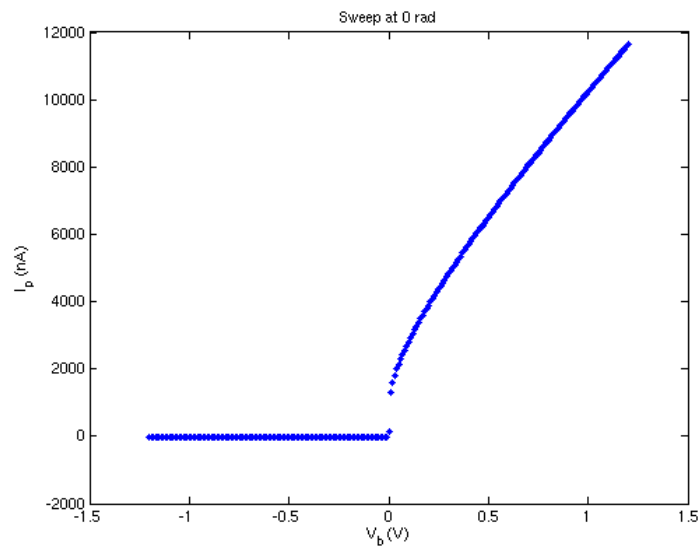


Figure 41: High resolution bias sweep at the point $\theta = 0$, a cometocentric distance of 10 km, and a heliocentric distance of 2.0 AU.

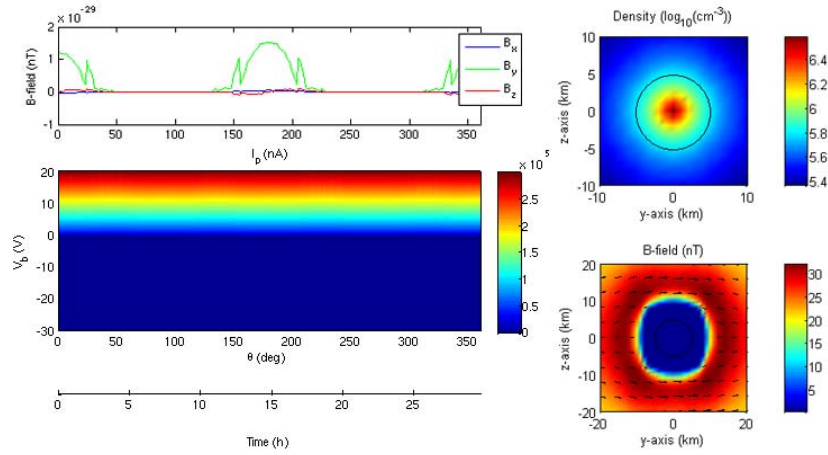


Figure 42: Bias sweep current vs. time of flight during one orbit at a cometocentric distance of 5 km and a heliocentric distance of 1.3 AU.

7.4 The 1.3 AU Case

At 1.3 AU the cometary activity is even larger and, although the sweeps during a 5 km orbit, shown in Figure 42, experiences no significant variations, the density and the probe current reaches up to $6.5 \cdot 10^5 \text{ cm}^{-3}$ and $+300 \mu\text{A}$ respectively; this exceeds by far the maximum measurement range of $+10 \mu\text{A}$. There is however little need to cover the full bias voltage range in the densest plasmas (Eriksson et al., 2007), but by looking at Figure 43, which shows a sweep during the excursion with a constant bias potential $V_b = 1 \text{ V}$, we see that even here the current is very high ($0.1\text{-}10 \mu\text{A}$). This again tells us that a much lower bias potential is necessary to be able to make any reasonable measurements and for this a new sweep with bias potential 0.25 V is shown in Figure 44, where we see that the current only reaches about $5 \mu\text{A}$ which is a much better result. However, this is still a bit high and, in reality, a smaller bias potential, perhaps 0.05 V which would result in a maximum current of $2 \mu\text{A}$, would likely be chosen in this situation. Also, the plot shows a decrease in current between 30-50 km and by comparing this with the environment plots of the density and magnetic field (Figure 45), we see that this drop is well fitted with the magnetic cavity and the corresponding density drop.

An excursion was modeled even at the perihelion distance and this is shown in Figure 46. Here the bow shock is fully developed and can be seen as a decrease in current at about 3700 km from the comet. Looking at the plots in Figure 43 we see that the bow shock is characterized by a decrease in density, which matches well with theory.

The problem with the sweeps discussed for the 2.0 AU case is also inherent at 1.3 AU. Figure 47 and 48 show the bias sweeps for a 5 km orbit in standard resolution and high resolution respectively and we see that the fact that no exponential function can be resolved endures. As in the 2.0 AU case, a good strategy could be to rely on MIP for n_e and T_e measurements for calibrating the LAP probe current, using the available LAP telemetry for high time resolution monitoring of variations in the probe current at fixed bias rather than for bias sweeps.

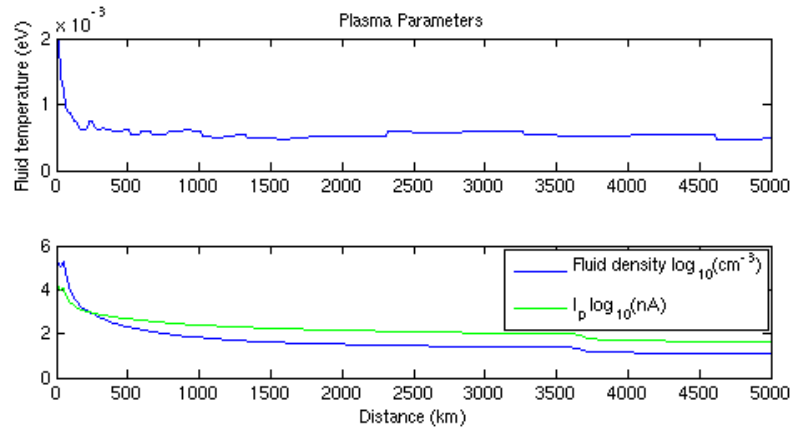


Figure 43: Fluid temperature, density and current vs. cometocentric distance at 1.3 AU.

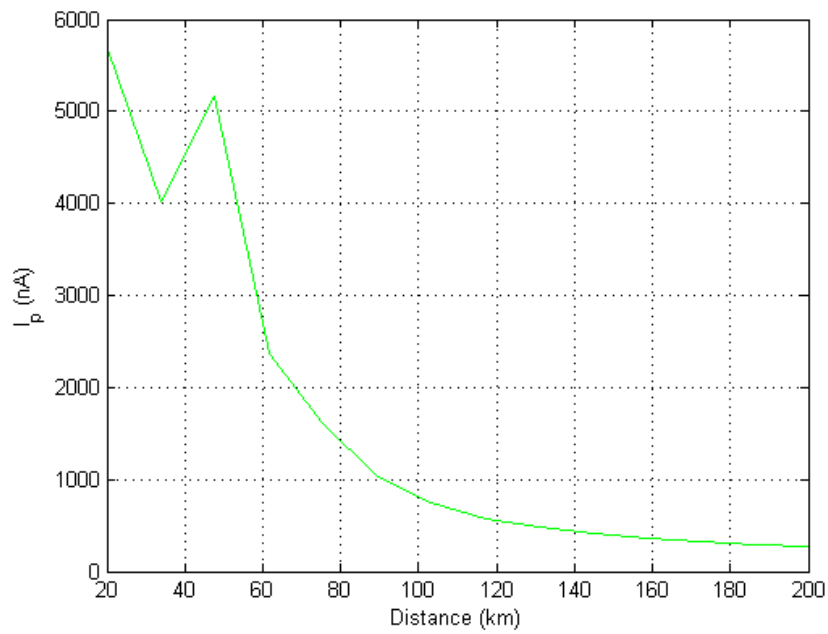


Figure 44: Current vs. cometocentric distance at 1.3 AU.

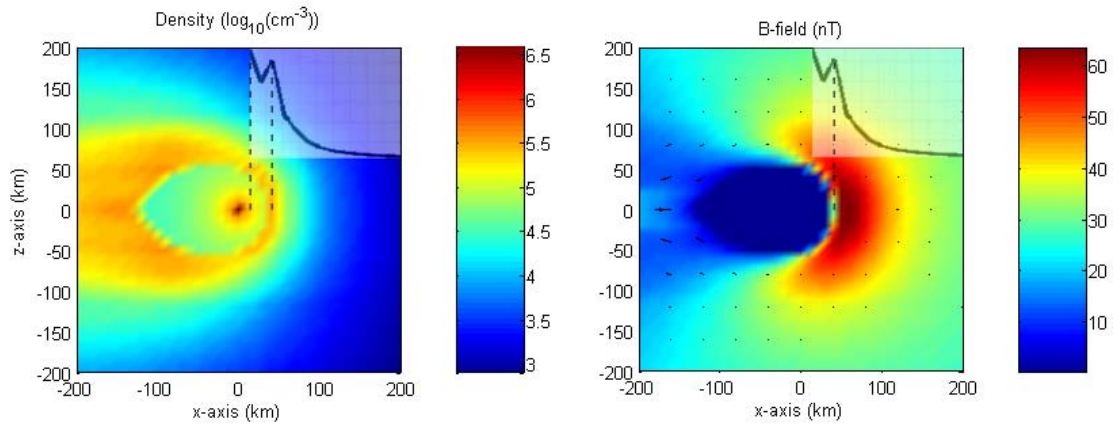


Figure 45: The density and magnetic field at 1.3 AU compared with the measured current using constant bias potential.

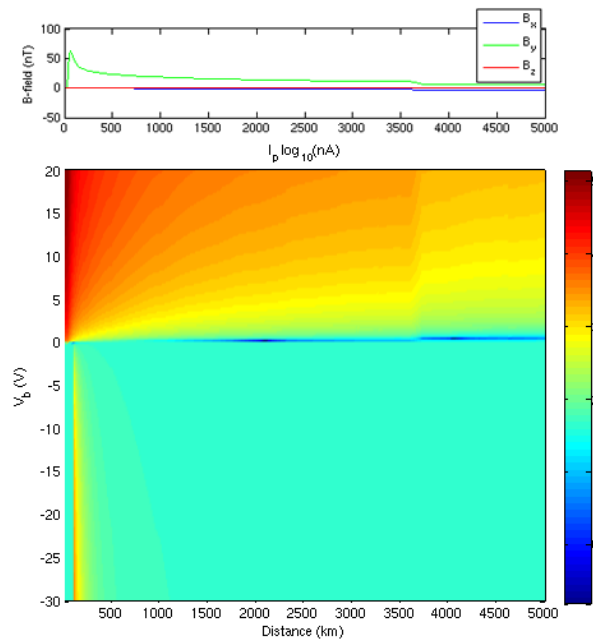


Figure 46: Bias sweep current vs. distance on an imaginary path along the x -axis (towards the Sun) at a heliocentric distance of 1.3 AU.

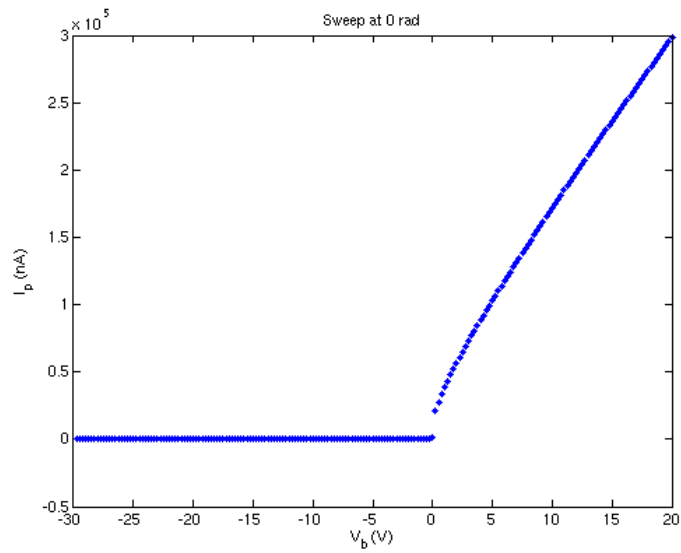


Figure 47: Bias sweep at the point $\theta = 0$, a cometocentric distance of 5 km, and a heliocentric distance of 1.3 AU.

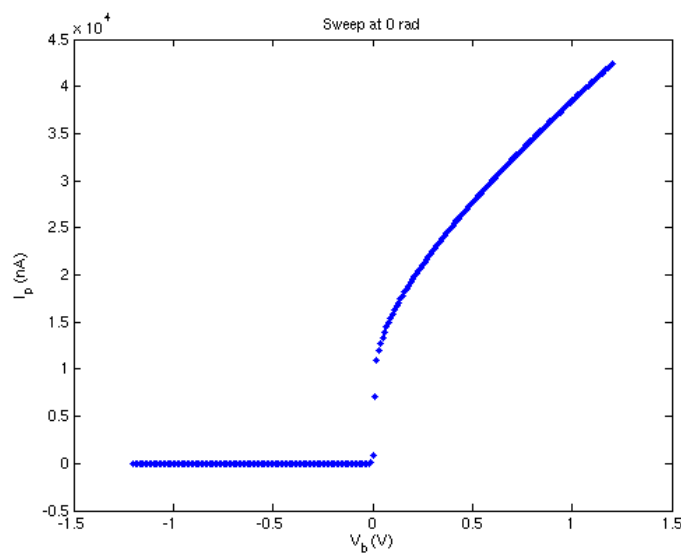


Figure 48: High resolution bias sweep at the point $\theta = 0$, a cometocentric distance of 5 km, and a heliocentric distance of 1.3 AU.

8 Concluding Remarks and Possible Future Work

The objective of this project was to prepare for LAP operations at the comet by simulating LAP measurements in the plasma environment expected at the comet, and for what can be regarded as typical operational scenarios for the spacecraft itself.

It has been shown that, if the outgassing is correctly described by the models, it is very unlikely that any signature of the comet will be seen in the plasma density during the approach phase. However, if the outgassing is unevenly distributed over the nucleus surface, we should be able to detect jets, and the density would in this case be modulated with the rotational frequency of the comet - this density signature is possible to detect.

A conclusion that can be drawn from the results of the 1.3 AU and 2.0 AU cases is that the very low temperatures predicted by the models create some problems for LAP. The LAP probe currents (which can be sampled continuously with 57.8 Hz and shorter sequences with 18 750 Hz) are appropriate to follow the dynamics, but to extract the n_e and T_e dependence so to give an absolute value of n_e we need other instruments, e.g. the Mutual Impedance Probe (MIP) designed to measure the electron density and temperature, in particular inside the contact surface. By analyzing LAP data together with data from other RPC instruments, it will be possible to investigate a broad range of problems no single RPC instrument could cover on its own. More information on MIP can be found in Trotignon et al. (2007).

In the above results, it was also shown that at 2.0 to 1.3 AU, Rosetta has a big chance of being located close to the contact surface of the comet which creates a very good possibility of gaining interesting data. Of course, the real outgassing might differ significantly from the model, but the contact surface will also move both in and out as the solar wind and the outgassing varies. This means that in some occasions, Rosetta will travel through the surface and it may be thought that this could occur at 2.2 - 1.8 AU or so.

Overall, the plasma models used for the cometary coma are very well suited for this purpose. However, the DSMC model seems to give some strange outputs when looking at Figure 22, and a problem has also been encountered when modeling the neutral particle velocities with this model. Due to this, we have used as few parameters as possible from the DSMC model.

This work is in no way complete for closure; there are lots more left to do in this field. Possible future work could for example be to:

- model comet dynamics;
- model currents from the photoelectrons emitted by the spacecraft;
- model spacecraft wake and other spacecraft-plasma interaction effects beyond the crude spacecraft potential model used here;
- model spacecraft attitude effects;
- perform closed-loop runs where, in addition to the spacecraft potential, the density and the temperature are derived from the output and compared with the input;
- study the possibility to pick up signatures at the comet rotation frequency in the LAP data during the approach phase as an indication of early cometary activity, inhomogeneously distributed over the comet surface;
- see to that all models can be run from a command line to avoid the copying and pasting from and to text files when using the GUI;
- rewrite the codes to collect similar functions into single extensive functions, maybe rewriting the codes in an object oriented programming language to speed up the modeling.

While the hybrid and MHD model results in the ICES model are static solutions, one may consider simple means to model dynamical effects on the measurements. For example, by just letting the origin of the coordinate system move around in time according to some prescribed function of time, one could model the effect of moving plasma boundaries on the measurements. Alternatively, one may put a time-dependent rescaling factor on the coordinates. If such a rescaling instead is applied to the fields themselves (density, temperature, flow speed, B-field, etc), one may have a crude way to model the effect of solar wind perturbations on the measurements. Likewise, effects of small scale structures in the cometary outgassing (e.g. jets) could possibly be modeled by just multiplying the radial coordinate and/or the physical fields by a scaling function depending on angular position on the cometary surface, even including the rotation of the nucleus. None of these simple extensions would probably lead to physically consistent models, but this is of little concern to us as long as they give parameter variations along the spacecraft orbit which are reasonably representative of what may be expected, and thus can be used to evaluate measurement strategies at the comet

Another aspect that should be considered is the inhomogeneity of the comet nucleus; the models uses a perfectly spherical nucleus but this is of course not the case in the real world.

Acknowledgments

First of all, I would like to thank my supervisor Dr Anders Eriksson at the Swedish Institute of Space Physics, Uppsala, for defining the project and for all his help, enthusiasm, encouragement, and instructive conversations - a really unique supervisor.

I would like to express my deepest gratitude and gratefulness to ESA and the Directorate for Human Spaceflight and Exploration, especially to Dr Piero Messina, for providing me with a well needed scholarship to complete my work - it really helped me getting through the daily rounds by not having the usual stressful economic situation of a student.

I am indebted to all people helping me with the plasma model, especially Nikolaos Gortsas at DLR and Kenneth Hansen, Martin Rubin, and Valeriy Tenishev at the University of Michigan.

I am also greatly thankful to all people involved with coordinating the Spacemaster programme - thank you for good arrangements and for creating this excellent possibility for me to develop my knowledge and experiences while also having a great time.

A huge thanks goes out to my family for always being so supportive and last, but not least, I would like to thank Sara, as a partner and a friend, for always being there and for her constant understanding, especially during the later part of my work when most of my time awake was spent in front of my computer.

References

- Bagdonat, T. and Motschmann, U. (2002a) 3D Hybrid Simulation Code Using Curvilinear Coordinates, *Journal of Computational Physics*, **183**, 470–485, doi:10.1006/jcph.2002.7203.
- Bagdonat, T. and Motschmann, U. (2002b) From a Weak to a Strong Comet - 3D Global Hybrid Simulation Studies, *Earth, Moon and Planets*, **90**, 305–321.
- Billvik, M. (2005) *The Rosetta Earth flybys*, Master's thesis, Uppsaa University.
- Brackbill, J. U. and Barnes, D. C. (1980) The Effect of Nonzero $\nabla \cdot \vec{B}$ on the Numerical Solution of the Magnetohydrodynamic Equations, *Journal of Computational Physics*, **35**, 426.
- Chen, F. F. (1984) *Introduction to Plasma Physics and Controlled Fusion*, vol. 1: Plasma Physics, 2nd rev ed., Dordrecht: Kluwer Academic Publishers Group.
- Chobotov, V. A., ed. (2002) *Orbital Mechanics*, AIAA Education Series, 3rd ed., Reston: AIAA.
- Coates, A. J. (1997) Ionospheres and Magnetospheres of Comets, *Adv. Space Res.*, **20**(2), 255–266.
- Coffey, V. N., Wright, K. H., Minow, J. I. et al. (2008) Validation of the Plasma Densities and Temperatures From the ISS Floating Potential Measurement Unit, *IEEE Transactions on Plasma Science*, **36**(5), 2301–2308.
- Dendy, R. O. (1995) *Plasma Physics: An Introductory Course*, Cambridge: Cambridge University Press.
- Edberg, N. (2006) *The Rosetta Mars Flyby*, Master's thesis, Uppsala University.
- Eleuterio, T. F. (1999) *Riemann Solvers and Numerical Methods for Fluid Dynamics*, Berlin: Springer Verlag.
- Engwall, E. (2006) *Cold Magnetospheric Plasma Flows: Properties and Interaction with Spacecraft*, Licentiate thesis, Uppsala University.
- Eriksson, A., Boström, R., Gill, R. et al. (2007) RPC-LAP: The Rosetta Langmuir Probe Instrument, *Space Science Reviews*, **128**, 729–744, doi:10.1007/s11214-006-9003-3.
- Eriksson, A., Gill, R., Rosenqvist, L. et al. (2008) Swarm CEFI-LP Level 1b Algorithms, Tech. rep., Swedish Institute of Space Physics, Uppsala.
- Eriksson, A. I., Gill, R., Wahlund, J.-E. et al. (2009) RPC-LAP: The Langmuir probe instrument of the Rosetta plasma consortium, unpublished.
- Eriksson, A. I. and Winkler, E. (2007) Photoemission Current and Solar EUV Radiation: Cluster and Timed Observations, *Proceedings of the 10th Spacecraft Charging Technology Conference (SCTC-10)*.
- Glassmeier, K.-H., Boehnhardt, H., Koschny, D. et al. (2007a) The Rosetta Mission: Flying Towards the Origin of the Solar System, *Space Science Reviews*, **128**, 1–21, doi:10.1007/s11214-006-9140-8.
- Glassmeier, K.-H., Richter, I., Diedrich, A. et al. (2007b) RPC-MAG: The Fluxgate Magnetometer in the ROSETTA Plasma Consortium, *Space Science Reviews*, **128**, 649–670.

- Gombosi, T. I., DeZeeuw, D. L., Häberli, R. M. et al. (1996) Three-Dimensional Multiscale MHD Model of Cometary Plasma Environments, *Journal of Geophysical Research*, **101**, 15,233–15,253.
- Gombosi, T. I., Hansen, K. C., DeZeeuw, D. L. et al. (1999) MHD Simulation of Comets: The Plasma Environment of Comet Hale-Bopp, *Earth, Moon and Planets*, **79**, 179–207.
- Hansen, K., Bagdonat, T., Motschman, U. et al. (2007) The Plasma Environment of Comet 67P/Churyumov-Gerasimenko Throughout the Rosetta Main Mission., *Space Science Reviews*, **128**, 133–166, doi:10.1007/s11214-006-9142-6.
- Hansen, K. and Rubin, M. (2008) *ICES User Manual: Code Version 1.1b*, ISSI.
- Häberli, R. M., Altwegg, K., Balsiger, H. et al. (1996) Heating of the thermal electrons in the coma of Comet 1P/Halley, *Journal of Geophysical Research*, **101**, 15,579–15,590.
- Ip, W.-H. (1985) An Overview of Gas Phenomena in Comet Halley, *Adv. Space Res.*, **5**, 223–245.
- Kallenrode, M.-B. (2004) *Space Physics - An Introduction to Plasmas and Particles in the Heliosphere and Magnetospheres*, Springer.
- Keller, U. (2008) Asteroid (2867) Steins, in *Rosetta Steins fly-by Press Conference*, Darmstadt: OSIRIS Principal Investigator, Max-Planck-Institut für Sonnensystemforschung.
- Kiel, R. E. (1971) Electrostatic Probe Theory for Free-Molecular Spheres, *AIAA*, **9**(7), 1380–1382.
- Kim, H.-M. and Jung, Y.-D. (2007) Dynamic non-Maxwellian screening effects on elastic collisions in Lorentzian plasmas, *Physics Letters A*, **371**, 314–317.
- Lamy, P. L., Toth, I., Davidsson, B. J. R. et al. (2007) A Portrait of the Nucleus of Comet 67P/Churyumov-Gerasimenko, *Space Science Reviews*, **128**, 23–66, doi:10.1007/s11214-007-9146-x.
- Mamun, A. A., Shukla, P. K. and Morfill, G. E. (2004) Theory of Mach Cones in Magnetized Dusty Plasmas with Strongly Correlated Charged Dust Grains, *Physical Review Letters*, **92**(9).
- Mott-Smith, H. M. and Langmuir, I. (1926) The Theory of Collectors in Gaseous Discharges, *Physical Review*, **28**, 727–763.
- Parks, G. K. (2004) *Physics of Space Plasmas*, Boulder: Westview Press.
- Powell, K. G., Roe, P. L., Linde, T. J. et al. (1999) A Solution-Adaptive Upwind Scheme for Ideal Magnetohydrodynamics, *Journal of Computational Physics*, **154**, 284–309.
- Rubin, M., Hansen, K. C., Gombosi, T. I. et al. (2009) Ion composition and chemistry in the coma of Comet 1P/Halley - A comparison between Giotto's Ion Mass Spectrometer and our ion-chemical network, *Icarus*, **199**, 505–519.
- Tenishev, V., Combi, M. and Davidsson, B. (2008) A Global Kinetic Model for Cometary Comae: The Evolution of the Coma of the Rosetta Target Comet Churyumov-Gerasimenko Throughout the Mission, *The Astrophysical Journal*, **685**, 659–677.
- Troignon, J. G., Michau, J. L., Lagoutte, D. et al. (2007) RPC-MIP: The Mutual Impedance Probe of the Rosetta Plasma Consortium, *Space Science Reviews*, **128**, 713–728.

A Matlab Routines

In this appendix, the routines will only be described as function headers in alphabetic order. The complete set of codes is available for download at http://www.space.irfu.se/exjobb/2009_kristoffer_hultgren.

A.1 draworbit.m

| | |
|--------------|---|
| Function: | draworbit(r, inc, omega) |
| Author: | J. Kristoffer Hultgren |
| Description: | Draws the orbit with radius r (m), inclination inc (rad), and right ascension omega (rad). Returns the x,y,z-coordinates as a matrix M and exports the matrix M as a space separated textfile named output. |
| Input: | r - Radius of orbit inc - Inclination of orbit (wrt the Sun line) omega - Argument of right ascension |
| Output: | elem - A matrix [r inc omega] |

A.2 ecl2orb.m

| | |
|--------------|--|
| Function: | ecl2orb(elem, x, y, z) |
| Author: | J. Kristoffer Hultgren |
| Description: | Transforms coordinates from the ecliptic plane to the orbital plane. |
| Input: | elem - Orbital elements [r inc omega] x,y,z - Coordinates in the ecliptic plane |
| Output: | [x2 y2 z2] - Coordinates in the orbital plane |

A.3 go.m

| | |
|--------------|---|
| Function: | go() |
| Author: | J. Kristoffer Hultgren |
| Description: | Plots the plasma environment in a given plane at a given heliocentric distance. Requires the Hybrid model compiled on disk. MHD and DSMC models should be run in GUI. |
| Input: | - |
| Output: | - |

A.4 inst.m

| | |
|--------------|---|
| Function: | inst(dist, ni, nhi, Te, Ti, vi, vhi, Vb) |
| Author: | J. Kristoffer Hultgren |
| Description: | Sets up all plasma and instrument properties and constants and calculates the probe currents. |
| Input: | dist - Heliocentric distance (AU) ni - Solar wind ion number density (cm^{-3}) nhi - Heavy ion number density (cm^{-3}) Te - Electron temperature (eV) Ti - Ion temperature (eV) vi - Solar wind ion velocity (km/s) vhi - Heavy ion velocity (km/s) Vb - Bias voltage (V) |
| Output: | ip - Total probe current (A) ii - Ion current (A) iph - Photoelectron current (A) |

A.5 LP_Constants.m

| | |
|--------------|---|
| Structure: | LP_Constants |
| Author: | Reine Gill |
| Modified by: | J. Kristoffer Hultgren |
| Description: | Global structure containing natural constants: CO.qe - Electron charge (C) CO.Kb1 - Boltzmann's constant (J/K) CO.Kb2 - Boltzmann's constant (eV/K) CO.me - Electron mass (kg) CO.mp - Proton mass (kg) CO.u - Atomic mass unit CO.R_Earth - Earth's radius (m) CO.eps0 - ϵ_0 (F/m) CO.G - Gravitational constant ($\text{m}^3\text{kg}^{-1}\text{s}^{-2}$) CO.M - Mass of comet 67P/CG (kg) |
| Input: | - |
| Output: | - |

A.6 LP_Curre.m

| | |
|--------------|--|
| Function: | LP_Curre(vp, n, T, dn) |
| Author: | Anders I. Eriksson |
| Description: | Calculates the probe electron current. |
| Input: | vp - Probe potential (V) n - Electron density (cm^{-3}) T - Electron temperature (eV) dn - White noise (%) |
| Output: | ie - Electron current (A) |

A.7 LP_Currf.m

| | |
|--------------|---|
| Function: | LP_Currf(vp, jf0, Tf) |
| Author: | Anders I. Eriksson |
| Description: | Calculates the photoelectron current. |
| Input: | vp - Probe potential (V) jf0 - Photo saturation current ($\mu\text{A} \cdot \text{m}^{-2}$) Tf - Photoelectron temperature (eV) |
| Output: | iph - Photoelectron current (A) |

A.8 LP_Curri.m

| | |
|--------------|--|
| Function: | LP_Curri(vp, n, T, z, m, v, dn) |
| Author: | Anders I. Eriksson |
| Description: | Calculates the probe ion current. |
| Input: | vp - Probe potential (V) n - Ion density (cm^{-3}) T - Ion temperature (eV) z - Ion charge (elementary charge) m - Ion mass (proton masses) v - Ram speed (km/s) dn - White noise (%) |
| Output: | ii - Ion current (A) |

A.9 LP_Debye.m

| | |
|--------------|--|
| Function: | LP_Debye(n, T) |
| Author: | Anders I. Eriksson |
| Description: | Computes the debye length. |
| Input: | n - Electron density (cm^{-3}) T - Electron temperature (eV) |
| Output: | Ld - Debye length (m) |

A.10 LP_IProbe.m

| | |
|--------------|--|
| Function: | LP_IProbe(vp, P) |
| Author: | Anders I. Eriksson |
| Modified by: | J. Kristoffer Hultgren |
| Description: | Calculates the probe currents. |
| Input: | vp - Probe potential (V) P - Structure containing plasma parameters |
| Output: | ip - Current (A) ii - Ion current (A) iph - Photocurrent (A) |

A.11 LP_SetupInstrument.m

| | |
|--------------|---|
| Structure: | LP_SetupInstrument |
| Author: | Reine Gill |
| Modified by: | J. Kristoffer Hultgren |
| Description: | Sets up a global structure with instrument design constants: IN.probe_radius - Probe radius (m) IN.probe_hradius - Radius of hole in probe (m) IN.probe_area - Surface area of one probe (m ²) |
| Input: | - |
| Output: | - |

A.12 LP_SetupPlasma.m

| | |
|--------------|---|
| Function: | LP_SetupPlasma(dist, ni, nhi, Te, Ti, vi, vhi) |
| Author: | Reine Gill |
| Modified by: | J. Kristoffer Hultgren |
| Description: | Set up assumptions and empty place holders for plasma parameters: P.Tf - Temperature of photoelectrons (eV) P.nsp - Number of ion species P.Zi - Ion charges P.mi - Approximate ion masses P.jf0 - Photo saturation current ($A \cdot m^{-2}$) P.v - Spacecraft ram speed (km/s) P.dn - White noise (%) P.ni - Ion densities (cm^{-3}) P.Te - Electron temperature (eV) P.Ti - Ion temperature (eV) P.meff - Effective mass (kg) |
| Input: | dist - Heliocentric distance (AU) ni - Solar wind ion number density (cm^{-3}) nhi - Heavy ion number density (cm^{-3}) Te - Electron temperature (eV) Ti - Ion temperature (eV) vi - Solar wind ion velocity (km/s) vhi - Heavy ion velocity (km/s) |
| Output: | P - Plasma structure with plasma information |

A.13 LP_Walker.m

| | |
|--------------|--|
| Function: | LP_Walker(v, n, T, a) |
| Author: | Anders I. Eriksson |
| Description: | Computes the spherical probe sheath radius. |
| Input: | v - Probe potential (V) n - Electron density (cm^{-3}) T - Electron temperature (eV) a - Probe radius (m) |
| Output: | rs - Sheath radius (m) |

A.14 LP_Vsc.m

| | |
|--------------|--|
| Function: | LP_Vsc(P, vs0) |
| Author: | Anders I. Eriksson |
| Modified by: | J. Kristoffer Hultgren |
| Description: | Calculates spacecraft potential from plasma parameters. |
| Input: | P - Structure containing plasma parameters vs0 - Seed value for V_{sat} (V) |
| Output: | vst - Satellite potential (V) |

A.15 meanFreePath.m

| | |
|--------------|---|
| Function: | meanFreePath(n, r1, r2) |
| Author: | J. Kristoffer Hultgren |
| Description: | Calculates and plots the mean free path of an incoming particle/molecule on a population of particles/molecules. |
| Input: | n - Density of target population (m^{-3}) r1 - Radius of incoming particle/molecule (m) r2 - Radii of target particles/molecules (m) |
| Output: | - |

A.16 plotCurrents.m

| | |
|--------------|--|
| Function: | plotCurrents(data, ip, ii, iph, r, ne, Te) |
| Author: | J. Kristoffer Hultgren |
| Description: | Plots currents as functions of time. |
| Input: | data - Complete data set ip - Total current (A) ii - Ion current (A) iph - Photoelectron current (A) r - Radius of orbit (m) ne - Electron density (cm^{-3}) |
| Output: | - |

A.17 plotDSMCOOrbit.m

| | |
|--------------|--|
| Function: | plotDSMCOOrbit(dataD, elem) |
| Author: | J. Kristoffer Hultgren |
| Description: | Plots the plasma environment in a given orbit. |
| Input: | dataD - DSMC model data elem - Orbital elements [r inc omega] |
| Output: | - |

A.18 plotDSMCPPlane.m

| | |
|--------------|---|
| Function: | plotDSMCPPlane(dataD, heli) |
| Author: | J. Kristoffer Hultgren |
| Description: | Plots the plasma environment in a given plane at a given heliocentric distance. |
| Input: | dataD - DSMC model data heli - Heliocentric distance |
| Output: | - |

A.19 plotDSMCPolarOrbit.m

| | |
|--------------|--|
| Function: | plotDSMCPolarOrbit(dataD, elem, v) |
| Author: | J. Kristoffer Hultgren |
| Description: | Plots the plasma environment in a given orbit. |
| Input: | dataD - DSMC model data elem - Orbital elements [r inc omega] v - In orbit velocity (km/s) |
| Output: | - |

A.20 plotDSMCTime.m

| | |
|--------------|--|
| Function: | plotDSMCTime(dataD, r) |
| Author: | J. Kristoffer Hultgren |
| Description: | Plots the plasma environment in a given orbit. |
| Input: | dataD - DSMC model data r - Radius of orbit (m) |
| Output: | - |

A.21 plotHybridOrbit.m

| | |
|--------------|--|
| Function: | plotHybridOrbit(dataH, elem) |
| Author: | J. Kristoffer Hultgren |
| Description: | Plots the plasma environment in a given orbit. |
| Input: | dataH - Hybrid model data elem - Orbital elements [r inc omega] |
| Output: | - |

A.22 plotHybridPlane.m

| | |
|--------------|---|
| Function: | plotHybridPlane(dataH, heli) |
| Author: | J. Kristoffer Hultgren |
| Description: | Plots the plasma environment in a given plane at a given heliocentric distance. |
| Input: | dataH - Hybrid model data heli - Heliocentric distance |
| Output: | - |

A.23 plotHybridPolarOrbit.m

| | |
|--------------|--|
| Function: | plotHybridPolarOrbit(dataH, elem, v) |
| Author: | J. Kristoffer Hultgren |
| Description: | Plots the plasma environment in a given orbit. |
| Input: | dataH - Hybrid model data elem - Orbital elements [r inc omega] v - In orbit velocity (km/s) |
| Output: | - |

A.24 plotHybridTime.m

| | |
|--------------|--|
| Function: | plotHybridTime(dataH, r) |
| Author: | J. Kristoffer Hultgren |
| Description: | Plots the plasma environment in a given orbit. |
| Input: | dataH - Hybrid model data r - Radius of orbit (m) |
| Output: | - |

A.25 plotMHDOrbit.m

| | |
|--------------|---|
| Function: | plotMHDOrbit(dataM, elem) |
| Author: | J. Kristoffer Hultgren |
| Description: | Plots the plasma environment in a given orbit. |
| Input: | dataM - MHD model data elem - Orbital elements [r inc omega] |
| Output: | - |

A.26 plotMHDPlane.m

| | |
|--------------|---|
| Function: | plotMHDPlane(dataM, heli) |
| Author: | J. Kristoffer Hultgren |
| Description: | Plots the plasma environment in a given plane at a given heliocentric distance. |
| Input: | dataM - MHD model data heli - Heliocentric distance |
| Output: | - |

A.27 plotMHDPolarOrbit.m

| | |
|--------------|---|
| Function: | plotMHDPolarOrbit(dataD, elem) |
| Author: | J. Kristoffer Hultgren |
| Description: | Plots the plasma environment in a given orbit. |
| Input: | dataM - MHD model data elem - Orbital elements [r inc omega] |
| Output: | - |

A.28 plotMHDTIME.m

| | |
|--------------|---|
| Function: | plotMHDTIME(dataM, r) |
| Author: | J. Kristoffer Hultgren |
| Description: | Plots the plasma environment in a given orbit. |
| Input: | dataM - MHD model data r - Radius of orbit (m) |
| Output: | - |

A.29 plotSweep.m

| | |
|--------------|---|
| Function: | plotSweep(data, currout, Vb, r) |
| Author: | J. Kristoffer Hultgren |
| Description: | Plots sweeps at a complete orbit as a pcolor over time. |
| Input: | data - Complete data set currout - Current vector (A) Vb - Bias voltage vector (V) r - Radius of orbit (m) |
| Output: | - |

A.30 plotSweepMom.m

| | |
|--------------|--|
| Function: | plotSweepMom(currout, Vb) |
| Author: | J. Kristoffer Hultgren |
| Description: | Plots a momentary sweep at a certain point as a I-V plot |
| Input: | currout - Current vector (A) Vb - Bias voltage vector (V) |
| Output: | - |

A.31 scaleVec.m

| | |
|--------------|--|
| Function: | scaleVec(data, span, spanS) |
| Author: | J. Kristoffer Hultgren |
| Description: | Rescales a vector |
| Input: | data - Input vector span - Original vector size spanS - Wanted vector size |
| Output: | out - Rescaled vector |

A.32 simulate.m

| | |
|--------------|---|
| Function: | simulate() |
| Author: | J. Kristoffer Hultgren |
| Description: | Simulates LAP measurements and outputs the resulting current/voltage. |
| Input: | - |
| Output: | - |

A.33 simulateSweep.m

| | |
|--------------|---|
| Function: | simulateSweep() |
| Author: | J. Kristoffer Hultgren |
| Description: | Simulates LAP measurements and outputs the resulting current/voltage. |
| Input: | - |
| Output: | - |

A.34 simulateTraj.m

| | |
|--------------|---|
| Function: | simulateTraj() |
| Author: | J. Kristoffer Hultgren |
| Description: | Simulates LAP measurements during motion on a trajectory and outputs the resulting current/voltage. |
| Input: | - |
| Output: | - |

A.35 splitVector.m

| | |
|--------------|--|
| Function: | splitVector(data, span) |
| Author: | J. Kristoffer Hultgren |
| Description: | Splits a vector into a matrix. |
| Input: | data - Input vector span - Size of resulting matrix |
| Output: | out - Resulting matrix |

A.36 wholeSpace.m

| | |
|--------------|--|
| Function: | wholeSpace(p, lim) |
| Author: | J. Kristoffer Hultgren |
| Description: | Returns coordinates for the whole plane $p=0$, where p is one of the characters $x y z$ defining which axis is zero, and where the axes goes from $-lim$ to lim . |
| Input: | p - Non existing plane lim - Plane limits |
| Output: | $[x, y, z]$ - Coordinates of resulting plane |
